

A COMBINED COMPUTATIONAL AND EXPERIMENTAL STUDY OF THE HETEROAGGREGATION OF DISSIMILAR ADSORBENT PARTICLES

BY ANIK KUMAR CHATURBEDI

A dissertation submitted to the
School of Graduate Studies
Rutgers, The State University of New Jersey
in partial fulfillment of the requirements
for the degree of
Doctor of Philosophy
Graduate Program in Chemical & Biochemical Engineering

Written under the direction of
Dr. Nina Shapley & Dr. Rohit Ramachandran
and approved by

New Brunswick, New Jersey

January, 2019

© 2019

ANIK KUMAR CHATURBEDI

ALL RIGHTS RESERVED

ABSTRACT OF THE DISSERTATION

A COMBINED COMPUTATIONAL AND EXPERIMENTAL STUDY OF THE HETEROAGGREGATION OF DISSIMILAR ADSORBENT PARTICLES

by ANIK KUMAR CHATURBEDI

**Dissertation Director: Dr. Nina Shapley & Dr. Rohit
Ramachandran**

Heteroaggregation, the process of aggregation between dissimilar particles is becoming increasingly popular due to the versatile applicability of heteroaggregates. The specific requirements of these widespread application areas require customized heteroaggregates with unique set of properties related mainly to the size and composition of these heteroaggregates. This has created an immense need for a developed understanding of the heteroaggregate process. However, research on heteroaggregates have been very limited, even fundamental questions pertinent to the mechanism of heteroaggregation process remain unanswered to date. The goal of this work is to study and understand the heteroaggregation process both at particle scale to answer some of these fundamental queries about

heteroaggregate structure and composition and also use that knowledge to advance the development of process scale models of heteroaggregation. The first aim of this study is to develop a population balance model (PBM) for the second stage of the heteroaggregation process or the agglomeration stage to predict final heteroaggregate particle size distribution (PSD). The model is also used to study the effect of different parameters on the important forces in the system such as electrostatic, van der Waals and hydration force to understand factors that lead to a faster agglomeration dynamics. The model is validated by comparing with experimentally measured final heteroaggregate PSD. The second objective of this work is to develop a model for the first stage of the heteroaggregation process or the layering stage where smaller nanoparticles layer on a larger microparticle and affect its properties, thereby making it more susceptible to aggregation with other such particles in the second stage of heteroaggregation. The model results are compared with the experimental study of monoaggregate structure performed by scanning electron microscopic imaging of the same. This is essential for understanding factors that regulate and limit layering, and in turn affect the monoaggregate distribution and consequently heteroaggregate PSD and the presence of different heteroaggregate regimes. Furthermore, these two models are combined to develop an integrated model for both stages of the heteroaggregation process. The progress of the system towards different heteroaggregation regimes have also been simulated and validated experimentally by studying the final heteroaggregate PSD. The third aim of this study is to investigate the adsorption characteristics of the heteroaggregates for the adsorption of oppositely charged heavy metal ions from single ion as well as mixed ion systems which represent real industrial wastewater more accurately than commonly studied single ion systems. The adsorption capacities of the heteroaggregates from three different regimes are also compared with the adsorption characteristics of the individual components of the heteroaggregates to see if the heteroaggregates offer an advantage over the

individual adsorbents. The bio-friendly nature, oppositely charged components and an adsorption capacity comparable to that of industrially popular adsorbents make this system a good choice to replace commonly used adsorbents in the future. This study is expected to advance the field of heteroaggregation by answering some of its most fundamental questions and at the same time aid in the utilization of this knowledge to progress towards the production and use of heteroaggregates in real life applications.

Acknowledgements

You can know the name of a bird in all the languages of the world, but when you are finished, you will know absolutely nothing whatever about the bird. So let's look at the bird and see what it's doing - that's what counts.

Let me start by a little name-dropping and thanking Dr. Richard Feynman for teaching me to be inquisitive through his books, which got me into this mess in the first place.

Since this is a PhD dissertation, I should first thank the people who spent the most amount of time thinking about these research problems except me, my advisers, Prof. Nina Shapley and Prof. Rohit Ramachandran. Hopefully I haven't completely wasted all the time, effort and research funding that you spent on me. I have seen firsthand, literally, how a doubtful, anxious, young researcher that came to Rutgers, has become (hopefully) a better and slightly more confident researcher over these 5 years and that is largely due to the things that I have learned and acquired consciously or unconsciously from you. Both of you have given me the utmost freedom to plan my work and have always encouraged me, gave me confidence. I also want to thank you for allowing me to work on so many different projects from different areas and encouraging me to go for the internship at Genentech. Those experiences enriched me a lot. Prof. Ramachandran has taught me to be less worried, more productive, and independent in taking research related decisions. Prof. Shapley is one of the nicest persons I have ever met in my life. She has also always given me confidence when I needed it, offered guidance and help in current, and future work related issues. I am so glad that you were my advisers. I would also like to thank my dissertation committee members: Prof. Masanori Hara, Prof. Yee Chiew and Prof. John Reinfelder for sharing valuable

feedback and suggestion on my dissertation.

I want to thank some other colleagues who contributed to my thesis related and non-thesis research directly. I want to thank Chinmay for his help with the laser diffraction experiments and particle synthesis. I want to thank Sanyukta for the countless hours she spent helping me with the adsorption experiments. I want to thank Chandra for building the foundation for the dry binder model. I want to thank Indu for her past and future help with the Evonik granulation paper. I want to thank Franklin for doing a great job on the parallelization paper and including me in it. I also want to thank Tulsi for her help with optical microscopy and Dr. Berra Beyoglu for her help with SEM analysis. I want to thank Shashank, Indu, Yuktesh and Chaitanya for proofreading the thesis.

I also want to thank my friend and closest office neighbor for the longest time, Ashu. I have learned many things from you and I hope you have gotten some things from me too, and, thanks for all the ‘open air discussions’, those were great fun. Next up is my current closest office neighbor, Subhodh. Honestly, you surprise me again and again by showing me how helpful a person can be. Thanks for all the help and support and for keeping the football discussions alive after Sarang left.

I want to thank my two special seniors in the lab: Maitraye*di*, Anwesh*adi*. You two made my life so much easier when I joined Rutgers. Thanks for all your unconditional help. I also want to thank Kun, Kristin, Kapil from Dr. Shapley’s group and Sarang, Dana, Shashank, Yuktesh, Chaitanya from Dr. Ramachandran’s group.

The other person without whom this would not have been possible is my childhood friend, and now my wife, Remi. Without your support and insistence, I would probably have given up on academia long ago and become a revolutionary or a monk. Thank you for your wise counsel and listening patiently to my work-related rants when I needed to vent.

I also want to thank my *baba-ma* who shaped very early in my life the kind of person I was going to become and have now become. I am so lucky to have gotten many of the principles that I proudly follow in life from you.

Table of Contents

Abstract	ii
Acknowledgements	v
List of Tables	xi
List of Figures	xii
1. Background	1
2. Development and experimental validation of a model for the agglomeration stage of the heteroaggregation process	9
2.1. Background & objectives	9
2.2. Development of a population balance model for the agglomeration stage of the heteroaggregation process	12
2.2.1. Mathematical model development	12
2.2.2. Results & discussion	17
2.2.2.1. Effect of process parameters on electrostatic interaction	17
2.2.2.2. Effect of process parameters on van der Waals interaction	21
2.2.2.3. Effect of process parameters on hydration interaction	22
2.2.2.4. Effect of process parameters on total interaction potential	24

2.2.2.5.	Effect of relative alginate & chitosan concentration on final heteroaggregate size distribution . .	28
2.2.2.6.	Effect of relative alginate & chitosan concentration on final heteroaggregate composition	31
2.3.	Experimental investigation of heteroaggregate particle size distribution	33
2.3.1.	Experimental procedure	33
2.3.1.1.	Materials & instruments	33
2.3.1.2.	Chitosan nanoparticle preparation	33
2.3.1.3.	Alginate microparticle preparation	34
2.3.1.4.	Heteroaggregation experiments	34
2.3.2.	Results & discussion	35
2.4.	Chapter conclusions	37
3.	Development and experimental validation of a model for the layering stage of the heteroaggregation process	40
3.1.	Background & objectives	40
3.2.	Development of a model for the layering stage of the heteroaggregation process	44
3.2.1.	Mathematical model development	44
3.2.2.	Results & discussion	49
3.3.	Experimental study of layering	55
3.3.1.	Experimental procedure	55
3.3.2.	Results & discussion	55
3.4.	Development and experimental validation of an integrated heteroaggregation process model	59
3.4.1.	Mathematical model development	59
3.4.2.	Results & discussion	62

3.5. Chapter conclusions	63
4. Study of adsorption characteristics of alginate, chitosan and heteroaggregates for the adsorption of positive & negative heavy metal ions	66
4.1. Background & objectives	66
4.2. Experimental procedure	73
4.2.1. Materials	73
4.2.2. Instruments	74
4.2.3. Preparation of alginate bead	74
4.2.4. Heteroaggregation experiments	75
4.2.5. Equilibrium adsorption experiments	75
4.2.6. ICP-OES analysis	77
4.2.7. Particle characterization	78
4.3. Results & discussion	78
4.3.1. Particle characterization	78
4.3.2. Equilibrium adsorption capacity	79
4.3.2.1. Comparison between adsorbents	79
4.3.2.2. Comparison between solutes	84
4.4. Chapter conclusions	91
5. Conclusions and future directions	94
5.1. Conclusions	94
5.2. Future directions	98
Bibliography	103

List of Tables

2.1. Parametric values for the agglomeration model	16
3.1. Parameters for the layering model	49
4.1. Coefficient of determination and model constants for Langmuir and Freundlich isotherms	90

List of Figures

1.1.	Interactions between different kind of particles in the system . . .	5
1.2.	Schematic of the three stages of the heteroaggregation process: [a] Mono-dispersed alginate and chitosan particles; [b] Formation of <i>monoaggregates</i> (individual alginate microparticles coated with multiple chitosan nanoparticles); [c] Formation of <i>heteroaggregates</i> (multiple monoaggregates agglomerated together)	7
2.1.	Effect of different parameters on electrostatic interaction potential	18
2.2.	Effect of different parameters on van der Waals interaction potential	21
2.3.	Effect of different parameters on hydration interaction potential .	23
2.4.	Effect of (a)-(b) inter-particle distance and (c) particle radius ratio on van der Waals, electrostatic and total interaction potential ES : electrostatic interaction potential; VDW : van der Waals in- teraction potential; Total : total interaction potential. <i>Identically</i> : both particles have either positive or negative surface potential of denoted magnitude; <i>Opposite</i> : particles have opposite surface potential of denoted magnitude	27
2.5.	Model estimated variation of final heteroaggregate particle size dis- tribution for different chitosan and alginate amount. <i>Correspond-</i> <i>ing chitosan volume fraction of the samples: 0.004 (0.1 g alginate-</i> <i>10 μl chitosan), 0.077 (0.1-200), 0.144 (0.1-400), 0.251 (0.1-800),</i> <i>0.335 (0.1-1200), 0.502 (0.1-2400), 0.002 (0.2-10), 0.0.04 (0.2-</i> <i>200), 0.077 (0.2-400), 0.144 (0.2-800), 0.201 (0.2-1200), 0.335</i> <i>(0.2-2400)</i>	29

2.6.	Model estimated variation of D_{10} , D_{50} and D_{90} with chitosan amount for 0.1 g and 0.2 g of alginate	31
2.7.	Variation of final fractional chitosan content for different amount of chitosan and alginate	31
2.8.	Experimentally observed variation of final heteroaggregate particle size distribution for different chitosan and alginate amount. <i>Corresponding chitosan volume fraction of the samples: 0.004 (0.1 g alginate-10 μl chitosan), 0.077 (0.1-200), 0.144 (0.1-400), 0.251 (0.1-800), 0.335 (0.1-1200), 0.502 (0.1-2400), 0.002 (0.2-10), 0.0.04 (0.2-200), 0.077 (0.2-400), 0.144 (0.2-800), 0.201 (0.2-1200), 0.335 (0.2-2400)</i>	35
2.9.	Experimentally observed variation of D_{10} , D_{50} and D_{90} with chitosan amount for 0.1 g and 0.2 g of alginate	37
3.1.	Surface potential of a monoaggregate with percentage surface area covered by chitosan nanoparticles	50
3.2.	Validation of the layering model by comparison of experimentally acquired heteroaggregate PSD with monoaggregate number distribution for alginate amount of 0.1 g	52
3.3.	Validation of the layering model by comparison of experimentally acquired heteroaggregate PSD with monoaggregate number distribution for alginate amount of 0.2 g	54
3.4.	SEM images of alginate beads with chitosan layering on it at 200X magnification	56
3.5.	SEM images of an alginate bead	57
3.6.	SEM images of an alginate bead from a system of 0.1 g alginate beads with 10 μ l chitosan	57
3.7.	SEM images of an alginate bead from a system of 0.1 g alginate beads with 400 μ l chitosan	58

3.8. SEM images of an alginate bead from a system of 0.1 g alginate beads with 2000 μl chitosan	58
3.9. Combined PBM and layering model estimated variation of D_{10} , D_{50} and D_{90} with chitosan amount for 0.1 g and 0.2 g of alginate	63
4.1. Different heteroaggregation regimes: “Dispersed, uncoated” (individual alginate microparticles ‘under coated’ with chitosan nanoparticles); “Dispersed, coated” (individual alginate microparticles ‘over coated’ with chitosan nanoparticles); “Agglomerated” (multiple alginate microparticles coated with chitosan nanoparticles agglomerated together)	68
4.2. Structure of the biopolymers used in this study	69
4.3. Chelation models (Monteiro and Airoidi, 1999)	70
4.4. Structure of calcium alginate beads according to the “egg-box” model (Braccini and Perez, 2001)	71
4.5. Schematic showing the design of experiments	77
4.6. Optical microscope image of alginate beads	78
4.7. Adsorption of copper on various adsorbents. <i>Alginate-Cu</i> represents the adsorption of copper on alginate. <i>Chitosan-Cu</i> represents the adsorption of copper on chitosan. $H_{10}\text{-Cu}$, $H_{400}\text{-Cu}$ and $H_{2000}\text{-Cu}$ respectively represent the adsorption of copper on heteroaggregates with 10, 400 and 2000 μl of chitosan.	80
4.8. Adsorption of molybdenum on various adsorbents. <i>Chitosan-Mo</i> represents the adsorption of molybdenum on chitosan. $H_{10}\text{-Mo}$, $H_{400}\text{-Mo}$ and $H_{2000}\text{-Mo}$ respectively represent the adsorption of molybdenum on heteroaggregates with 10, 400 and 2000 μl of chitosan.	81

4.9.	Adsorption of copper from a mixture of copper and molybdenum ions on various adsorbents. <i>Chitosan-Cu(+Mo)</i> and <i>Alginate-Cu(+Mo)</i> represent the adsorption of copper on chitosan and alginate respectively. <i>H₁₀-Cu(+Mo)</i> , <i>H₄₀₀-Cu(+Mo)</i> and <i>H₂₀₀₀-Cu(+Mo)</i> respectively represent the adsorption of copper on heteroaggregates with 10, 400 and 2000 μ l of chitosan.	83
4.10.	Adsorption of molybdenum from a mixture of copper and molybdenum ions on various adsorbents. <i>Chitosan-Mo(+Cu)</i> and <i>Alginate-Mo(+Cu)</i> represent the adsorption of molybdenum on chitosan and alginate respectively. <i>H₁₀-Mo(+Cu)</i> , <i>H₄₀₀-Mo(+Cu)</i> and <i>H₂₀₀₀-Mo(+Cu)</i> respectively represent the adsorption of molybdenum on heteroaggregates with 10, 400 and 2000 μ l of chitosan.	84
4.11.	Adsorption of various solutes on alginate. <i>Alginate-Cu(+Mo)</i> and <i>Alginate-Mo(+Cu)</i> respectively represent the adsorption of copper and molybdenum from a mixture of the same on alginate. <i>Alginate-Cu</i> represents the adsorption of copper on alginate.	85
4.12.	Adsorption of various solutes on chitosan. <i>Chitosan-Cu(+Mo)</i> and <i>Chitosan-Mo(+Cu)</i> respectively represent the adsorption of copper and molybdenum from a mixture on chitosan. <i>Chitosan-Cu</i> and <i>Chitosan-Mo</i> respectively represent the adsorption of copper and molybdenum on chitosan from single ion solutions.	86
4.13.	Adsorption of various solutes on heteroaggregates from three different regimes. <i>H₋-Cu(+Mo)</i> and <i>H₋-Mo(+Cu)</i> respectively represent the adsorption of copper and molybdenum from a mixture on the heteroaggregates. <i>H₋-Mo</i> and <i>H₋-Cu</i> respectively represent the adsorption of molybdenum and copper on the heteroaggregates.	89

Chapter 1

Background

Colloidal particles suspended in liquid medium have a tendency to aggregate due to attractive van der Waals force. When these particles are charged, they are also subject to electrostatic double layer attraction or repulsion force depending on the electrostatic surface charge of the particles. For hydrophilic particles in water, the water molecules that are attached to the particles as a result of their hydrophilicity gives rise to an additional hydration force. A combination of these forces produces aggregates which are loosely divided into two categories: homoaggregates and heteroaggregates. Homoaggregates are aggregates of one kind of particles and heteroaggregates are aggregates of particles that differ in various attributes such as size, electrical surface charge etc.

Traditionally, heteroaggregation has been used to separate charged particles from solutions through precipitation by adding oppositely charged particles. Added particles with the opposite charge neutralize the surface charge of existing particles. This causes these neutral particles to aggregate with each other due to the attractive van der Waals force. At the other end it has been used to stabilize colloidal solutions of negligibly charged microspheres by introducing highly charged nanoparticles in the solution and forming nanoparticle ‘halos’ (i.e., a layer of nanoparticles on microspheres) (Tohver et al., 2001). Due to the layer of highly charged nanoparticles on the microspheres, these aggregates attain a similar surface charge and repel each other due to the electrostatic force instead of agglomerating.

More recently, core-shell particles, produced by heteroaggregation have been used for xerography, printing ink where micron sized polymer core is coated with nanosized pigments. These toner particles are required to have a very narrow particle size distribution (PSD) and a homogeneous composition distribution (Turner et al., 2011). Conventional mechanical production processes of toner particles involve milling of a solid block of toner and generate particles with a wide PSD and produce significant amount of dust. The shortcomings of the traditional method gave rise to the development of a chemical production method. In the chemical method, pigments are added to latex particles and then these particles are flocculated by lowering the pH of the solution. As the pH of the solution is lowered, negatively charged latex particles become neutral and aggregate due to van der Waals force. This uncontrolled aggregation produces a gel which is then mechanically broken into toner particles of desired size. Recently a more advanced method has been developed where the heteroaggregation technique is applied by adding a coagulating agent instead of lowering the pH to have a controlled aggregation of the latex particles (Ahuja et al., 2007).

Heteroaggregates have also been suggested for drug delivery applications. Sarmiento et al. (2007) showed that the insulin uptake capacity increased when it was entrapped in alginate or chitosan nanoparticles as the alginate or chitosan adhered to the mucous wall of the gastrointestinal tract, provided protection to the drug molecule and allowed for the transport of insulin to the blood circulation system. Bodmeier and Paeratakul (1989); Ostberg and Graffner (1994) also proposed the use of calcium alginate beads to entrap water insoluble drugs to make the drug molecules freely movable in an aqueous environment. However, erosion of the alginate matrix accelerated the release of drugs (Murata et al., 1993b). Later, Murata et al. (1993a); Sezer (1999); Sezer and Akbuga (1999) found that alginate beads coated with chitosan had a higher drug loading capacity and also the layer of chitosan reduced the erosion of the gel matrix. Positively charged chitosan

particles have also been suggested to be a good carrier for DNA delivery since they form complexes with negatively charged plasmid DNA. Although, to be used for drug delivery application it is required for these particles to have a specific size and structure (Kim et al., 2001).

Customized heteroaggregates can also be used for water purification applications (Yu et al., 2013). This is based on the idea that oppositely charged components of the heteroaggregates will adsorb toxic anions and cations which include charged heavy metal compounds such as cadmium, mercury, lead, copper, chromium and arsenic from waste-water.

The property of the heteroaggregates depend not only on the material properties of the primary component particles but also the size, composition and surface charge. Therefore, it is very crucial to understand the mechanism of heteroaggregation and to be able to control aggregation and form heteroaggregates of desired size and composition tailored for use in the areas mentioned before.

The colloidal system chosen for this particular work comprises of alginate and chitosan. Chitosan which is derived from chitin found in crustacean cells and alginate which is produced from algae and certain bacteria, are abundant, biocompatible and environment-friendly. As mentioned before, chitosan and alginate are popular biopolymers which have been used in drug delivery applications (Murata et al., 1993a; Sezer, 1999; Sezer and Akbuga, 1999; Sarmiento et al., 2007). Moreover, in the gel particle form both alginate and chitosan show comparable metal ion adsorption capability to that of more popularly used ion exchange resins (Yu et al., 2013).

Previous research (both modeling and experimental) has been mainly focused on the aggregation of one kind of rigid colloidal particles whereas, alginate and chitosan are oppositely charged, very different in terms of size (alginate microparticles are about 130 times and alginate beads are about 10000 times bigger than the chitosan nanoparticles) and are not rigid particles. These make the system

studied in this work more complex than commonly studied colloidal systems.

The interactions between different kind of particles in this system is shown in the Figure 1.1. For alginate-alginate, since both the particles are negatively charged there is a strong repulsive electrostatic force which dominates over the weak van der Waals attraction. For chitosan-chitosan, similarly there is a strong electrostatic repulsion which dominates over the van der Waals attraction. In the case of alginate-chitosan particles the opposing charges result in a strong electrostatic attraction along with the weak van der Waals attraction. For neutral monoaggregates (where the charge of the chitosan particles attached to the alginate particle is just enough to neutralize the negative surface charge of the alginate particle) and any other type of particle the only force is weak attractive van der Waals force. For negatively charged monoaggregates (where the positive charge of the all chitosan particles attached to the negatively charged alginate is less than the surface charge of the alginate particle) and any other kind of particle the forces in play are strong or weak (depending on the negative charge of the monoaggregate) electrostatic attraction or repulsion (depending on whether the other particle is charged and positively or negatively) and attractive van der Waals force. For positively charged monoaggregates (where the positive charge of the chitosan particles attached to the negatively charged alginate is more than the surface charge of the alginate particle) similarly the forces are van der Waals attraction and electrostatic attraction or repulsion (except when the other particle is neutral).

These forces facilitate the aggregation of monodispersed alginate and chitosan particles and ultimately the formation of heteroaggregates mainly in two steps. As shown in Figure 1.2, in step [a], the alginate and chitosan particles are monodispersed at the start of the process. In the next step ([b]) due to attractive forces between alginate-chitosan and repulsive force between alginate-alginate and chitosan-chitosan, the chitosan particles start to attach to the alginate particles.

































PARTICLE I		PARTICLE II		INTERACTION	PARTICLE I		PARTICLE II		INTERACTION
<i>Alginate</i>			<i>Alginate</i>	Strong Repulsion	<i>Negatively Charged Monoaggregate</i>			<i>Chitosan</i>	Partially Charge Dependent Attraction
<i>Chitosan</i>			<i>Chitosan</i>	Strong Repulsion	<i>Negatively Charged Monoaggregate</i>			<i>Negatively Charged Monoaggregate</i>	Completely Charge Dependent Repulsion
<i>Alginate</i>			<i>Chitosan</i>	Strong Attraction	<i>Negatively Charged Monoaggregate</i>			<i>Neutral Monoaggregate</i>	Weak Attraction
<i>Neutral Monoaggregate</i>			<i>Alginate</i>	Weak Attraction	<i>Negatively Charged Monoaggregate</i>			<i>Positively Charged Monoaggregate</i>	Completely Charge Dependent Attraction
<i>Neutral Monoaggregate</i>			<i>Chitosan</i>	Weak Attraction	<i>Positively Charged Monoaggregate</i>			<i>Chitosan</i>	Partially Charge Dependent Repulsion
<i>Neutral Monoaggregate</i>			<i>Negatively Charged Monoaggregate</i>	Weak Attraction	<i>Positively Charged Monoaggregate</i>			<i>Negatively Charged Monoaggregate</i>	Completely Charge Dependent Attraction
<i>Neutral Monoaggregate</i>			<i>Neutral Monoaggregate</i>	Weak Attraction	<i>Positively Charged Monoaggregate</i>			<i>Neutral Monoaggregate</i>	Weak Attraction
<i>Neutral Monoaggregate</i>			<i>Positively Charged Monoaggregate</i>	Weak Attraction	<i>Positively Charged Monoaggregate</i>			<i>Positively Charged Monoaggregate</i>	Completely Charge Dependent Repulsion

Figure 1.1: Interactions between different kind of particles in the system

The chitosan particles being significantly smaller than the alginate particles, form a layer around each alginate particle. These particles with one alginate particle at the core and many chitosan particles layered on it are referred to as monoaggregates in this dissertation. In the last step ([c]), these monoaggregates, due to the forces mentioned in Table 1.1 aggregate with each other and form bigger aggregates with multiple alginate particles and numerous chitosan particles. These particles are called heteroaggregates in this article.

With change in the relative starting concentration of alginate and chitosan, the system progresses towards different final particle size distributions. These final distributions can be divided in three regimes: ‘dispersed, uncoated’, ‘agglomerated’ and ‘dispersed, coated’:

1. When the number of chitosan particles in the system at step [a] (Figure 1.2) is less than the amount needed to completely neutralize the surface charge of all the alginate particles, most of the monoaggregates at step [b]

have negative surface charge and thus repel each other and do not form heteroaggregates. Since the alginate particles are only partially coated (complete coating represents the state when the negative charge of the alginate particle is completely neutralized by the chitosan particles attached to it) this regime is called dispersed (as opposed to ‘agglomerated’), uncoated.

2. When the number of chitosan particles in step [a] is just enough to neutralize the surface charge of all the alginate particles, in step [b] mostly neutral monoaggregates are formed which aggregate with each other to form heteroaggregates due to weak van der Waals attractive force. Since in this case in step [c] we have big heteroaggregates, this regime is called the ‘agglomerated’ regime.
3. When at the start, in step [a] there are more chitosan particles than that necessary to neutralize the surface charge of all the alginate particles, majority of the monoaggregates formed in step [b] are positively charged and thus repel each other and prevent formation of heteroaggregates. Since the alginate particles are completely or ‘over-coated’ with chitosan particles and do not form heteroaggregates, this regime is called the ‘dispersed, coated’ regime.

It is important to note that in a real system, at any moment, there will be a distribution of all three kinds of monoaggregates in step [b] and not only one kind of monoaggregate (positive or negative or neutral) although the relative number of different types of monoaggregates and consequently the final particle size distribution will be different depending on the initial relative concentration of alginate and chitosan.

The first objective of this work is to study the second stage which is the agglomeration stage of heteroaggregation by developing a mesoscale population balance model (PBM) and validating the model with experimental study of a

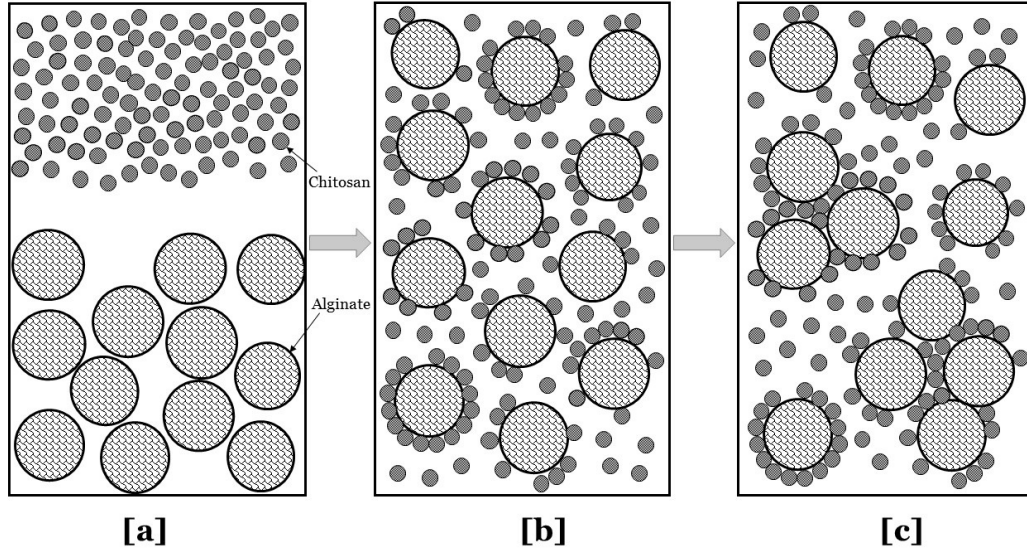


Figure 1.2: Schematic of the three stages of the heteroaggregation process: [a] Mono-dispersed alginate and chitosan particles; [b] Formation of *monoaggregates* (individual alginate microparticles coated with multiple chitosan nanoparticles); [c] Formation of *heteroaggregates* (multiple monoaggregates agglomerated together)

heteroaggregation process. PBM is a very popular tool to model particulate systems. Extensive research has been done on modeling colloidal systems using PBM (Axford, 1997; Lattuada et al., 2003, 2006; Maindarkar et al., 2012, 2013; Peukert et al., 2005; Raikar et al., 2010, 2011; Schaer et al., 2001; Sefcik et al., 2006; Soos et al., 2006). Some experimental work also has been reported on the heteroaggregation of colloidal particles (Furusawa and Velev, 1999; Schaer et al., 2001; Lattuada et al., 2003; Soos et al., 2006; Tourbin and Frances, 2007). Although some studies have investigated this phenomenon of the progress of a system towards different regimes during aggregation of microparticles and nanoparticles (Atmuri et al., 2013; Gilchrist et al., 2005; Zhang et al., 2008), the novelty of this study lies in dealing with alginate and chitosan which are highly hydrophilic hydrogels of opposite charge and very distinct in terms of size and in developing a PBM framework to describe the dynamics of their aggregation.

The second aim is to model the first stage or the layering stage of heteroaggregation at using a separate population balance model. The findings from these

simulations will be compared with experimental imaging of individual monoaggregates. Experimental imaging of the heteroaggregate structure using various techniques and study of layering on monoaggregates have also been reported (Fisher et al., 2001; Kim and Berg, 2000; Kim et al., 2003; Johnson and Lenhoff, 1996; Rasa et al., 2004; Yates et al., 2005). Then finally, findings from the layering model are incorporated in the agglomeration framework to develop an integrated model for both stages of the heteroaggregation process and the results from the integrated model are compared to the experimental heteroaggregate PSD.

The third goal is to study the adsorption characteristics of the heteroaggregates and its individual components alginate and chitosan for the adsorption of positive and negative ions from single ion and mixed ion systems for application in removal of heavy metal ions from wastewater. Chitosan and alginate have proven to be very good adsorbents for heavy metal ions. Therefore, the equilibrium adsorption capacity of alginate-chitosan heteroaggregates will be studied for potential application in the adsorption of heavy metals ions from industrial waste water as a more efficient alternative to individual adsorbents.

Objectives

The objectives of this dissertation are:

- **Specific aim 1:** Development and experimental validation of a model for the agglomeration stage of the heteroaggregation process
- **Specific aim 2:** Development and experimental validation of a model for the layering stage of the heteroaggregation process
- **Specific aim 3:** Study of adsorption characteristics of alginate, chitosan and heteroaggregates for the adsorption of positive & negative heavy metal ions

Chapter 2

Development and experimental validation of a model for the agglomeration stage of the heteroaggregation process

More details about the work discussed in this section can be obtained in the following article.

- **A. Chaturbedi**, C. Pathak, K. Deshpande, N. Shapley, R. Ramachandran. Population balance model development and experimental validation for the heteroaggregation of oppositely charged micro- and nano-particles. *Chemical Engineering Research & Design*, 113, 96-111, 2016

2.1 Background & objectives

As mentioned before, population balance models (PBM) are very popular for modeling particulate systems. There has been some previous work on using PBMs for modeling colloidal systems as well, although, none of those systems were as dissimilar as the one studied in this work with respect to the particles in the system. This work is built on the foundation laid out by numerous other researchers working on colloidal aggregation, especially on modeling of colloidal aggregation as outlined below.

Traditionally the formation of colloidal aggregates has been studied in the literature as kinetic processes with a kernel for purely diffusive systems. Fuchs (1934) introduced the Fuchs stability ratio to account for the effect of various

interaction forces such as van der Waals, electrostatic, hydration forces on aggregation rate. Derjaguin (1934), and subsequently Derjaguin and Landau (1993) and Verwey and Overbeek (1948) formulated the effect of van der Waals and electrostatic forces on aggregation. Much later, Axford (1997) studied the reaction-limited aggregation of colloidal silica by using a population balance model (PBM). Furusawa and Velev (1999) investigated the effects of various important parameters such as the particle size ratio, the particle zeta potential and the electrolyte concentrations on the interaction of amphoteric latex particles and silica, and succeeded in controlling the size and composition. Schaer et al. (2001) studied the aggregation kinetics of silica particle precipitation in a batch reactor and proposed a mechanism for the aggregation process. They also used a PBM to model the aggregation process. Lattuada et al. (2003) performed experiments and used a PBM for studying the reaction-limited aggregation of polymer colloids. Peukert et al. (2005) used a PBM to study the production of nanoparticles of controlled size for nanoparticle precipitation and nanomilling applications. López-López et al. (2005) modeled the binary diffusion-limited cluster-cluster aggregation of similarly sized oppositely charged particles and found out that at a relative concentration of the minority particles higher than a critical value, all initial particles formed one large cluster however with relative concentration below that value, stable aggregates were formed. Soos et al. (2006) compared their PBM results with experiments on colloidal aggregation, breakage and restructuring in turbulent flows. Sefcik et al. (2006) used a PBM to study the effect of mixing on aggregation and gelation of nanoparticles and competition between aggregation and gelation for a homogeneous system. Lattuada et al. (2006) used a PBM for modeling the aggregation between clusters. Tourbin and Frances (2007) compared several analytical technique to measure the size distribution of colloidal silica particles in suspension which were detailed in a previous work. Mao and McClements (2011) studied the heteroaggregation of oppositely charged lipid

droplets and found that the aggregate properties depend on the ratio of positive to negative droplets and pH. Raikar et al. (2010) used population balance model to predict emulsion drop size distribution for a oil-in-water simulation improving upon a previously developed model by accounting for multiple drop breakage instead of a breakage distribution function exhibiting maximum probability for the formation of two equal sized droplets. In a subsequent work, by increasing number of daughter drops formed in an event of breakage and by introducing a maximum stable diameter the model was further improved to work better for a wide range of homogenization pressures (Raikar et al., 2011). To predict the drop size distribution at industrially acceptable high oil-to-surfactant ratio Maindarkar et al. (2012) developed a population balance breakage-coalescence model in place of established breakage-only model. This model was advanced to predict drop size distribution for different surfactant types and concentration (Maindarkar et al., 2013). PBM also has been used to model the viscosity of suspension of highly anisotropic nanoparticles during aggregation (Puisto et al., 2012), to model the aggregation of solid lipid nanoparticles (Yang et al., 2012), to study the aggregation kinetics and effect of cluster size and structure on aggregation kinetics for aggregation of rigid colloidal particles (Babler et al., 2010). Atmuri et al. (2013) performed experiments with latex particles at different salt and particle concentration and compared the experimental results with PBM results.

Objectives

The objectives of the work outlined in this chapter are:

- **Sub aim 1:** Development of a PBM framework for the second stage ([b]-[c])

in Figure 1.2) of the two stage heteroaggregation process of alginate microparticles and chitosan nanoparticles in which the monoaggregates (nanoparticle coated microparticles) aggregate with each other to form heteroaggregates after the partial or complete charge neutralization through layering of positively charged chitosan nanoparticles on negatively charged alginate microparticles in the first stage ([a]-[b] in Figure 1.2)

- **Sub aim 2:** Experimental investigation of the final particle size distribution at the end of the heteroaggregation process to validate and calibrate the model

2.2 Development of a population balance model for the agglomeration stage of the heteroaggregation process

2.2.1 Mathematical model development

The equation for the calculation of rate of particle transfer between different size classes based on the population balance model is as follows:

$$\frac{\partial}{\partial t}N(a, c, t) = R_{form}(a, c) - R_{dep}(a, c) \quad (2.1)$$

$$R_{form}(a, c) = \frac{1}{2} \int_0^a \int_0^c K(a', a - a', c', c - c') N(a', c', t) N(a - a', c - c', t) da' dc \quad (2.2)$$

$$R_{dep}(a, c) = N(a, c, t) \int_0^{a_{max}-a} \int_0^{c_{max}-c} K(a', a, c', c) N(a', c', t) da' dc \quad (2.3)$$

where, $N(a, c, t)$ is number of aggregates of alginate volume a and chitosan volume c at time t , $R_{form}(a, c)$ and $R_{dep}(a, c)$ are respectively the rates of formation and depletion of particles of alginate volume a and chitosan volume c due to aggregation only. For this work, the other rate processes that affect the formation and depletion rates such as the breakage of the aggregates, consolidation in which due to shear the aggregates are consolidated and layering in which smaller particles form a layer around the bigger particles in the system are neglected.

$K(a', a, c', c)$ is the aggregation rate kernel between two aggregates with alginate and chitosan volume of a', c' and a, c respectively. It is important to note that all particles in the system are assumed to be spherical and the diameter and the radius of the particles are calculated from the volume with this assumption. For the monoaggregates and heteroaggregates, which are aggregates of different amount of alginate and chitosan, the total volume is calculated by adding the volume of alginate and chitosan in that particle and the diameter and the radius are calculated from the volume.

For a pure diffusion-limited aggregation in dilute systems, the aggregation kernel can be represented by the Brownian kernel which is of the form (Schmitt et al., 2000):

$$K(a', a, c', c) = 4\pi(D_{(a,c)} + D_{(a',c')})(R_{(a,c)} + R_{(a',c')}) \quad (2.4)$$

where, $R_{(a,c)}$ is the radius of the particle of alginate volume a and chitosan volume c . The diffusion coefficient $D_{(a,c)}$ can be represented by the Stokes-Einstein relationship:

$$D_{(a,c)} = \frac{kT}{6\pi\mu R_{(a,c)}} \quad (2.5)$$

where, k is the Boltzmann constant, T is temperature and μ is viscosity of the medium. Substituting the expression of $D_{(a,c)}$ from Equation 2.5 in Equation 2.4 we get:

$$K(a', a, c', c) = \frac{K_B(R_{(a,c)}^{-1} + R_{(a',c')}^{-1})(R_{(a,c)} + R_{(a',c')})}{4} \quad (2.6)$$

where, $K_B = 8kT/3\mu$ is the collision rate constant for monoaggregates due to Brownian motion for diffusion-limited aggregation. If this process is not diffusion-limited then dividing the aggregation rate by the Fuchs stability ratio W , we get the actual rate (Axford, 1997):

$$K(a', a, c', c) = K_0 \frac{K_B}{W(a', a, c', c)} \frac{(R_{(a,c)}^{-1} + R_{(a',c')}^{-1})(R_{(a,c)} + R_{(a',c')})}{4} \quad (2.7)$$

where, K_0 is the aggregation kernel constant.

The Fuchs Stability Ratio is the ratio of aggregation rate in the presence of various particles interactions such as electrostatic, van der Waals, hydration interaction to the aggregation rate in absence of any such interactions. It can be expressed as a function of total interaction potential energy between two aggregates U , the thermal energy kT , the dimensionless center-to-center distance $L(l)$ ($L(l) = r(l)/A((a', a, c', c))$, where r is the distance between the centers of the aggregating particles and A is the average radius of the aggregating particles ($A((a', a, c', c)) = (R_{(a,c)} + R_{(a',c')})/2$) and the hydrodynamic resistance, $G(a', a, c', c, l)$ experienced by the approaching particles due to the dispersion of fluid between them.

$$W(a', a, c', c) = 2 \int_2^\infty \frac{\exp(U(a', a, c', c, l)/kT)}{G(a', a, c', c, l)L(l)^2} dL \quad (2.8)$$

The hydrodynamic resistance was not taken into consideration in this work.

According to the DLVO theory (Derjaguin and Landau, 1993; Verwey and Overbeek, 1948), the total interaction energy is the sum of interaction energies from van der Waals, electrostatic and in this case also hydration interaction:

$$U = U_{van\ der\ Waals} + U_{electrostatic} + U_{hydration} \quad (2.9)$$

where, $U_{van\ der\ Waals}$ is the interaction potential due to van der Waals attraction, $U_{electrostatic}$ is the interaction potential due to electrostatic repulsion or attraction depending on the surface charges of the aggregating particles and $U_{hydration}$ is the hydration interaction energy, generated from the attaching of water molecules to the surface of the particles that need to be displaced during aggregation.

The Hamaker relation for calculation of van der Waals interaction potential

is (Elimelech et al., 1995):

$$U_{van\ der\ Waals}(a', a, c', c, l) = -\frac{A_H}{6} \times \left\{ \frac{8\omega(a', a, c', c)}{(1 + \omega(a', a, c', c))^2} \left[\frac{1}{(L(l)^2 - 4)} + \frac{1}{L(l)^2 - 4\left(\frac{1-\omega(a', a, c', c)}{1+\omega(a', a, c', c)}\right)^2} \right] + \ln \left[\frac{L(l)^2 - 4}{L(l)^2 - 4\left(\frac{1-\omega(a', a, c', c)}{1+\omega(a', a, c', c)}\right)^2} \right] \right\} \quad (2.10)$$

where, A_H is the Hamaker constant, $\omega(a', a, c', c) (= R_{(a',c')}/R_{(a,c)})$ is the ratio of radii of aggregating particles, $L(l)$ is dimensionless center-to-center distance.

The expression for electrostatic interaction potential as developed by Sader et al. (1995):

$$U_{electrostatic}(a', a, c', c, l) = \frac{4\pi\epsilon_0\epsilon_r\omega(a', a, c', c)A(a', a, c', c)\psi_{(a,c)}^2}{(1 + \omega(a', a, c', c))^2 L(l)} \times \left\{ (1 + \Psi(a', a, c', c))^2 \ln(1 + \exp[-\kappa A(a', a, c', c)(L(l) - 2)]) + (1 - \Psi(a', a, c', c))^2 \ln(1 - \exp[-\kappa A(a', a, c', c)(L(l) - 2)]) \right\} \quad (2.11)$$

where, $\Psi(a', a, c', c) (= \frac{\psi(a',c')}{\psi(a,c)})$ is the ratio of surface potential of the two colliding particles; $\epsilon_0\epsilon_r$ is the permittivity of the dispersant and $\kappa (= \sqrt{\frac{e^2 N_A \sum_n z_n^2 C_n^b}{\epsilon_0 \epsilon_r k T}})$ is the Debye-Huckel parameter. Where, e is the electron charge, N_A is the Avogadro number, z_n and C_n^b are valance and bulk concentration of species (ion) n .

For the hydration energy, by applying the Derjaguin approximation to the typical exponential relation $F_{hyd} = F_0 \exp[-\frac{h}{\delta_0}]$ as shown in Israelachvili (1992) we get:

$$U_{hydration}(a', a, c', c, l) = \frac{4\pi\omega(a', a, c', c)A(a', a, c', c)}{(1 + \omega(a', a, c', c))^2} \times F_0 \delta_0^2 \exp\left(-\frac{A(a', a, c', c)}{\delta_0}(L(l) - 2)\right) \quad (2.12)$$

where, F_0 is the hydration force constant and δ_0 is the decay length.

Since values of some of the physical constants are not available in the literature for a similar system, they were assumed to have reasonable values within the feasible parametric space and are shown in Table 2.1.

Table 2.1: Parametric values for the agglomeration model

Parameter	Symbol	Value	Units
Boltzmann constant	k	$1.3806488 \times 10^{-23}$	$m^2 \text{ kg } s^{-2} K^{-1}$
Charge of electron	e	$1.60217657 \times 10^{-19}$	<i>Coulombs</i>
Avogadro Number	N_A	6.0221413×10^{23}	—
Hamaker constant	A_H	3×10^{-21}	<i>J</i>
Hydration force constant	F_0	10^{-2}	$N \text{ m}^{-1}$
Temperature of the medium	T	298	<i>K</i>
Viscosity of the medium	μ	0.8999×10^{-3}	<i>Pa.s</i>
Permittivity of the medium	$\epsilon_0 \epsilon_r$	6.93×10^{-10}	$C^2 \text{ N}^{-1} \text{ m}^{-2}$
Valence of ions in medium	z	1	—
Bulk concentration of ions in medium	C^b	1×10^{-2}	$kg \text{ m}^{-3}$
Debye length	$\frac{1}{\kappa}$	1.3581×10^{-7}	<i>m</i>
Decay length	δ_0	6×10^{-10}	<i>m</i>
Density of alginate	$\rho_{alginate}$	1050	$kg \text{ m}^{-3}$
Density of chitosan	$\rho_{chitosan}$	1000	$kg \text{ m}^{-3}$
Surface potential of alginate	$\Psi_{alginate}$	-46×10^{-3}	<i>Volts</i>
Surface potential of chitosan	$\Psi_{chitosan}$	40×10^{-3}	<i>Volts</i>
Volume of the system	V	10×10^{-6}	m^3
Volume of the smallest alginate bin	a_1	1.5×10^{-17}	m^3
Volume of the smallest chitosan bin	c_1	0.3×10^{-17}	m^3
Aggregation kernel constant	K_0	5×10^9	—
Simulated process time	t	10	<i>s</i>
Simulation time-Step	dt	0.01	<i>s</i>

Numerical method

The numerical stability of a PBM is a complex process due to the presence of multiple dimensions and inherent possibility of instability involved with the time-step of the integration step. The ordinary differential equations (ODE) as shown in Equation 2.1 for different particle size combinations is integrated simultaneously using the first order Euler integration technique which is popularly used to solve multidimensional PBMs (Barrasso et al., 2015; Barrasso and Ramachandran, 2015; Chaudhury et al., 2014, 2015). The time-step was chosen such that the rate of particles leaving a particular size class (bin) is not greater than the number of particles in that size class at any time-step based on the Courant-Friedrichs-Lewy

(CFL) condition as mentioned in Ramachandran and Barton (2010). The value of the time-step used is given in Table 2.1. The process time was set as 10 seconds, since no significant change was observed in the PSD after that time.

For the different possible sizes of particles (indicated by the volume of alginate; a and chitosan; c) a nonlinear grid is used to cover the broad size ranges of particles. Since this work considers the monoaggregates as starting particles, comparable volume for both alginate and chitosan is used, though the diameter of individual alginate and chitosan particles are different by an order of 3. The volume bins are expressed as shown in 2.13 & 2.14:

$$a_i = a_1 \times 3^{i-1} \quad (2.13)$$

$$c_i = c_1 \times 3^{i-1} \quad (2.14)$$

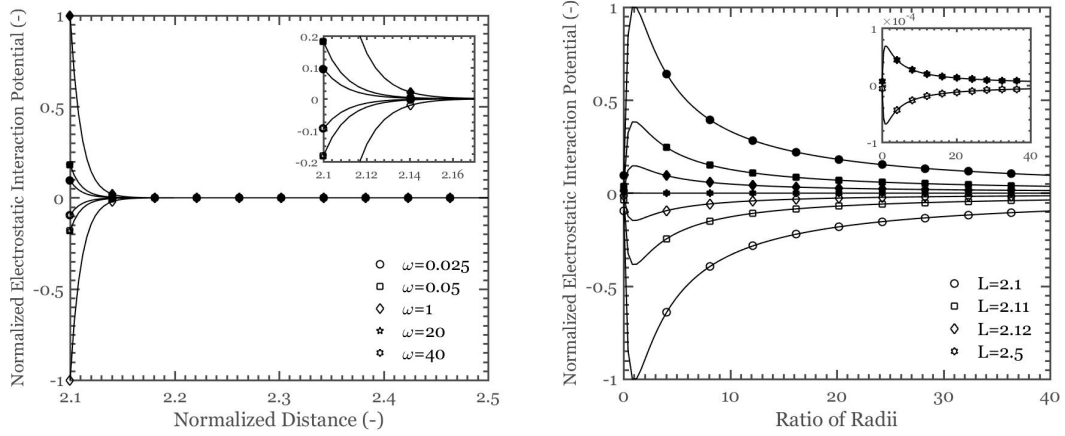
Where, a_1 and c_1 respectively are the volumes of smallest alginate and chitosan bins and shown in Table 2.1. Since a nonlinear grid is used aggregates can have volume that lie between the predefined bins. The cell average method as developed by Kumar et al. (2006) for 1-dimensional case and subsequently extended by Chaudhury et al. (2013) for multidimensional cases is used to distribute particles formed in different bins by applying a multidimensional lever rule.

All simulations were performed in Mathworks MATLAB® R2015a on an Intel Core i7-4770 CPU (3.4 GHz) with 12 GB of RAM.

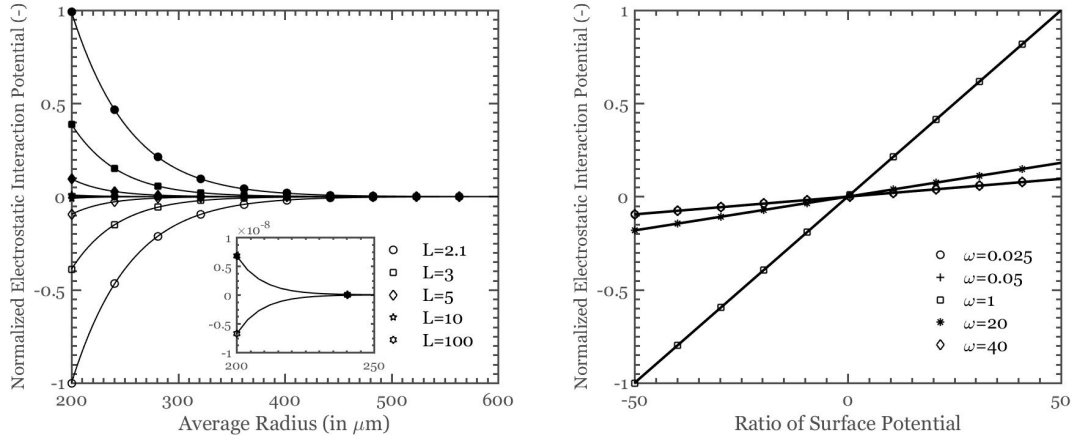
2.2.2 Results & discussion

2.2.2.1 Effect of process parameters on electrostatic interaction

As shown in Equation 2.11 the electrostatic interaction depends on the medium (i.e., permittivity), the relative size (i.e., radius ratio); the size (i.e., average radius) of the aggregating particles, the distance between them (i.e., normalized distance), the ratio of surface charge (i.e., surface potential ratio) and the ions



(a) Effect of distance between particles for different size ratio (b) Effect of the size ratio of particles for particles at different distances



(c) Effect of average size of particles for different distances (d) Effect of ratio of surface potential of aggregating particles for different size ratio

Figure 2.1: Effect of different parameters on electrostatic interaction potential

in the system (i.e., Debye-Huckel parameter). Since the medium in this system is deionized water, the permittivity and the Debye-Huckel parameter are kept constant at $6.93 \times 10^{-10} C^2 N^{-1} m^{-2}$ and $2.3 \times 10^5 m^{-1}$ respectively and the radius ratio was varied from 0.025 to 40, similarly the average radius is varied from $20 \mu m$ ($2 \times 10^{-5} m$) to $800 \mu m$ ($8 \times 10^{-4} m$), the normalized distance is varied from 2.1 to different normal distances depending on the range of the particular interaction and the surface potential ratio is varied from -50 to 50 to study their individual effect on the electrostatic interaction.

As shown in Figure 2.1a for a constant average radius of $4.1 \times 10^{-4} \text{ m}$ (mean of the highest and lowest possible average radius), surface potential of -0.003 V (mean of the surface potential of alginate, -0.046 V and chitosan, 0.04 V) and surface potential ratio of -1 representing two particles with opposite charge of the same magnitude and 1 representing the interaction between two particles with the same charge, the magnitude of the electrostatic force decreases rapidly with inter-particle distance and becomes non-existent at a normal distance of 2.16 due to the inverse dependence on $L(1)$ in the first term in Equation 2.11. Because of the $\frac{\omega(a', a, c', c)}{(1 + \omega(a', a, c', c))^2}$ term in Equation 2.11 the rate of change of electrostatic interaction potential with distance is highest for equal sized particles that is when the radius ratio is 1 and as the size ratio increases the rate of change decreases. For a radius ratio of 20 or 0.05 the force is about 20% of the force between equal sized particles and for a radius ratio of 40 or 0.025 the force is about 10% of the force between equal sized particles when the particles are at a normal distance of 2.1 from each other. As expected, for particles with identical charge the electrostatic interaction is repulsive and the interaction potential is positive and for particles with opposite charges the potential is negative and thus the interaction is attractive.

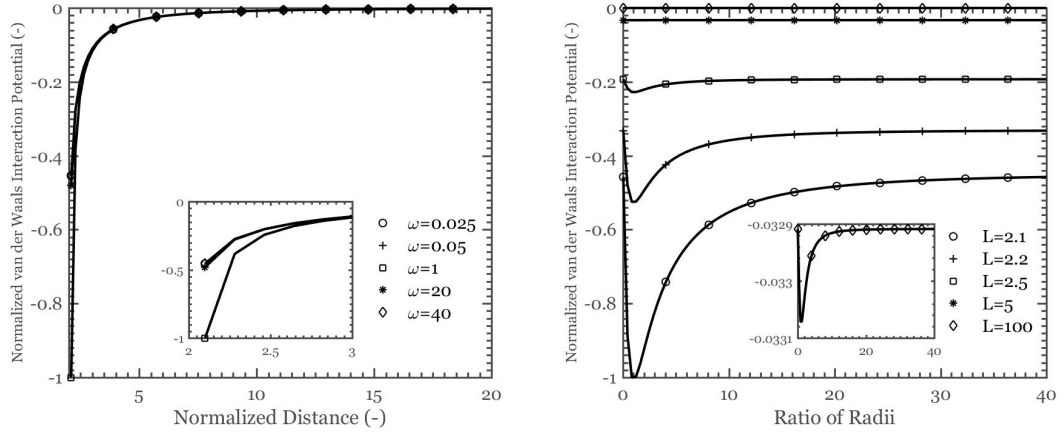
The variation of electrostatic force with radius ratio of the particles for a constant average radius of $4.1 \times 10^{-4} \text{ m}$, surface potential of -0.003 V and surface potential ratio of -1 and 1 at different normalized distances was plotted in Figure 2.1b. For the same reasons mentioned above, similarly to the behavior seen in Figure 2.1a the force is highest when the particles are of equal size (that is when the radius ratio is 1). The curves for particles at a normal distance of 2.5 are magnified to show that though the interaction potential changes similarly with radius ratio, the magnitude of the potential is less than 0.01% of the potential between equal sized particles at the closest (that is at a normal distance of 2.1).

For equal sized particles, with identical and opposite charges of the magnitude

$-0.003 V$, the electrostatic interaction potential decreases in magnitude with increasing particle size owing to the exponential terms ($\exp[-\kappa a(a', a, c', c)(L(l) - 2)]$) in Equation 2.11. As the particle size increases the magnitude of the electrostatic interaction potential becomes non-existent at even smaller distances. For example, particles with an average radius of $250 \mu m$ experience electrostatic interaction up to a normal distance of 5 but particles with an average radius of $400 \mu m$ experience electrostatic interaction only up to a normal distance of 2.1.

As seen in Figure 2.1d, at a surface potential of $-0.003 V$, normal distance of 2.1 and constant average radius of $4.1 \times 10^{-4} m$, the electrostatic interaction potential increases linearly in magnitude with increasing or surface potential ratio in either positive or negative direction. This happens as a result of the $(1 + \Psi(a', a, c', c))^2$ and $(1 - \Psi(a', a, c', c))^2$ terms in Equation 2.11. As the magnitude of $\Psi(a', a, c', c)$ increases the magnitude of these terms increase resulting in an increase in the interaction potential. Since, $\ln(1 - \exp[-\kappa a(a', a, c', c)(L(l) - 2)])$ is inherently negative, when the surface potential ratio is negative, $(1 - \Psi(a', a, c', c))^2$ dominates over $(1 + \Psi(a', a, c', c))^2$ and the interaction potential becomes negative. Similarly since $\ln(1 + \exp[-\kappa a(a', a, c', c)(L(l) - 2)])$ is inherently positive, when the surface potential ratio is positive $(1 + \Psi(a', a, c', c))^2$ dominates over $(1 - \Psi(a', a, c', c))^2$ and the electrostatic interaction potential becomes positive. Similar to Figure 2.1a the potential increases rapidly for equal sized particles (radius ratio of 1). As the size disparity increases the rate of increase of the potential with increasing surface potential decreases.

Therefore it can be concluded that the electrostatic interaction potential will be maximum when smaller, equally sized particles with different surface potential are closest to each other.



(a) Effect of distance between particles for different size ratio (b) Effect of size ratio of two particles for particles at different distances

Figure 2.2: Effect of different parameters on van der Waals interaction potential

2.2.2.2 Effect of process parameters on van der Waals interaction

The van der Waals interaction depends on the radius ratio and normalized distance between particles (Equation 2.10). The change in van der Waals interaction potential with normalized distance for different radius ratio is shown in Figure 2.2a. As expected the van der Waals interaction potential is always negative confirming that the van der Waals interaction is attractive in nature. Similar to the variation of the electrostatic force with normalized distance (Figure 2.1a) the magnitude of van der Waals force decreases with increasing distance between particles. Since van der Waals interaction has an inverse-squared dependence on distance ($[\frac{1}{(L(l)^2-4)} + \frac{1}{L(l)^2-4(\frac{1-\omega(a',a,c',c)}{1+\omega(a',a,c',c)})^2}]$ term in Equation 2.10) in place of the combined inverse and inverse-exponential dependence of electrostatic interaction potential, the former exists at even longer distances compared to the latter. Similar to the electrostatic interaction potential the van der Waals interaction potential is maximum for equal sized particles (with radius ratio of 1). At very close distance the magnitude of the van der Waals potential decreases with increasing size disparity as shown in the magnified inset plot in Figure 2.2a. As the normalized distance increases the difference between the interaction potential

for particles with different size ratio decreases and the van der Waals interaction becomes non-existent at a normalized distance greater than 15.

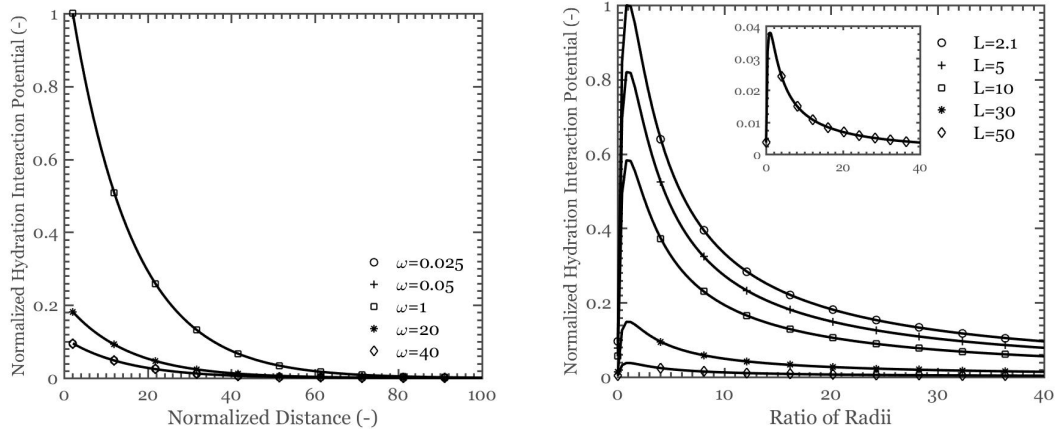
The van der Waals interaction shows a similar trend as the electrostatic force with increasing radius ratio owing to a similar dependence on radius ratio as the electrostatic interaction potential ($\frac{\omega(a',a,c',c)}{(1+\omega(a',a,c',c))^2}$ term). The van der Waals interaction reaches a maximum when aggregating particles are of about equal size (Figure 2.2b). For particles at a large distance from each other the nature of dependence of van der Waals potential is similar but as shown in the magnified part in the inset plot, the maximum difference between the maximum and minimum potential is about 0.02% of the interaction potential between particles of equal size at the closest.

Therefore the van der Waals interaction is also strongest at a very close distance between equal sized particles, similar to the electrostatic interaction.

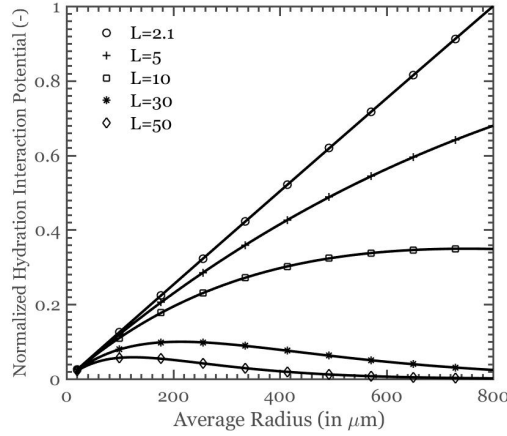
2.2.2.3 Effect of process parameters on hydration interaction

The hydration interaction potential depends on the size ratio (i.e., radius ratio), the size (i.e., the average radius), the separation between particles (i.e., the normalized distance) and the decay length (Equation 2.12). Since most of the previous work on colloidal aggregation involves aggregation of similar or dissimilar nanoparticles with each other, the experimentally estimated values of the decay length are in the range of $0.2 - 1.5 \text{ nm}$ (Israelachvili and McGuiggan, 1988). In this system, since the average radius of the hetero-aggregates of microparticles and nanoparticles is significantly higher than the decay length for nanoparticle aggregation, the hydration force is negligible compared to other forces. Therefore, we examined the effect of parameters mentioned above on the hydration force assuming the decay length to be 6 nm . For the simulation of heteroaggregation process, the decay length was kept constant at 0.6 nm .

It can be seen that the hydration interaction potential decreases exponentially



(a) Effect of distance between particles for different size ratio (b) Effect of size ratio of two particles for different distances



(c) Effect of average size of particles for different normal distances

Figure 2.3: Effect of different parameters on hydration interaction potential

with distance for different radius ratio due to the inverse-exponential dependence on distance ($\exp(-\frac{a(a',a',c',c)}{\delta_0}(L(l)-2))$ in Equation 2.12) and is non-existent at a normalized distance greater than 80 (Figure 2.3a). It is also important to note, positive hydration interaction potential indicates that the hydration interaction inhibits aggregation which is in accordance with the nature of the hydration interaction. Similar to electrostatic and van der Waals interaction, hydration interaction potential is maximum for equal sized particles and decrease with increasing size disparity. The difference between the hydration interaction potential

between particles with more dissimilar sizes is higher at a smaller distance. As the distance between particles increase the difference decreases.

In Figure 2.3b the hydration force shows a similar trend to the van der Waals and electrostatic interaction in its relationship with size ratio of particles owing to a similar dependence on radius ratio as both electrostatic and van der Waals interaction potential ($\frac{\omega(a',a,c',c)}{(1+\omega(a',a,c',c))^2}$ term in Equation 2.12). The hydration force reaches a maximum when particles are of equal size and decrease with increasing size disparity. This behavior is more pronounced for particles closer to each other. At a normalized distance of 50, it can be seen that the maximum potential is only 4% of the maximum potential between particles at a distance of 2.1.

The hydration interaction potential unlike electrostatic interaction potential increases linearly with increasing particle size for particles that are closer to each other because more water molecules are attached to the surface of bigger particles removing which takes more energy. This rate of increase with increasing particle size decreases as the distance between the particles increase and finally for particles that are far away (normalized distance, $L = 30$ and 50 in the plot) the potential first increases a little and then decreases with increasing size. This happens due to the counteracting proportional and inverse-exponential dependence on average radius (see Equation 2.12). Depending on the distance between particles one of the aforementioned terms dominates and dictates the magnitude of the hydration interaction potential.

Therefore, the hydration interaction potential is highest for larger equal sized particles at small distances.

2.2.2.4 Effect of process parameters on total interaction potential

Effect of different process parameters on the total interaction potential is discussed in this section. The surface potential of alginate particles is -46 mV and the chitosan particles is 40 mV . However the monoaggregates and the heteroaggregates

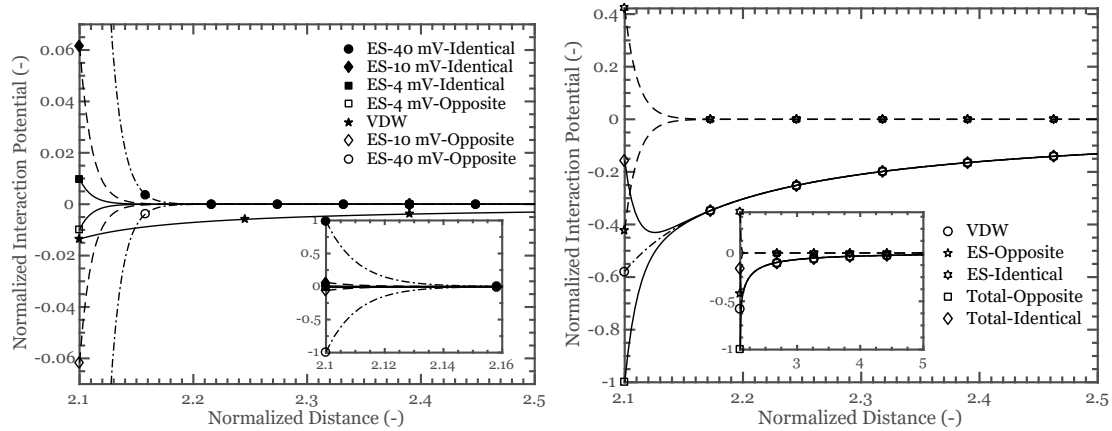
have different surface potential depending on the composition which is the number of chitosan particles attached to the alginate particle in the monoaggregate and similarly for heteroaggregates the number of chitosan particles present for each alginate particle.

In Figure 2.4a, the two most dominant interactions in this system, the van der Waals interaction potential and the electrostatic interaction potential along with the total interaction potential are plotted with the inter-particle distance for particles with different surface potential. At small distances the electrostatic potential is very high between particles with more surface charge (that is when, *i*) both particles have surface potential of $+40\text{ mV}$; *ii*) both particles have surface potential of -40 mV ; *iii*) the particles have surface potential of $+40\text{ mV}$ and -40 mV) compared to the electrostatic potential between particles with less surface charge (that is when, *i*) both particles have surface potential of $+10\text{ mV}$; *ii*) both particles have surface potential of -10 mV ; *iii*) the particles have surface potential of $+10\text{ mV}$ and -10 mV ; *iv*) both particles have surface potential of $+4\text{ mV}$; *v*) both particles have surface potential of -4 mV ; *vi*) the particles have surface potential of $+4\text{ mV}$ and -4 mV) and van der Waals interaction potential. It can also be seen that the van der Waals potential is comparable to the electrostatic interaction potential between particles with surface potential of a magnitude of 4 mV in this system.

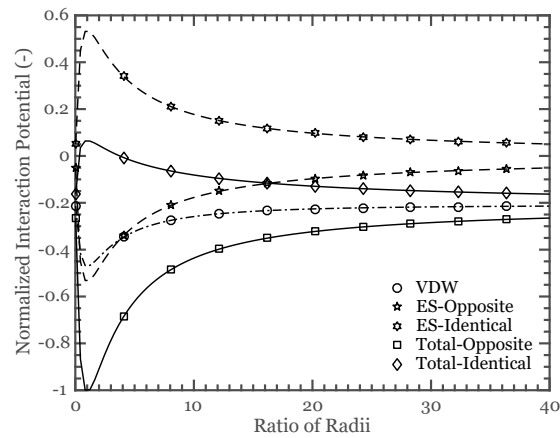
In Figure 2.4b the van der Waals interaction potential, the electrostatic interaction potential for particles with surface potential of 4 mV with opposite and identical charges and the total interaction potential for both these cases are plotted. For oppositely charged particles both the van der Waals and electrostatic forces are attractive and thus the magnitude of the total interaction potential is highest and decreases rapidly at close distance between particles but at a normal distance larger than 2.15 coincides with the van der Waals potential curve since the electrostatic potential is insignificant at a distance greater than this.

For particles with identical charge, the repulsive electrostatic force acts against the attractive van der Waals force and the magnitude of the total interaction potential is about 16% of the total interaction potential between particles with identical charges when the particles are at a normal distance of 2.1. As the distance between particles increases the magnitude of the repulsive electrostatic force decreases more rapidly than the van der Waals force and the total interaction potential reaches the highest magnitude at a normal distance of about 2.12 and then coincides with the van der Waals potential curve at distance greater than 2.15 similar to the total interaction potential potential curve for identically charged particles.

In Figure 2.4c, the van der Waals interaction potential, the electrostatic interaction potential for particles with surface potential of 4 mV with opposite and identical charges and the total interaction potential for both these cases are plotted with the radius ratio of the particles. It was seen that the interaction potentials are highest for equal sized particles. It is important to note that the magnitude of the electrostatic interaction potential decreases more rapidly than the van der Waals interaction potential, with increasing size disparity. As expected, when the particle size disparity is low the total interaction potential is dominated by the electrostatic interaction and as size disparity increases the effect of van der Waals interaction becomes more prominent. Similar to Figure 2.4b, the highest total interaction potential happens when the particles are of opposite charge since both the electrostatic and van der Waals interactions are attractive.



(a) Effect of inter-particle distance for different surface potential (b) Effect of inter-particle distance for surface potential magnitude of 4 mV



(c) Effect of particle radius ratio for surface potential magnitude of 4 mV

Figure 2.4: Effect of (a)-(b) inter-particle distance and (c) particle radius ratio on van der Waals, electrostatic and total interaction potential

ES: electrostatic interaction potential; **VDW:** van der Waals interaction potential; **Total:** total interaction potential.

Identical: both particles have either positive or negative surface potential of denoted magnitude; *Opposite:* particles have opposite surface potential of denoted magnitude

2.2.2.5 Effect of relative alginate & chitosan concentration on final heteroaggregate size distribution

As shown before, the dominant force resulting in aggregation of particles and formation of firstly; monoaggregates (chitosan nanoparticle layered on alginate micro-particle) and then; heteroaggregates (multiple alginate and chitosan particles agglomerated together) is the electrostatic force, especially at a very close distance. A previous experimental study on alginate-chitosan system (Deshpande (2014)) has shown that the final aggregate demographics depend on the relative amount of alginate and chitosan. Systems with nanoparticles also show similar behavior by reaching different aggregation regimes depending on the properties of the system (Atmuri et al., 2013). Therefore, the effect of relative alginate and chitosan concentration on final heteroaggregate size distribution was studied.

Since the first stage of heteroaggregation process is the formation of monoaggregates from monodispersed alginate and chitosan particles and this model focuses only on the heteroaggregation of these monoaggregates which happens afterwards, different standard distributions were used for the initial monoaggregate distributions for different starting alginate and chitosan ratio.

Based on the amount of initial alginate and chitosan, in each case, different number of monoaggregates were assumed to have different charges. For example, a very small amount of chitosan would result in a initial distribution of monoaggregates with partially negative charge due to the absence of sufficient chitosan particles necessary to neutralize the negative charge of the alginate particles. In contrast, very high amount of chitosan would result in a initial distribution of monoaggregates where the number of positively charged monoaggregates is higher due to the presence of chitosan particles in excess of that necessary to neutralize the negative charge of the alginate particles. In the intermediate region where the chitosan amount is neither too low nor too high and close to the amount necessary to neutralize the charge of alginate, the number of monoaggregates with

neutral or close to neutral charge is higher compared to monoaggregates with strong negative or positive charge.

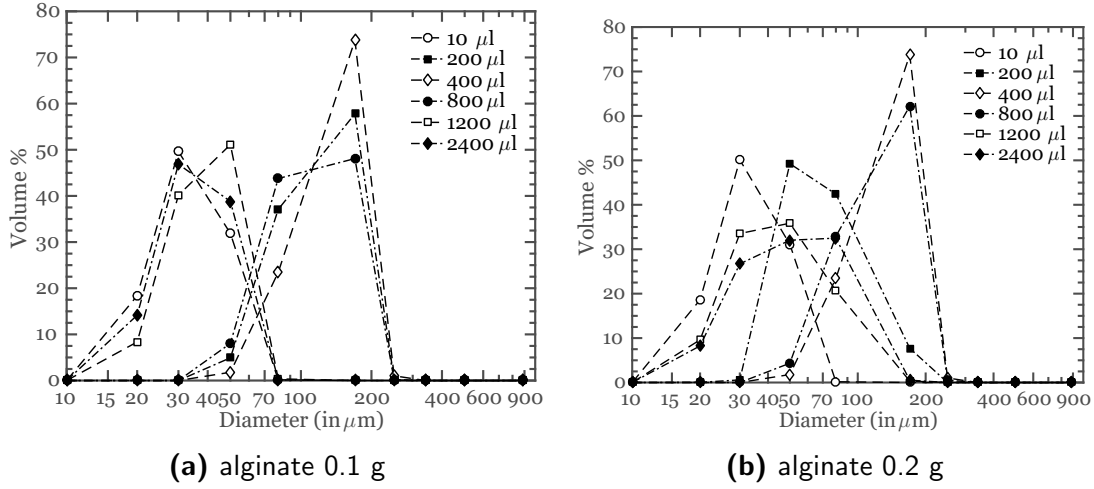


Figure 2.5: Model estimated variation of final heteroaggregate particle size distribution for different chitosan and alginate amount. *Corresponding chitosan volume fraction of the samples: 0.004 (0.1 g alginate-10 μ l chitosan), 0.077 (0.1-200), 0.144 (0.1-400), 0.251 (0.1-800), 0.335 (0.1-1200), 0.502 (0.1-2400), 0.002 (0.2-10), 0.0.04 (0.2-200), 0.077 (0.2-400), 0.144 (0.2-800), 0.201 (0.2-1200), 0.335 (0.2-2400)*

In Figure 2.5a, the effect of initial chitosan concentration on the final heteroaggregate particle size distribution (PSD) is shown for a fixed alginate amount of 0.1 g. For 10 μ l of chitosan, the initial monoaggregate distribution consists mostly of negatively charged monoaggregates and the repulsive electrostatic force is higher than the attractive van der Waals which results in a final distribution where heteroaggregate formation is very low. As the chitosan volume is increased to 200 μ l, the initial monoaggregate distribution comprises of more neutrally charged monoaggregates or monoaggregates with a weak negative charge so heteroaggregate formation increases as the electrostatic repulsion between these monoaggregates are weaker than the previous case resulting in formation of bigger particles. For an even higher amount of chitosan of 400 μ l, the number of neutrally charged monoaggregates is higher and that leads to formation of bigger and a higher number of heteroaggregates. When the chitosan amount is increased even more to 800 μ l, initially some of the neutral monoaggregates present in the

case of 400 μl become positively charged and the formation of heteroaggregate is lower than that for 400 μl . As the chitosan amount is increased even more to 1200 μl and 2400 μl , more monoaggregates become positively charged and that prevents the formation of big heteroaggregates.

In Figure 2.5b the final particle size distribution is shown for 0.2 g of alginate. For this alginate amount as well the same trend follows. For 10 μl of chitosan, most of the monoaggregates initially are negatively charged since there is not enough chitosan particles to neutralize the negative charge of the alginate particles and as a result there is low heteroaggregate formation. For 200 μl of chitosan, there are more neutral or close to neutral monoaggregate initially which leads to the formation of more heteroaggregates. For 400 μl of chitosan, there are more neutrally charged monoaggregates initially which leads to the formation of more and even bigger heteroaggregates similar to the case for 0.1 g alginate. Since there are more alginate particles for 0.2 g of alginate than that for 0.1 g, even for 800 μl chitosan, the number of neutral monoaggregates is also very high and this leads to the formation of a high number of heteroaggregates similar to the case with 400 μl of chitosan. For 1200 μl and 2400 μl of chitosan though, similar to the 0.1 g alginate case, the number of positively charged monoaggregate initially is higher which hinders the formation of big and as many heteroaggregates.

The effect of relative alginate and chitosan concentration on average diameter of the particles in the system namely D_{10} , the 10th percentile mass diameter, D_{50} , mass median diameter and D_{90} , the 90th percentile mass diameter is plotted in Figure 2.6. As chitosan amount increases for both 0.1 g and 0.2 g alginate, the particles get bigger initially resulting in an increase in D_{10} , D_{50} and D_{90} . This indicates the transition from ‘dispersed, uncoated’ regime to ‘agglomerated’ regime. For, 0.1 g alginate, at 200 μl , 400 μl and 800 μl of chitosan the D_{10} , D_{50} and D_{90} are considerably higher than the other chitosan amounts indicating the occurrence of the ‘agglomerated’ regime. For 0.2 g alginate, the ‘agglomerated’

regime can be seen for 400 μl and 800 μl of chitosan. With even higher chitosan amounts the average diameter decreases as the ‘agglomerated’ regime transitions to ‘dispersed, coated’ regime and the particle size decreases.

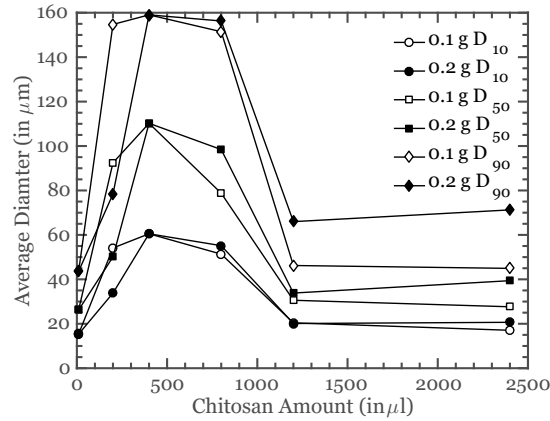


Figure 2.6: Model estimated variation of D_{10} , D_{50} and D_{90} with chitosan amount for 0.1 g and 0.2 g of alginate

2.2.2.6 Effect of relative alginate & chitosan concentration on final heteroaggregate composition

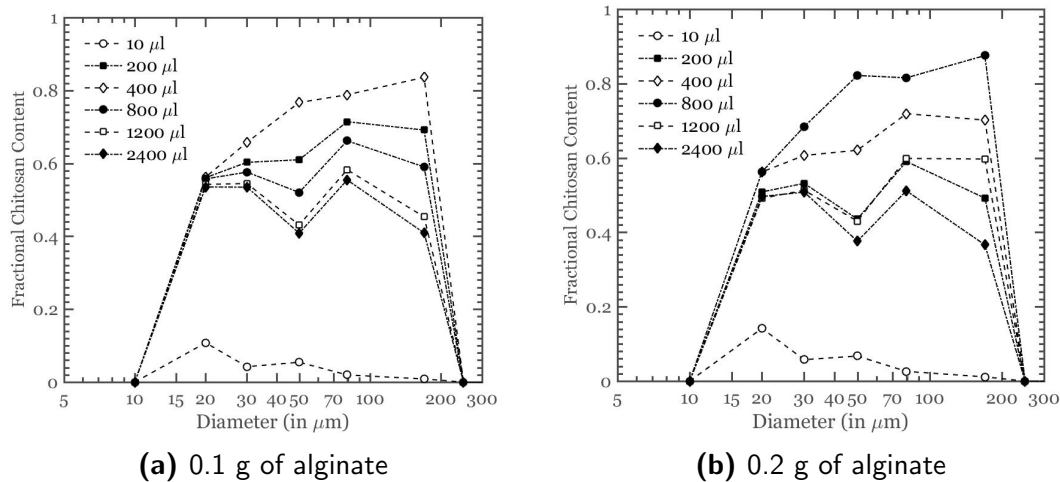


Figure 2.7: Variation of final fractional chitosan content for different amount of chitosan and alginate

The model evaluated number averaged fractional chitosan content for 0.1 g and 0.2 g alginate is shown in Figure 2.7a and 2.7b respectively. The same

amounts of alginate and chitosan as used to study the effect of alginate and chitosan concentration on the final aggregate size were used here.

In both the cases as expected, the fractional chitosan content is very low for 10 μl of chitosan since there is a very low amount of chitosan compared to alginate in the system. In Figure 2.7a as the chitosan amount increases to 200 μl the fractional chitosan content increases since the number of heteroaggregates which have more chitosan than smaller particles increases. For 400 μl as the number of heteroaggregates increases even more the fractional chitosan content also increases. Above that, with increasing chitosan amount the fractional chitosan content decreases as the number of heteroaggregates decreases. It is crucial to note that with increasing chitosan amount, the fractional chitosan content does not increase above 400 μl because the excess chitosan is in free chitosan form which is not accounted for by the model, the fractional chitosan content in the monoaggregates and heteroaggregates in the system is shown in Figure 2.7a.

In Figure 2.7b the same trend is observed. In accordance with Figure 2.8b and 2.5b, the highest fractional chitosan content is observed for 800 μl since with 0.2 g alginate the most heteroaggregation formation happens in this case. With lower and higher amounts of chitosan than this, the number averaged fractional chitosan content is lower because similar to the 0.1 g alginate case, the heteroaggregate formation is also lower in these cases.

2.3 Experimental investigation of heteroaggregate particle size distribution

2.3.1 Experimental procedure

2.3.1.1 Materials & instruments

Low molecular weight (50-190 kDa) chitosan (deacetylation fraction 90.85 %, viscosity of 185 cP for a concentration of 1% w/w in 1% w/w acetic acid solution), 85% sodium tripolyphosphate (TPP), dibromohexane (96%) and span-80 was supplied by Sigma Aldrich. Sodium alginate (molecular weight of 450-550 kDa, viscosity of 485 cP (for a 1% w/w solution)) which consisted of 65-75% guluronic acid (G) subunits and 25-35% mannuronic acid (M) subunits was supplied by Acros Organics under the name alginic acid. HPLC grade iso-octane and calcium chloride was supplied by Fisher Scientific. Water was acquired from a Milli-Q water system.

A Beckman Coulter LS 13 320 laser diffraction spectroscope was used for measurement of the particle size distribution of alginate microparticles and the heteroaggregates. Zeta potential and chitosan nanoparticle average diameter was measured using a Malvern Zetasizer. A Beckman centrifuge was used for centrifuging the alginate suspension in order to separate and collect alginate beads.

2.3.1.2 Chitosan nanoparticle preparation

chitosan was cross-linked using sodium tripolyphosphate by the ionic gelation method used by (Yu et al., 2013). 0.7 ml TPP solution of 2 mg/ml concentration was added to 5 ml of 2 mg/ml chitosan solution. Produced chitosan particles (average diameter of 250 nm, approximate zeta potential of 40 mV, density of 1 g/ml) were suspended in water to produce a chitosan suspension of concentration 37.5 mg/ml.

2.3.1.3 Alginate microparticle preparation

Sodium alginate solution was prepared and emulsified in 1,6-dibromohexane and iso-octane, and span-80 was used as surfactant. The emulsified alginate was cross linked using calcium chloride to form calcium alginate gel micro-beads. Then the separation of the emulsion was performed in a separatory funnel with acetone washing. Extracted alginate solution was centrifuged followed by the removal of the supernatant liquid and collection of the alginate beads. Afterwards, wet sieving of the alginate particles was performed and the particles were stored in DI water (Yu et al., 2013). The resulting micro-beads (density of 1.05 g/ml) had a diameter of 25-38 μm with an average diameter of 34 μm and a zeta potential of about -46 mV (Mladenovska et al., 2007).

2.3.1.4 Heteroaggregation experiments

Two different sets of experiments were performed where the alginate amount was varied at 0.1 g (approximately 4.63×10^6 particles and 95.24 μl volume) and 0.2 g (approximately 9.26×10^6 particles and 190.48 μl volume) and for each alginate level the chitosan solution amount was varied in 6 levels: 10 μl (roughly 4.89×10^{10} particles and 0.4 μl of particle volume), 200 μl (roughly 9.78×10^{11} particles and 8 μl of particle volume), 400 μl (roughly 1.96×10^{12} particles and 16 μl of particle volume), 800 μl (roughly 3.91×10^{12} particles and 32 μl of particle volume), 1200 μl (roughly 5.87×10^{12} particles and 48 μl of particle volume) and 2400 μl (roughly 1.17×10^{13} particles and 96 μl of particle volume). The total volume of the sample was kept constant at 10 ml. Each of these experiments was performed three times. To prepare these samples, first, water according to the chitosan amount was taken and then desired amount of alginate (by weight) was added into the water. Then the desired amount of chitosan was added. Finally, the mixture was sonicated to break down any initial monoaggregates and/or heteroaggregates that were formed.

All the samples from both the sets were analyzed with a Beckman Coulter LS 13 320 laser diffraction spectrometer. Fraunhofer.rf780d was selected as the optical model with the refractive index of the medium set at 1.33 (refractive index of water). The difference between mean and standard deviation of all three trials of each sample distributions were below 10%.

2.3.2 Results & discussion

Heteroaggregation experiments and LDS analyses as mentioned in Section 2.3.1.4 were performed to study the effect of relative starting concentration of alginate and chitosan on the final heteroaggregate PSD and compare it to the model calculated values. The PSDs for 0.1 g and 0.2 g alginate was plotted in Figures 2.8a and 2.8b respectively. The similarity between Figure 2.5a-Figure 2.8a and Figure 2.5b-Figure 2.8b shows that the model can correctly capture the system behavior.

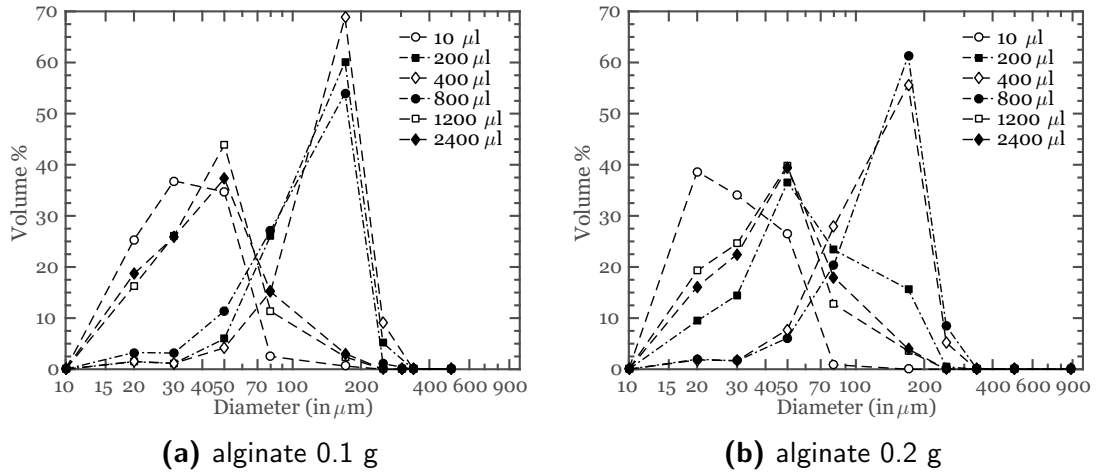


Figure 2.8: Experimentally observed variation of final heteroaggregate particle size distribution for different chitosan and alginate amount. *Corresponding chitosan volume fraction of the samples: 0.004 (0.1 g alginate-10 μl chitosan), 0.077 (0.1-200), 0.144 (0.1-400), 0.251 (0.1-800), 0.335 (0.1-1200), 0.502 (0.1-2400), 0.002 (0.2-10), 0.004 (0.2-200), 0.077 (0.2-400), 0.144 (0.2-800), 0.201 (0.2-1200), 0.335 (0.2-2400)*

For 0.1 g alginate, in Figure 2.8a, at 10 μl chitosan, most of the particles have

a diameter of about $30\ \mu m$ which is similar to the diameter of a single alginate particle (average diameter $34\ \mu m$). This indicates the presence of ‘dispersed, uncoated’ regime, since in this regime, the majority of particles in the system are monoaggregates (which are single alginate particles with a chitosan layer on them). For 1200 and 2400 μl chitosan, most of the particles have a diameter of around $50\ \mu m$, which points toward the existence of ‘dispersed, coated’ regime. The particles are slightly bigger in the ‘dispersed, coated’ regime than the ‘dispersed, uncoated’ regime because the thickness of chitosan layer should be higher in case of the earlier. For 200, 400 and 800 μl chitosan, most particles have a diameter of around $200\ \mu m$, indicating the presence of big heteroaggregates in the ‘agglomerated’ regime.

For 0.2 g alginate (Figure 2.8b), since the number of alginate particles are more than for 0.1 g alginate, in case of 10 μl chitosan, the thickness of chitosan layer is less than that in case of 0.1 g alginate. For this reason, there are some monoaggregates in case of 0.2 g alginate which are smaller than the monoaggregates for 0.1 g alginate (Figure 2.8a) in the ‘dispersed, uncoated’ regime. For 0.2 g alginate-200 μl chitosan, the system is in transition from ‘dispersed, uncoated’ regime to the ‘agglomerated’ regime, unlike 0.1 g alginate-200 μl chitosan where the system is in ‘agglomerated’ regime, since the amount of chitosan is not enough to neutralize the higher amount of alginate present in the case of the earlier. For 400 and 800 μl chitosan, there is enough chitosan in the system to neutralize 0.2 g alginate, resulting in the formation of mostly neutral monoaggregates and as result finally in the formation of big heteroaggregates leading to the ‘agglomerated’ regime, similar to 0.1 g alginate. For 1200 and 2400 μl chitosan, the system again transitions to the ‘dispersed, coated’ regime, for reasons similar to the case of 0.1 g alginate.

In Figure 2.9, the experimental D_{10} , D_{50} and D_{90} were plotted with increasing chitosan amount for both 0.1 g and 0.2 g of alginate. A similar trend to the one

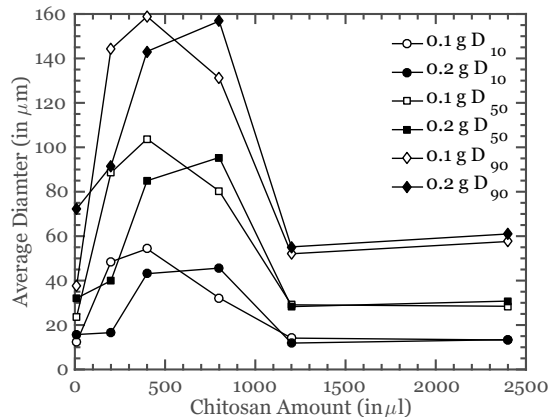


Figure 2.9: Experimentally observed variation of D_{10} , D_{50} and D_{90} with chitosan amount for 0.1 g and 0.2 g of alginate

seen in Figure 2.6 is observed. At 10 μl chitosan, for both 0.1 g and 0.2 alginate, the system is in ‘dispersed, uncoated’ regime and the D_{10} , D_{50} and D_{90} are low. As the chitosan amount increases the transition to ‘agglomerated’ regime starts and the system is in ‘agglomerated’ regime at 200, 400 and 800 μl chitosan for 0.1 g alginate where the D_{10} , D_{50} and D_{90} are very high. For 0.2 g alginate, at 200 μl chitosan, the system is in between ‘dispersed, uncoated’ and ‘agglomerated’ regime, and is in ‘agglomerated’ regime at 400 and 800 μl chitosan. With even higher chitosan amount, D_{10} , D_{50} and D_{90} start to decrease as the transition to ‘dispersed, coated’ regime from the ‘agglomerated’ regime starts and the system is in ‘dispersed, coated’ regime at 1200 and 2400 μl chitosan. The sum of squared error (SSE) was also calculated for the PBM calculated D_{10} , D_{50} , D_{90} based on the corresponding experimental values. The average SSE for 0.1 g alginate was 0.0481 and for 0.2 g alginate, it was found to be 0.1455.

2.4 Chapter conclusions

A population balance model for agglomeration stage of the heteroaggregation process was developed. The model was able to simulate the real system fairly accurately. The effect of various process parameters on the individual interaction

potentials such as van der Waals, electrostatic and hydration forces and the total interaction potential which is the sum of the above, was also examined. It was found that the electrostatic force is strongest between two small, equal sized particles with high surface potential ratio (i.e. distinct surface charge) at close distance. The van der Waals and hydration forces are strongest between equal sized particles when they are closest to each other. It was also seen that the electrostatic force followed by the van der Waals force played the most significant role and hydration force was negligible and as a result the total interaction potential behaved similarly to the combined effect of electrostatic and van der Waals interactions.

The effect of initial alginate and chitosan concentration on the final particle size distribution was studied both through the model and the experiments. Depending on the initial relative concentration of alginate and chitosan, the system demonstrated the presence of three different regimes as described in Chapter 1. For a very small amount of chitosan the system progressed towards the ‘dispersed, uncoated’ regime consisting mainly of alginate particles partially coated with chitosan particles. With very high amount of chitosan the system advanced towards the ‘dispersed, coated’ regime comprised of alginate particles ‘over-coated’ with chitosan particles and for intermediate chitosan loading, the neutral or close to neutrally charged monoaggregates agglomerated with each other to form bigger heteroaggregates and resulted in the ‘agglomerated’ regime.

The effect of initial relative concentration of alginate and chitosan on the final heteroaggregation composition was also investigated using the model. The results corroborated the nature of final heteroaggregate PSD. The agglomerated regime had heteroaggregates with more chitosan compared to the partially coated monoaggregates in the uncoated dispersed regime and the over-coated monoaggregates in the coated dispersed regime since the larger fraction of chitosan present as free chitosan particles in the last two cases was not taken into account by the

model.

This work explored the effect of different process parameters in detail which gives an initial understanding of the ranges these parameters should be varied within to form aggregates of specific size. A qualitative relation between relative quantity of alginate-chitosan and final heteroaggregate size and the final heteroaggregate composition was established. This knowledge can further be used to determine the initial conditions of the system to form heteroaggregates of required size and composition. Depending on the application heteroaggregates of different size and composition would be more efficient, so ultimately this knowledge can be used to produce heteroaggregates tailored for different applications.

The next step would be to model the first stage of the heteroaggregation process, which is the formation of chitosan layers on the alginate particles for formation of monoaggregates. This can be modeled as a layering process with the layering rate dependent on the relative size and surface charge of individual alginate and chitosan particles.

Chapter 3

Development and experimental validation of a model for the layering stage of the heteroaggregation process

3.1 Background & objectives

In order to understand heteroaggregation, it is important to understand the process of formation of monoaggregates by layering of chitosan nanoparticles onto the surface of the alginate microparticles. A better understanding of the layering process and factors that control and limit it is necessary. In previous research, the layering of smaller particles on a bigger particle of a different kind has not been explored in detail. Fundamental questions such as what limits the layering, the surface coverage or the the charge neutralization for charged particles, remain unanswered. Furthermore, it is not clear whether for charged particles the complete charge neutralization prevents further layering or in a system such as the one studied in this work, the layering stops when the surface potential of a monoaggregate is equal to the surface potential of the chitosan particles. In the latter case, the repulsion between a monoaggregate and a chitosan particle becomes larger than the repulsion between two chitosan particles. Another important thing is to be able to calculate the surface charge or surface potential of the monoaggregates. It is crucial to know whether the monoaggregate surface charge potential originates from the presence of just the chitosan layer on the surface and the free positive sites or do the negative sites of the alginate also play a role in this. This gives rise to another important question, which is whether the chitosan

layer is a uniform layer covering the entire surface of the alginate particle or can they form a 2-dimensional structure with some free alginate surface area. It is therefore necessary to model the layering stage of the heteroaggregation process to find the answers to these questions.

There has been some previous research on simulating heteroaggregation systems using molecular dynamics simulations. Cerbelaud et al. (2008) simulated heteroaggregation between alumina particles (400 nm) and silica particles (25 nm) using Brownian dynamics to look at the amount of silica adsorbed on alumina particles with increasing silica-to-alumina ratio. They also studied the same using inductively coupled plasma (ICP) analysis. It was observed by the authors that the maximum amount of silica that can be adsorbed on the alumina surface is much smaller than the close-packing coverage. They also studied the heteroaggregate structure using cryo-field emission gun scanning electron microscope (cryo-FEGSEM). The heteroaggregates were seen to have a open branch-like structure. Cerbelaud et al. (2009) performed more detailed simulations on the same system and showed that the silica particles form a pseudo-hexagonal network as opposed to a random arrangement on the alumina surface as the silica amount in the solution is increased. They also attributed the chain-like structure of the heteroaggregates to the energy barrier that monoaggregates have to cross to rearrange the silica particles on the surface to form more compact heteroaggregate structure, even though the compact structures are energetically more favorable. In Cerbelaud et al. (2010), they performed these simulations for 10 seconds and compared the heteroaggregate structure with cryo-FEGSEM images of the heteroaggregates. Although, these articles provided insights into heteroaggregation processes, these were based on systems with particles that are significantly less size asymmetric compared to the alginate-chitosan system studied in this work.

There is also some previous work on modeling colloidal systems using DEM. Hong (1997) performed a DEM simulation incorporating body forces such as

van der Waals, electrostatic forces, adhesion forces, influence of the medium and body contact forces to simulate particle packing in colloidal foaming processes. He found that the electrostatic force dominated the particle motion. He also observed that in highly concentrated solutions, particles with electrostatic repulsion formed chain-like structures but particles without repulsion tended to form compact agglomerates. In a later work, he further improved the model by implementing the adhesive force based on the Johnson-Kendall-Roberts (JKR) theory instead of the long-range DLVO forces to fix the problem of numerical singularity which arises from the van der Waals force approaching infinity as the distance between particle surface approaches zero (Hong, 1998). At a particle distance less than that at which JKR adhesion force is equal to van der Waals force, the adhesion forces was used to model particle movement. Li et al. (2006) also used DEM to simulate packing structure of mono-sized silicon dioxide particles.

These models had considerable success in simulating the heteroaggregation of colloidal particles, however, with increasing size difference between the particles, the development of such a modeling framework becomes increasingly difficult. The numerical stability of such simulation methods require the largest possible time step to be defined by the size of the smallest particle in the system. This results in the simulation progressing in the time direction slowly. At the same time, the presence of larger particles requires the simulation domain to be large, thereby, also increasing the computational load. Both these reasons make the simulation of a system with such large size difference very complex. Therefore, it is necessary to have a mesoscale modeling framework where the time step is not dependent on the size of the particles and the particles can be treated in groups rather than individually. For this purpose a separate 1-dimensional population balance framework was designed to simulate the layering stage of the heteroaggregation process where the nanoparticles layer on the microparticles.

It is vital to compare the findings from the model with experimental observations of aggregate structures. In some previous studies, researcher have used various imaging techniques to study the structure of monoaggregates and heteroaggregates. Fisher et al. (2001) studied the fraction of silica particles (5-300 nm) adsorbed onto the surface of alumina particles (250 nm). They found that the fraction of silica adsorbed on the surface of alumina varied with the silica particle size. The structure of the silica layer on the alumina particle was also studied using a scanning electron microscope (SEM). It was observed that the silica formed a monolayer on the surface of the alumina particle. Johnson and Lenhoff (1996) used atomic force microscopy (AFM) to study the adsorption of charged latex particles on to a mica base at various ionic strengths. For low ionic strength of 0.003 mM and 0.1 mM, the latex particles were seen to be uniformly distributed and evenly spaced on the mica surface. At higher ionic strength, however, the latex particles were assembled into two dimensional clusters on the surface of the mica substrate. Kim and Berg (2000); Kim et al. (2003) studied the structure of large heteroaggregates formed from negatively charged silica and positively charged alumina-coated silica particles. They observed that the heteroaggregates had a branched structure. Rasa et al. (2004) also were able to experimentally image the heteroaggregates of negatively charged silica and positively charged alumina coated silica particles using a cryo-SEM. Yates et al. (2005) investigated the heteroaggregation of alumina (310 nm) and silica particles (4.3-285 nm) experimentally. They discovered that the number of silica particles needed for optimum heteroaggregation decreased with increasing silica particle size. Also at a very high size asymmetry, the number of silica particles exceeded the calculated half surface coverage number while at a very low size asymmetry, the number of silica particles needed for optimum heteroaggregation was about 25% of the half surface coverage number. In this work, SEM images of the heteroaggregates was acquired to study the layering of nanoparticles on the

microparticles.

Once the layering model is developed, it is important to integrate the findings from that into the model for the agglomeration stage. This integrated model can then generate the final heteroaggregate PSD which can then be compared to the experimentally acquired PSD, thereby validating the model for the layering stage.

Objectives

The objectives of the work presented in this chapter are as follows.

- **Sub aim 1:** Development of a model to simulate the layering stage of the heteroaggregation process to study the extent of layering on monoaggregates
- **Sub aim 2:** Experimental study of chitosan layer on alginate beads
- **Sub aim 3:** Integration of the model for the layering stage with the model for the agglomeration stage to develop a model for the entire heteroaggregation process

3.2 Development of a model for the layering stage of the heteroaggregation process

3.2.1 Mathematical model development

A layering model was developed to simulate the layering of chitosan nanoparticles on the alginate microparticles due to the combined effect of van der Waals, electrostatic and hydration forces. Even though all three forces are combined the electrostatic force is by far the most dominant, especially for the layering stage, since the nanoparticles and the microparticles are oppositely charged, resulting in a strong attractive electrostatic force.

In this model, the monoaggregates are divided in different classes based on the amount of chitosan layered on them. The number of monoaggregates with a volume of chitosan defined by c at time t is defined as $N(c,t)$. Depending the rate of layering, the number of monoaggregates with a certain amount of chitosan changes with time. As the layering stage progresses, more chitosan particles gets attached to the alginate particle in the monoaggregate and the number of monoaggregates with less chitosan decreases and more chitosan increases as the monoaggregates move from one particle class to another. This rate of change of number of monoaggregates is calculated as follows:

$$\frac{\partial}{\partial t}N(c,t) = R_{layering}(c) \quad (3.1)$$

where, $R_{layering}(c)$ is the rate of layering on monoaggregates with chitosan volume c and can be expressed as:

$$R_{layering}(1) = -N(1)\frac{K_{layering}(1)}{(v_c(2) - v_c(1))} \quad (3.2)$$

$$R_{layering}(nc) = N(nc-1)\frac{K_{layering}(nc-1)}{(v_c(nc) - v_c(nc-1))} \quad (3.3)$$

$$\begin{aligned} R_{layering}(2 : nc-1) = & N(1 : nc-2)\frac{K_{layering}(1 : nc-2)}{(v_c(2 : nc-1) - v_c(1 : nc-2))} \\ & - N(a, 2 : nc-1)\frac{K_{layering}(2 : nc-1)}{(v_c(3 : nc) - v_c(2 : nc-1))} \end{aligned} \quad (3.4)$$

where, $K_{layering}(c)$ is the layering kernel for a monoaggregate with chitosan volume represented by c , $v_c(c)$ is the volume of chitosan in a monoaggregate and $v_c(nc)$ is the highest volume of chitosan that any monoaggregate in the system can have.

The layering kernel, $K_{layering}$ is calculated similarly to the aggregation kernel as shown in Chapter 2, the only difference being that the layering happens between one alginate particle and free chitosan in the system as opposed to two monoaggregates as is the case in the second stage of heteroaggregation.

The layering kernel is formulated as (Axford, 1997):

$$K_{layering}(c) = \frac{K_B}{W(c)} \frac{(R_{alginate}^{-1} + R_{chitosan}^{-1})(R_{alginate} + R_{chitosan})}{4} \quad (3.5)$$

where, $K_B = 8kT/3\mu$ is the collision rate constant between a monoaggregate and the individual chitosan particles due to Brownian motion. $R_{alginate}$ and $R_{chitosan}$ are respectively the radii of an alginate and a chitosan particle. It is assumed that the radius change in a monoaggregate due to layering of chitosan is negligible and therefore the monoaggregate radius is assumed to be equal to the radius of an alginate particle. W is the Fuchs stability constant.

The Fuchs stability constant is calculated from the hydrodynamic resistance, $G(c, l)$ experienced by the approaching monoaggregate and chitosan particles due to the dispersion of fluid between them, the total interaction potential between a monoaggregate and individual monodispersed chitosan particles; U , the thermal energy of the system; kT and the dimensionless center-to-center distance $L(l)$ ($= r(l)/A$), where r is the actual distance between the center of the monoaggregate and an individual chitosan particle. A is the average radius of the monoaggregate and a chitosan particle. As mentioned before, the radius of the monoaggregate is assumed to be equal to that of an alginate particle. So, the average radius becomes, $A = (R_{alginate} + R_{chitosan})/2$). The hydrodynamic resistance was neglected in this work. The expression relating the Fuchs stability constant to the above mentioned parameters is shown below.

$$W(c) = 2 \int_2^\infty \frac{\exp(U(c, l)/kT)}{G(c, l)L(l)^2} dL \quad (3.6)$$

The total interaction potential is the sum of the van der Waals, electrostatic and hydration interaction potential:

$$U = U_{van \text{ der Waals}} + U_{electrostatic} + U_{hydration} \quad (3.7)$$

where, $U_{van \text{ der Waals}}$, $U_{electrostatic}$ and $U_{hydration}$ are respectively the van der Waals, electrostatic and hydration interaction potential.

The van der Waals interaction potential is calculated as (Elimelech et al.,

1995):

$$U_{van\ der\ Waals}(c, l) = -\frac{A_H}{6} \times \left[\frac{8\omega(c)}{(1 + \omega(c))^2} \left[\frac{1}{(L(l)^2 - 4)} + \frac{1}{L(l)^2 - 4\left(\frac{1-\omega(c)}{1+\omega(c)}\right)^2} \right] + \ln \left[\frac{L(l)^2 - 4}{L(l)^2 - 4\left(\frac{1-\omega(c)}{1+\omega(c)}\right)^2} \right] \right] \quad (3.8)$$

where, A_H is the Hamaker constant. $\omega(c)$ is the ratio of radii of the monoaggregate and a chitosan particle and calculated as $\omega(c) (= R_{alginate}/R_{chitosan})$, since the monoaggregate radius is assumed to be equal to the radius of an alginate particle. $L(l)$ is the dimensionless center-to-center distance.

The electrostatic interaction potential is calculated as (Sader et al., 1995):

$$U_{electrostatic}(c, l) = \frac{4\pi\epsilon_0\epsilon_r\omega(c)A(c)\psi_{(c)}^2}{(1 + \omega(c))^2L(l)} \times \{(1 + \Psi(c))^2 \ln(1 + \exp[-\kappa A(c)(L(l) - 2)]) + (1 - \Psi(c))^2 \ln(1 - \exp[-\kappa A(c)(L(l) - 2)])\} \quad (3.9)$$

where, $\Psi(c) (= \frac{\psi_{(c)}}{\psi_{chitosan}})$ is the ratio of surface potential of the monoaggregate with layered chitosan volume represented by c to the surface potential of chitosan nanoparticle; $\epsilon_0\epsilon_r$ is the permittivity of the dispersant and $\kappa (= \sqrt{\frac{e^2 N_A \sum_n z_n^2 C_n^b}{\epsilon_0 \epsilon_r k T}})$ is the Debye-Huckel parameter, where, e is the electron charge, N_A is the Avogadro number, z_n and C_n^b are valance and bulk concentration of species (ion) n .

The hydration energy was calculated as shown in Israelachvili (1992):

$$U_{hydration}(c, l) = \frac{4\pi\omega(c)A(c)}{(1 + \omega(c))^2} \times F_0 \delta_0^2 \exp\left(-\frac{A(c)}{\delta_0}(L(l) - 2)\right) \quad (3.10)$$

where, F_0 is the hydration force constant and δ_0 is the decay length.

Numerical method

As discussed in the previous chapter, the numerical stability of a population balance model is largely dependent on the time-step. The upper limit of the

time-step was chosen to ensure that the number of monoaggregates moving from one class to another is not greater than the number of monoaggregates present in the originating class, based on the Courant-Friedrichs-Lewy (CFL) condition described in Ramachandran and Barton (2010). The time-step chosen is provided in Table 3.1. The process time was set as 1 second, since, due to the opposing charges of the aggregating particles (monoaggregates and chitosan nanoparticles) it was assumed that the process will be much faster than the agglomeration process which itself took less than 10 seconds.

All the monoaggregates in the system were assumed to have an alginate volume equal to that of an alginate particle of diameter $34 \mu\text{m}$. Two sets of simulations were performed for total alginate amount of 0.1 g and 0.2 g. The number of alginate particles was calculated from the mass of the alginate added to the system. For the different possible amount of chitosan layered on the monoaggregates (represented by c) a nonlinear grid is used. The highest possible volume of layered chitosan is chosen based on the assumption that the surface potential of a monoaggregate remains constant once it has reached the surface potential of chitosan nanoparticles. After that, with increasing chitosan layering the surface potential stays constant at that value. So to capture the variation of monoaggregate surface potential with increasing chitosan layering, the highest volume or amount of layered chitosan is chosen to be the amount when the monoaggregate surface potential becomes equal to that of chitosan. To make the model more accurate, 30 different size classes were used as shown below.

$$c_i = c_1 \times 1.322^{i-1} \quad (3.11)$$

where, c_1 is the least possible volume of layered chitosan.

The cell average method developed by Kumar et al. (2006) was used similar to Chapter 2 to distribute particles formed in different bins by applying a multidimensional lever rule. All simulations were performed in Mathworks MATLAB®

R2018a on an Intel Core i7-4770 CPU (3.4 GHz) with 12 GB of RAM.

Table 3.1: Parameters for the layering model

Parameter	Symbol	Value	Units
Boltzmann constant	k	$1.3806488 \times 10^{-23}$	$m^2 kg s^{-2} K^{-1}$
Charge of electron	e	$1.60217657 \times 10^{-19}$	<i>Coulombs</i>
Avogadro Number	N_A	6.0221413×10^{23}	—
Hamaker constant	A_H	3×10^{-21}	<i>J</i>
Hydration force constant	F_0	10^{-2}	$N m^{-1}$
Temperature of the medium	T	298	<i>K</i>
Viscosity of the medium	μ	8.999×10^{-4}	<i>Pa.s</i>
Permittivity of the medium	$\epsilon_0 \epsilon_r$	6.93×10^{-10}	$C^2 N^{-1} m^{-2}$
Valence of ions in medium	z	1	—
Bulk concentration of ions in medium	C^b	1×10^{-2}	$kg m^{-3}$
Debye length	$\frac{1}{\kappa}$	1.3581×10^{-7}	<i>m</i>
Decay length	δ_0	6×10^{-10}	<i>m</i>
Density of alginate	$\rho_{alginate}$	1050	$kg m^{-3}$
Density of chitosan	$\rho_{chitosan}$	1000	$kg m^{-3}$
Surface potential of alginate	$\Psi_{alginate}$	-46×10^{-3}	<i>Volts</i>
Surface potential of chitosan	$\Psi_{chitosan}$	56×10^{-3}	<i>Volts</i>
Volume of the system	V	10×10^{-6}	m^3
Radius of alginate particle	$R_{alginate}$	34	μm
Radius of chitosan particle	$R_{chitosan}$	250	<i>nm</i>
Volume of the smallest chitosan bin	c_1	1×10^{-19}	m^3
Simulated process time	t	1	<i>s</i>
Simulation time-Step	dt	0.0001	<i>s</i>

3.2.2 Results & discussion

The increase in surface potential was calculated with increasing surface area coverage of the monoaggregate by chitosan and was plotted in Figure 3.1.

As can be seen, at no surface coverage, that was when, the monoaggregate is a monodispersed alginate particle, the surface potential was equal to that of an individual alginate particle, -46 mV. Here, in this work, surface potential was assumed to be equal to the zeta potential. As the surface coverage increased and as more and more chitosan layered on top of the alginate particle, the surface charge

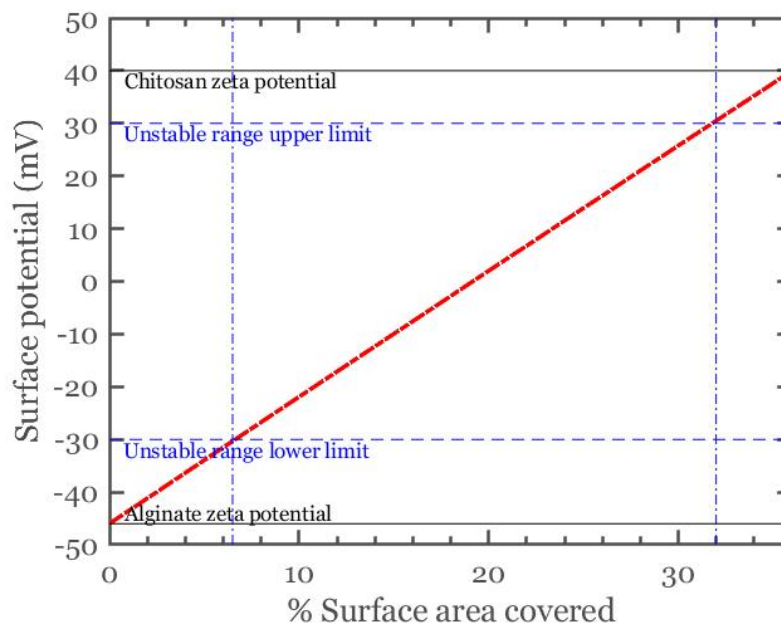


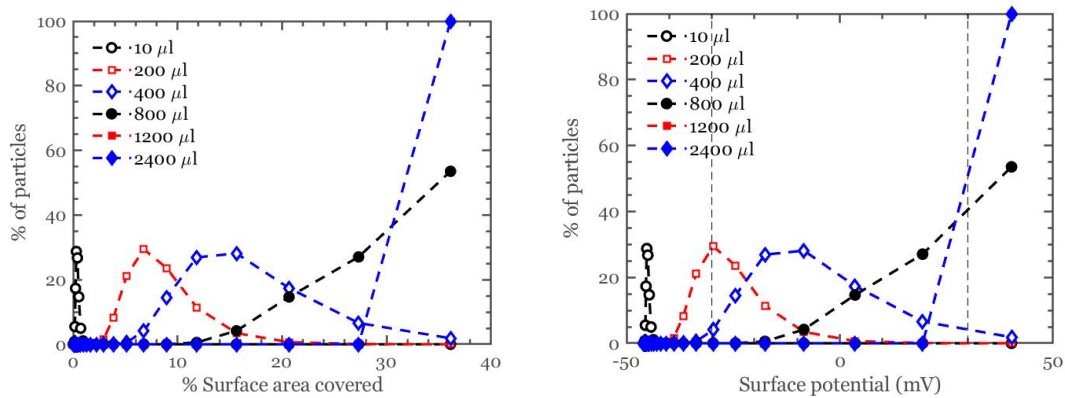
Figure 3.1: Surface potential of a monoaggregate with percentage surface area covered by chitosan nanoparticles

started to increase and moved towards a positive surface potential. At about 20% coverage the monoaggregate became neutral. As the coverage increased more and reached about 36% coverage, the surface potential became equal to that of chitosan particles. Since, it was assumed that with increasing surface coverage the surface potential would remain constant at this level and would not increase more than the surface potential of an individual chitosan particle, only this range was studied.

It is generally considered that colloidal suspensions are stable when the particles have an absolute zeta potential ≥ 30 mV (Gumustas et al., 2017). In other words, when all the colloidal particles in the system have a zeta potential between ± 30 mV the particles have a tendency to aggregate. In Figure 3.1, the stable region zeta potential limits were shown with dotted blue lines and corresponding surface area coverage limits were shown with black dotted lines. Any monoaggregate with a surface coverage inside that region would have a tendency to aggregate and form heteroaggregates.

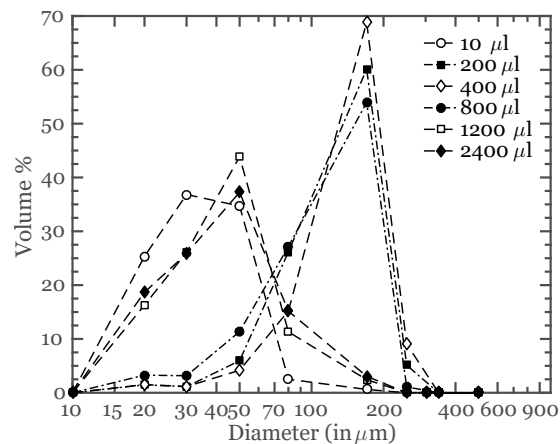
The number distribution of monoaggregates was shown with the percentage surface coverage and surface potential of the monoaggregates in Figures 3.2 and 3.3 for respectively 0.1 g and 0.2 g of alginate. It can be seen in Figure 3.2a, that as more chitosan was added to the system, the distribution shifted to the right or in other words, the number of monoaggregates with higher surface coverage increased. With 10 μl of chitosan, there is very little coverage on all the monoaggregates. For 200 μl of chitosan, most of the monoaggregates seem to have about 8% surface area coverage which increases to about 10-12% for 400 μl of chitosan, 20% for 800 μl of chitosan and finally for 1200 and 2400 μl of chitosan, most of the heteroaggregates seem to have the surface coverage which is equal to the limiting surface area coverage of the model that corresponds to the monoaggregate surface potential equal to that of chitosan.

In Figure 3.2b, the monoaggregate number distribution was plotted with monoaggregate surface potential. The unstable region mentioned before is shown with black dotted lines. It can be observed that for 10 μl of chitosan, all the monoaggregates have negative surface potential which results in very little heteroaggregation as reflected in the experimental final heteroaggregate PSD shown in Figure 3.2c. As the chitosan amount increases to 200 μl of chitosan, most of the monoaggregates have a surface potential that is within the unstable region and therefore prone to heteroaggregation. Similarly, for 400 μl of chitosan completely and for 800 μl of chitosan partially the monoaggregate distribution lies within the unstable region. This is in accordance with the fact that most heteroaggregation is seen for these three cases in the experiments as well (Figure 3.2c). For higher chitosan amounts of 1200 and 2400 μl of chitosan, all the monoaggregates seem to have a surface potential greater than the unstable region limit which hinders the agglomeration of these monoaggregates and that is also seen in the leftward shift of the final heteroaggregate PSD in Figure 3.2c.



(a) Monoaggregate number distribution with respect to monoaggregate surface coverage for different chitosan amount

(b) Monoaggregate number distribution with respect to monoaggregate surface potential for different chitosan amount

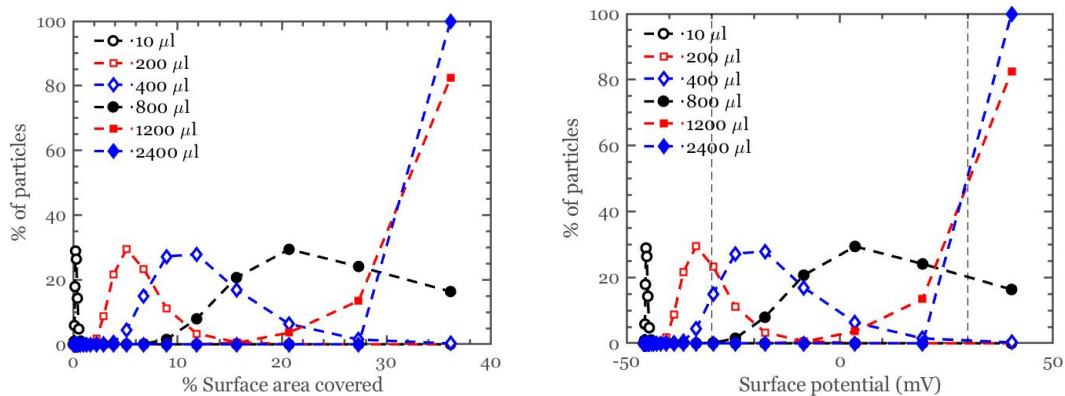


(c) Experimentally observed variation of final heteroaggregate particle size distribution for different chitosan amount

Figure 3.2: Validation of the layering model by comparison of experimentally acquired heteroaggregate PSD with monoaggregate number distribution for alginate amount of 0.1 g

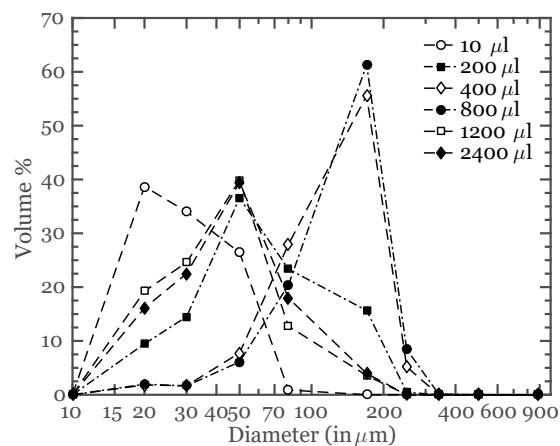
For 0.2 g of alginate, a similar trend to Figure 3.2a was observed in Figure 3.3a. With increasing chitosan amount, surface area coverage increased. From almost no surface coverage at 10 μl of chitosan, the peak of the monoaggregate distribution moved to about 6%, 11-12%, 20% for 200, 400 and 800 μl of chitosan respectively. For 1200 μl of chitosan, almost all the particles had a surface coverage equal to the limiting coverage and for 2400 μl of chitosan all monoaggregates had the highest possible surface area coverage.

From Figure 3.3b, it could be seen that for 10, 1200 and 2400 μl of chitosan all the monoaggregates were inside the stable region, thereby resulting in very little heteroaggregation which was also seen in Figure 3.3c. For 400 and 800 μl of chitosan almost all the monoaggregates were in the unstable region resulting in highest growth observed in Figure 3.3c. For 200 μl of chitosan, unlike the 0.1 g alginate case, most monoaggregates were in the stable region which agreed with the fact that the final heteroaggregate distribution shown in Figure 3.3c was more similar to that of 1200 and 2400 μl of chitosan than that of 400 and 800 μl of chitosan.



(a) Monoaggregate number distribution with respect to monoaggregate surface coverage for different chitosan amount

(b) Monoaggregate number distribution with respect to monoaggregate surface potential for different chitosan amount



(c) Experimentally observed variation of final heteroaggregate particle size distribution for different chitosan amount

Figure 3.3: Validation of the layering model by comparison of experimentally acquired heteroaggregate PSD with monoaggregate number distribution for alginate amount of 0.2 g

3.3 Experimental study of layering

3.3.1 Experimental procedure

To study the monoaggregate structure, alginate beads are used since it is easier to handle individual alginate beads and study them. For this purpose chitosan solution of different volumes (0, 10, 400 and 2000 μl) were added to 0.1 alginate beads in 10 ml of water. The chitosan amounts were chosen to represent the three different heteroaggregation regimes described in chapter 2 and a control case. The solutions were left for a day to allow sufficient time for layering. Afterwards, about 4-5 individual alginate beads were taken out of the solution. Liquid nitrogen was poured on top of the particles to freeze them. After that, frozen alginate beads were placed on carbon tapes on aluminum stubs for SEM analysis. Extreme caution was taken during this step to ensure that the particles are not pressured and deformed in any way. In the next stage the samples were left in a desiccator overnight for drying. Finally, samples were gold coated at a thickness of 10 nm to acquire better signal in the SEM. SEM analysis was performed in the following step in a FESEM (Zeiss-Sigma, Oberkochen, Germany) using an accelerating voltage of 5 kV and at a working distance of about 8.5 mm.

3.3.2 Results & discussion

The SEM images of alginate bead without any chitosan, and alginate beads from systems with 10, 400 and 2000 μl of chitosan are shown in Figure 3.4 at 200X magnification. It can be seen that the particles are shrunk severely. This is a result of the drying in desiccator which is necessary to prevent the interference of water vapor with the electron beam from a wet sample in the SEM. As the alginate and chitosan particles are hydrogel particles, they are filled with large amounts of water. This leads to the massive shrinkage of the particles when left in

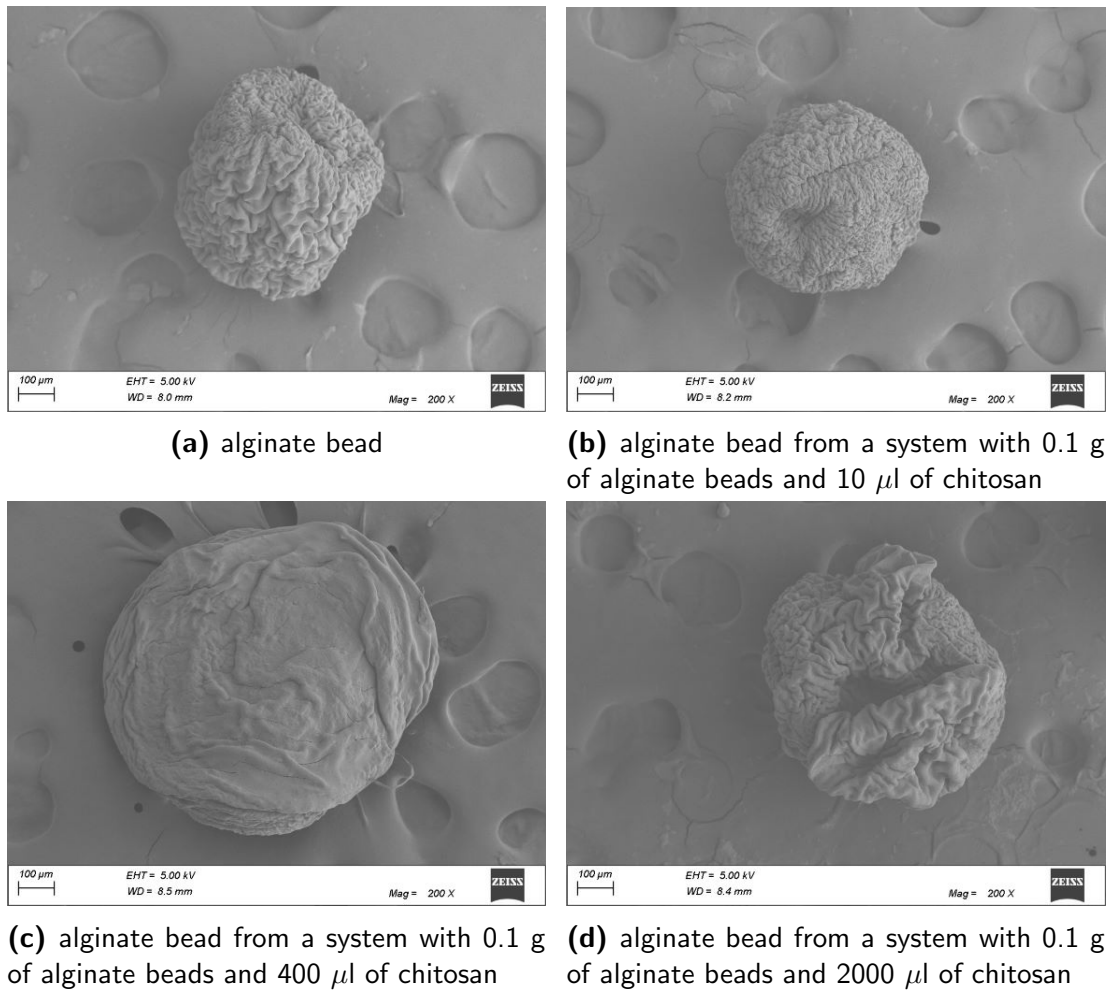


Figure 3.4: SEM images of alginate beads with chitosan layering on it at 200X magnification

the desiccator. The alginate bead surface became very curvy due to this shrinkage which made separating the surface roughness due to chitosan layering and shrinkage difficult. At the same time, chitosan particles also shrunk significantly. The chitosan particles were previously seen to be shrinking by a factor of 18 in volume (Yu et al., 2013) which is equivalent to about a 2.5 times decrease in the diameter. The 10 nm thick gold coating also contributed to reduced detect-ability of chitosan layers.

The SEM images of the four samples mentioned above are shown in Figures 3.5, 3.6, 3.7 and 3.8 respectively both at 1000X and 10000X magnification. In

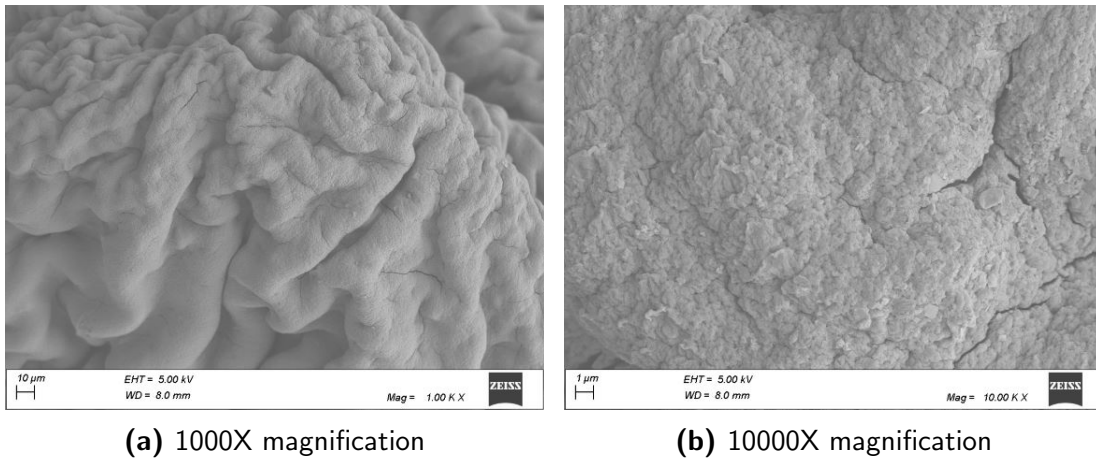


Figure 3.5: SEM images of an alginate bead

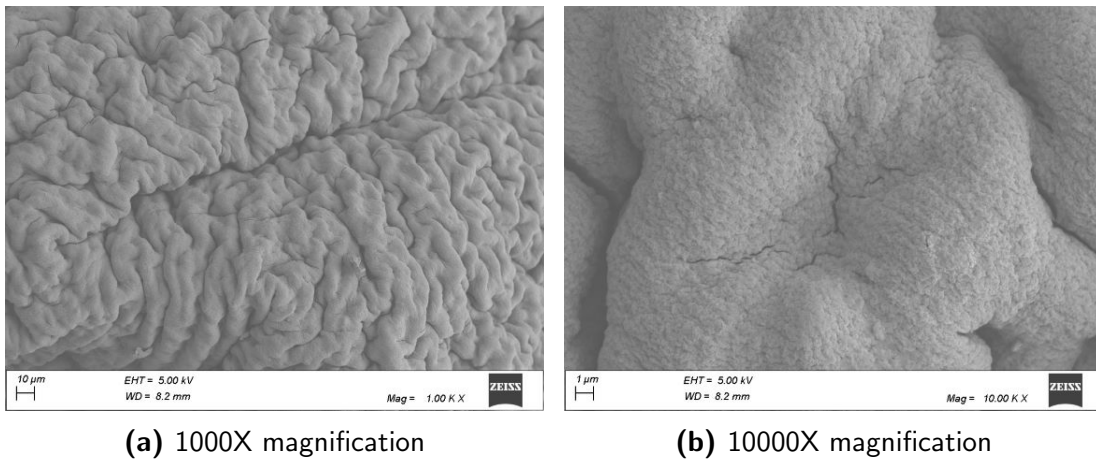


Figure 3.6: SEM images of an alginate bead from a system of 0.1 g alginate beads with 10 μl chitosan

Figure 3.5 some sharp crystal like structures can be seen but smooth or rounded bumps that are visible in the others are absent. This indicates that the smooth bumps likely are chitosan layers on the alginate. It can be seen that the number or net area covered by the smooth bumps increase slightly as the chitosan amount increases from Figure 3.6 to Figure 3.7 and finally at the highest chitosan content, in Figure 3.8 much more elongated surface features can be seen which possibly indicates an increase in chitosan layering with increasing chitosan amount.

The SEM images indicate a tendency of chitosan to form layers that are non-uniform and in form of patches. This is in line with what other researchers

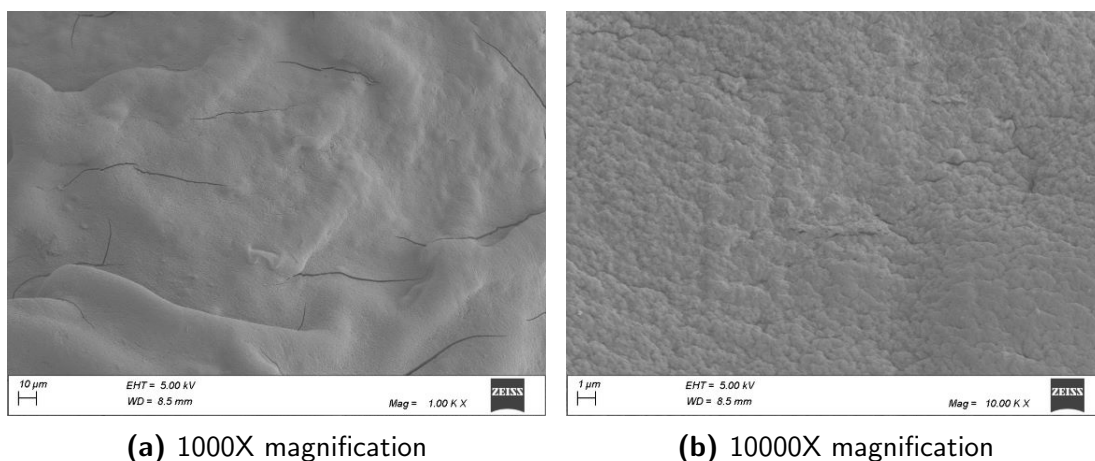


Figure 3.7: SEM images of an alginate bead from a system of 0.1 g alginate beads with 400 μl chitosan

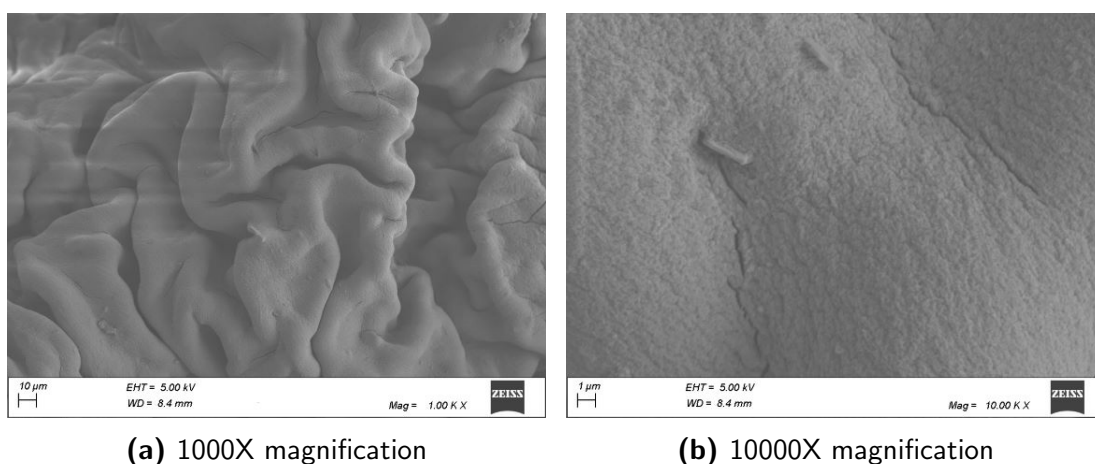


Figure 3.8: SEM images of an alginate bead from a system of 0.1 g alginate beads with 2000 μl chitosan

have observed before. In cases of particles that are less dissimilar in terms of size than the ones in our case, it was seen that chainlike agglomerate structures are formed rather than symmetrical structures. That possibly happened due to patchy layering of the smaller particles on the larger ones which formed neutral surface patches on the larger particles which attached to neutral patches on other particles in a non-symmetrical way and thereby creating a chainlike agglomerate.

As can be seen, the overall extent of layering was low which is consistent with the model findings which showed that the monoaggregates surface charge reached

the level of chitosan surface charge at a very low surface coverage. This low surface coverage was probably pronounced in the SEM images due to the shrinkage of the alginate beads and the chitosan particles and also the gold coating, as explained earlier.

3.4 Development and experimental validation of an integrated heteroaggregation process model

3.4.1 Mathematical model development

The layering framework was adopted to fit into the model developed for the agglomeration stage in Chapter 2. Instead of change of particle distribution through any one mechanism such as agglomeration or layering, particles were allowed to undergo both mechanisms simultaneously. In other words, some particles could undergo layering while other particles that already had ‘enough’ layering could agglomerate with other monoaggregates.

The particle number changes according to the following expression:

$$\frac{\partial}{\partial t}N(a, c, t) = R_{formation}(a, c) - R_{depletion}(a, c) + R_{layering}(a, c) \quad (3.12)$$

where, $N(a, c, t)$ is number of aggregates with alginate volume a and chitosan volume c at time t . $R_{formation}(a, c)$, $R_{depletion}(a, c)$ and $R_{layering}(a, c)$ respectively represent the rates of formation, depletion and layering of particles of alginate volume a and chitosan volume c .

Rates of formation and depletion through agglomeration are calculated in the same way as described in Chapter 2. The rate of layering calculation shown in Section 3.2.1 is modified for a 2-dimensional system that is necessary to represent the heteroaggregates where the alginate volume is not constant. The rate of layering can be expressed as shown below.

$$R_{layering}(a, 1) = -N(a, 1) \frac{K_{layering}(a, 1)}{(v_c(2) - v_c(1))} \quad (3.13)$$

$$R_{layering}(a, nc) = N(a, nc - 1) \frac{K_{layering}(a, nc - 1)}{(v_c(nc) - v_c(nc - 1))} \quad (3.14)$$

and,

$$\begin{aligned} R_{layering}(a, 2 : nc - 1) = & N(a, 1 : nc - 2) \frac{K_{layering}(a, 1 : nc - 2)}{(v_c(2 : nc - 1) - v_c(1 : nc - 2))} \\ & - N(a, 2 : nc - 1) \frac{K_{layering}(a, 2 : nc - 1)}{(v_c(3 : nc) - v_c(2 : nc - 1))} \end{aligned} \quad (3.15)$$

where, $K_{layering}(a, c)$ is the layering kernel for an aggregate with alginate volume and chitosan volume represented by a and c , $v_c(c)$ is the volume of chitosan in an aggregate and $v_c(nc)$ is the highest volume of chitosan that any particle in the system can have.

The layering kernel, $K_{layering}$ calculation from Section 3.2.1 is also modified for a 2-dimensional system and is calculated as shown in the following equation.

$$K_{layering}(a, c) = \frac{K_B}{W(a, c)} \frac{(R_{(a,c)}^{-1} + R_{chitosan}^{-1})(R_{(a,c)} + R_{chitosan})}{4} \quad (3.16)$$

where, W is the Fuchs stability constant. $R_{(a,c)}$ and $R_{chitosan}$ are respectively the radii of an aggregate with alginate volume of a and chitosan volume of c and a monodispersed chitosan particle. $K_B = 8kT/3\mu$ is the collision rate constant between an aggregate and the individual chitosan particles due to Brownian motion.

The Fuchs stability constant is calculated using the following expression.

$$W(a, c) = 2 \int_2^\infty \frac{\exp(U(a, c, l)/kT)}{G(a, c, l)L(l)^2} dL \quad (3.17)$$

where, $U(a, c, l)$ is the total interaction potential between an aggregate with alginate and chitosan volume of a and c respectively. $G(a, c, l)$ is the hydrodynamic resistance which is not considered in this model. kT is the thermal energy of the system. $L(l)$ ($= r(l)/A(a, c)$) is the dimensionless center-to-center distance where

r is the actual distance between particle centers. $A(a, c)$ is the average radius of an aggregate and a chitosan particle and is calculated as $A = (R_{(a,c)} + R_{chitosan})/2$.

The total interaction potential is the sum of the van der Waals, electrostatic and hydration interaction potential:

$$U = U_{van\ der\ Waals} + U_{electrostatic} + U_{hydration} \quad (3.18)$$

where, $U_{van\ der\ Waals}$, $U_{electrostatic}$ and $U_{hydration}$ are respectively the van der Waals, electrostatic and hydration interaction potential.

The van der Waals interaction potential between an aggregate and a monodispersed chitosan particle is calculated as (Elimelech et al., 1995):

$$U_{van\ der\ Waals}(a, c, l) = -\frac{A_H}{6} \times \left[\frac{8\omega(a, c)}{(1 + \omega(a, c))^2} \left[\frac{1}{(L(l)^2 - 4)} + \frac{1}{L(l)^2 - 4 \left(\frac{1 - \omega(a, c)}{1 + \omega(a, c)} \right)^2} \right] + \ln \left[\frac{L(l)^2 - 4}{L(l)^2 - 4 \left(\frac{1 - \omega(a, c)}{1 + \omega(a, c)} \right)^2} \right] \right] \quad (3.19)$$

where, A_H is the Hamaker constant. $\omega(a, c)$ is the radii ratio of the aggregate and a chitosan particle and calculated as $\omega(a, c) = R_{(a,c)} / R_{chitosan}$. $L(l)$ is the dimensionless center-to-center distance.

The electrostatic interaction potential acting between an aggregate and individual chitosan particles is calculated as (Sader et al., 1995):

$$U_{electrostatic}(a, c, l) = \frac{4\pi\epsilon_0\epsilon_r\omega(a, c)A(a, c)\psi_{(a,c)}^2}{(1 + \omega(a, c))^2 L(l)} \times \{ (1 + \Psi(a, c))^2 \ln(1 + \exp[-\kappa A(a, c)(L(l) - 2)]) + (1 - \Psi(a, c))^2 \ln(1 - \exp[-\kappa A(a, c)(L(l) - 2)]) \} \quad (3.20)$$

where, $\Psi(a, c) = \frac{\psi_{(a,c)}}{\psi_{chitosan}}$ is the ratio of surface potential of the aggregate with alginate volume of a and chitosan volume c to the surface potential of a chitosan nanoparticle. $\epsilon_0\epsilon_r$ is the permittivity of the dispersant and $\kappa = \sqrt{\frac{e^2 N_A \sum_n z_n^2 C_n^b}{\epsilon_0 \epsilon_r k T}}$ is

the Debye-Huckel parameter, where, e is the electron charge, N_A is the Avogadro number, z_n and C_n^b are valance and bulk concentration of species (ion) n .

The hydration energy for layering of chitosan on aggregates was calculated as shown in Israelachvili (1992):

$$U_{hydration}(a, c, l) = \frac{4 \pi \omega(a, c) A(a, c)}{(1 + \omega(a, c))^2} \times F_0 \delta_0^2 \exp \left(-\frac{A(a, c)}{\delta_0} (L(l) - 2) \right) \quad (3.21)$$

where, F_0 is the hydration force constant and δ_0 is the decay length.

3.4.2 Results & discussion

The layering model combined with the agglomeration model developed in Chapter 2 was used to simulate particle size distributions at the end of the heteroaggregation process. Similar to Figure 2.6, the effect of relative alginate and chitosan concentration on D_{10} , D_{50} and D_{90} was plotted in Figure 3.9. The combined model was able to replicate the behavior of the agglomeration only model without any assumptions about the initial PSD. As chitosan amount increased for both 0.1 g and 0.2 g alginate, size enlargement of particles was observed which resulted in an increase in D_{10} , D_{50} and D_{90} indicating the transition from ‘dispersed, uncoated’ regime to ‘agglomerated’ regime. As the chitosan amount increased even more, D_{10} , D_{50} and D_{90} decreased as the ‘agglomerated’ regime transitioned to ‘dispersed, coated’ regime and the particle size decreased.

A shortcoming of this model compared to the agglomeration only model can be seen on close observation of Figure 3.9. The D_{10} , D_{50} and D_{90} values for both 1200 μl and 2400 μl were very similar. Also, D_{10} , D_{50} and D_{90} values for the 10 μl was slightly higher than the ones estimated by agglomeration only model as shown in Figure 2.6. Both of these behaviors can be attributed to enhanced layering prediction by the layering model. As the monoaggregates for 10 μl case had more chitosan for the combined model compared to agglomeration model, more of

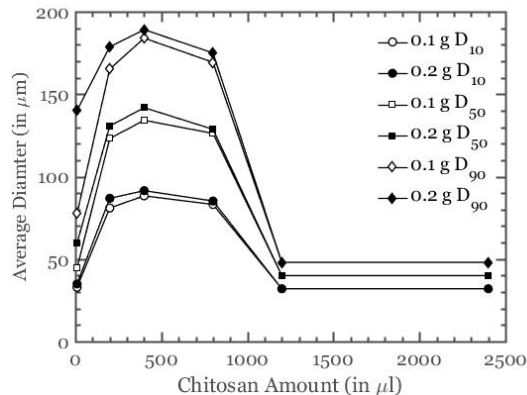


Figure 3.9: Combined PBM and layering model estimated variation of D_{10} , D_{50} and D_{90} with chitosan amount for 0.1 g and 0.2 g of alginate

the monoaggregates had a surface charge close to neutral resulting in heteroaggregation and thus higher D_{10} , D_{50} and D_{90} . For the same reason, monoaggregates acquired high amounts of chitosan even at 1200 μl which prevented further aggregation. When the chitosan amount was increased to 2400 μl , monoaggregates had even more chitosan and thus a lesser chance of further heteroaggregation after the layering stage.

3.5 Chapter conclusions

A 1-dimensional population balance model was developed for the layering stage of the agglomeration process. Using the model, the increase in surface potential with increasing surface area coverage of the monoaggregate by chitosan was studied. It was seen that at no surface coverage, as expected, the monoaggregate surface potential was equal to that of an alginate particle. With increasing surface coverage the surface potential increased and then reached the surface potential of chitosan particles at maximum allowed surface coverage in the model. At about 20% surface area coverage the monoaggregates became neutral. It was thought that with increasing surface area coverage the surface potential of the monoaggregate would remain equal to that of most positively charged particles in the

system which were chitosan nanoparticles.

An absolute zeta potential less than 30 mV is considered to lead to unstable suspensions where particles do not repel each other enough to overcome the attractive van der Waals force and they agglomerate. It was seen that monoaggregates within 6-32% surface area coverage were likely to agglomerate with each other.

The relation of the number distribution of monoaggregates with the percentage surface coverage and surface potential of the monoaggregates was also investigated. As expected, with more chitosan in the system, the number distribution shifts to the right which meant that the number of monoaggregates with higher surface coverage and higher surface potential increased. For 0.1 g of alginate and 10, 1200 and 2400 μl of chitosan, most or all monoaggregates had a surface potential that was in the stable region and therefore large heteroaggregate formation was less compared to 200, 400 and 800 μl of chitosan cases where most monoaggregates were in the unstable region which lead to the formation of large heteroaggregates. The model findings were validated by comparing with experimental heteroaggregate PSDs, which matched with the layering model results. In case of 0.2 g alginate, both model and experimental results showed that the system progressed towards ‘dispersed, uncoated’ regime for 10 and 200 μl of chitosan. Addition of 400 and 800 μl of chitosan lead to ‘agglomerated regime’ and 1200, 2400 μl of chitosan lead to ‘dispersed, coated’ regime.

The layering of chitosan on alginate beads is also studied. The shrinkage of the alginate beads and chitosan nanoparticles due to drying prior SEM analysis reduced the visibility of chitosan layers on the surface of alginate beads. However, a slight increase in chitosan layering was observed with increasing chitosan amount in the system. The overall low surface coverage observed is in agreement with the low surface coverage observed in the model. The chitosan layer is also found to be non-uniform and patchy which is similar to what has been found by other

researchers previously.

The layering model is integrated in the 2-dimensional framework developed in Chapter 2. The combined agglomeration-layering model was able to capture the general trend of the system transition from one regime to another without any assumption about the initial monoaggregate distribution. However, an over-prediction of the layering was observed, which points towards the need of a more detailed discrete element method model for the simulation of the layering stage.

Chapter 4

Study of adsorption characteristics of alginate, chitosan and heteroaggregates for the adsorption of positive & negative heavy metal ions

The contents of this section have been submitted to a journal for consideration for publication as:

- **A. Chaturbedi**, S. Patil, R. Ramachandran, N. Shapley. Adsorption of positively and negatively charged heavy metal ions from wastewater by heteroaggregates of biopolymer particles.

4.1 Background & objectives

Elements with density greater than 5-6 g/cc are considered to be heavy metals. Various chemical-intensive industries produce large amount of waste-water with considerable amount of heavy metals in it. Metal finishing and electroplating industries generate waste-water with cadmium, chromium, zinc, lead, copper, silver etc. Another significant source of waste-water containing heavy metals is metal mining and smelting industries. Textile industries, because of the dyeing process produce waste water with chromium, copper, nickel, lead in it. Manufacturing of printed circuit boards also generates waste-water consisting of heavy metals such as tin, lead and nickel (Akpore et al., 2014).

Heavy metals have detrimental effects on plants and animals. Copper can cause liver damage, Wilson's disease, insomnia. Cadmium can result in kidney damage, renal disorder and cancer. Chromium is the reason behind diarrhea,

nausea, cancer. Lead and mercury can cause damage to the fetal brain, result in kidney diseases and create problems to the circulatory and nervous systems (Barakat, 2011).

Heavy metals, due to their non-biodegradable and toxic nature are considered to be among the most hazardous chemicals. Additionally, since heavy metals are very soluble in aqueous environment, they are easily transported and absorbed by animals and plants alike. The harmful nature of heavy metals and the abundance of industries generating heavy metal containing waste-water make the removal of heavy metals from industrial waste-water vital before the emission of waste-water to the environment.

As mentioned earlier, very recently, customized heteroaggregates have also been suggested as good water purifying agents (Yu et al., 2013). This is based on the idea that oppositely charged components of the heteroaggregates will adsorb toxic anions and cations which include charged heavy metal compounds such as cadmium, mercury, lead, copper, chromium and arsenic from wastewater. The current work is based on the same idea of exploiting the opposing charges of the heteroaggregate components to adsorb oppositely charged heavy metal ions from wastewater. Depending on the initial ratio of the components; the heteroaggregation process can progress towards three different regimes (as shown in Figure 4.1). The aggregates formed in these regimes differ in their structure and composition which may have an effect on the adsorption capacity of the individual components.

In several previous works, chitosan and alginate have been suggested by researchers as good water purifying agents. In gel particle form, chitosan and alginate have shown comparable adsorption capacity as that of commercial ion exchange resins (Yu et al., 2013). Extensive research has been conducted on the use of chitosan and alginate for water purification in general and specifically for removal of heavy metals by adsorption as well. Gotoh et al. (2004) studied the

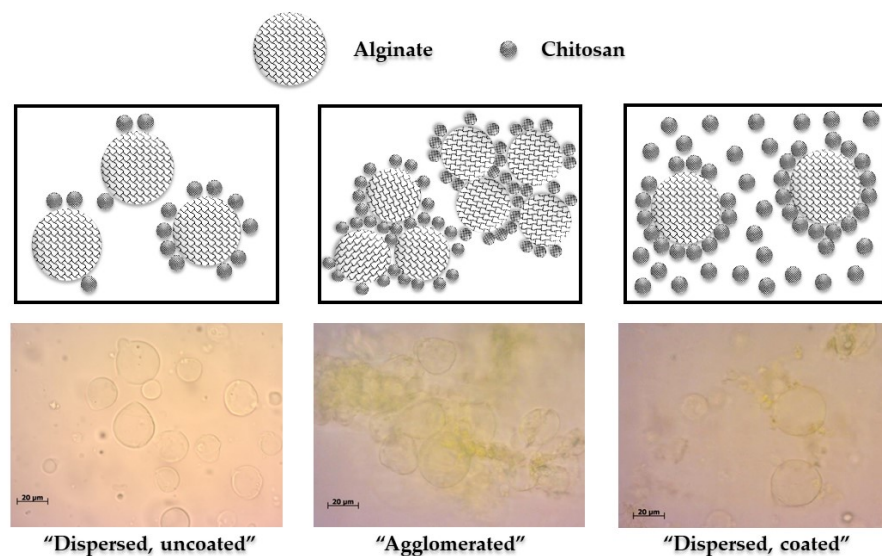


Figure 4.1: Different heteroaggregation regimes: “Dispersed, uncoated” (individual alginate microparticles ‘under coated’ with chitosan nanoparticles); “Dispersed, coated” (individual alginate microparticles ‘over coated’ with chitosan nanoparticles); “Agglomerated” (multiple alginate microparticles coated with chitosan nanoparticles agglomerated together)

adsorption of Cu(II), Co(II) and Cd(II) ions onto alginate-chitosan hybrid gel beads and showed that the adsorption was rapid and reached equilibrium within 10 min. Jang et al. (1995) studied the effect of pH on adsorption of Cu(II) ions onto alginate gel and observed 50% reduction in adsorption capacity as pH was reduced from 3.4 to 2.4. Williams et al. (1998) studied the adsorption of copper, nickel and cadmium on alginate. Chitosan, as well, has been used in various forms such as non-cross-linked, cross-linked, flake, cross-linked beads to adsorb various heavy metal ions such as chromium (Udaybhaskar et al., 1990; Sa and Aktay, 2002; Prez-Candela et al., 1995; Boddu et al., 2003), lead (Gonzalez-Davila et al., 1990; Ng et al., 2003), silver (Lasko and Hurst, 1999), zinc (Juang and Shao, 2002; Wang et al., 2004), mercury (Kyzas and Deliyanni, 2013), cadmium (Evans et al., 2002; Jha et al., 1988), uranium (Gerente et al., 1999), platinum (Guibal et al., 1999a), nickel (Juang and Shao, 2002).

The amine groups of the chitosan as shown in Figure 4.2a are considered

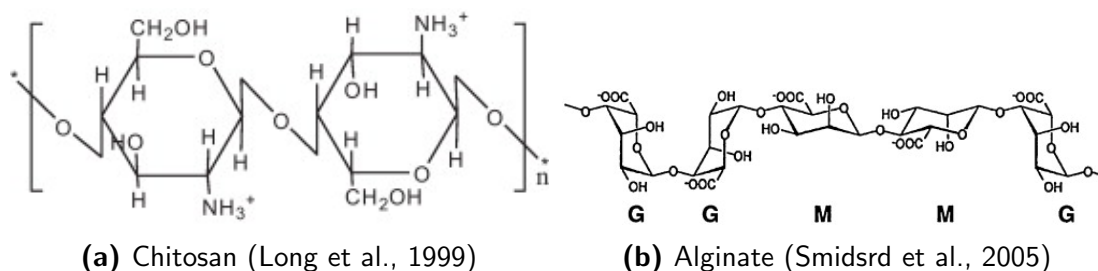


Figure 4.2: Structure of the biopolymers used in this study

the most active adsorption sites. The amine groups are protonated at acidic pH up to the pKa value of approximately pH 6.5, causing a positive charge on chitosan molecules. However, the hydroxyl groups present in the C-3 position can also participate in the adsorption process (Guibal, 2004). The main adsorption mechanism through which chitosan can adsorb positively charged metal ions is chelation. The chelation has been shown to occur in two routes: the “bridge” model and the “pendant” model. During chelation, nitrogen from the amine groups form covalent bonds with the metal ion and the hydroxyl group can also participate by releasing protons. When two sets of amine and hydroxyl groups from the same or adjacent chains of chitosan attach to the metal ions, the process is said to follow the “bridge” model (Figure 4.3a). Alternatively, when one set of amine and hydroxyl groups are replaced by water molecules, the adsorption model is termed the “pendant” model (Figure 4.3b). Chitosan cross-linked with sodium tripolyphosphate (TPP), as performed in this study, can also adsorb anions by ion exchange with the TPP.

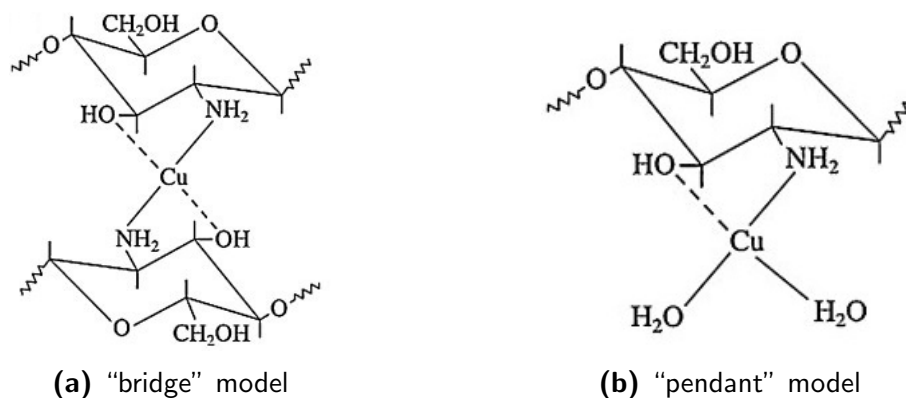


Figure 4.3: Chelation models (Monteiro and Airoidi, 1999)

The principal binding mechanism for alginate and positively charged ions is ion exchange. As shown in Figure 4.2b, the carboxyl groups of alginate are deprotonated in aqueous solutions except at very low pH. Therefore, for most practical pH values, the carboxyl groups are negatively charged. For calcium-alginate beads such as the ones used in this study, calcium ions cross-link two alginate chains by attaching with the deprotonated carboxyl groups according to the "egg-box" model (Figure 4.4). These calcium ions can be replaced by other positively charged metal ions during adsorption. In recent past, some studies have hypothesized that in addition to the "egg-box" model sites, adsorption can also occur at additional sites (Emmerichs et al., 2004; Donati et al., 2005; Siew et al., 2005; Rodrigues and Lagoa, 2006).

Molybdenum is considered toxic at concentration levels above 5 ppm (Moret and Rubio, 2003). Chronic exposure to Mo can result in weakness, headache, growth reduction, sterility and death (Namasivayam and Sangeetha, 2006). Mo ranks between Zn(II) and Cr(III) in terms of toxicity (Wu et al., 2001). Mo is used in electron tubes, high-strength steel alloys, heat resistant materials, vacuum tubes, as pigments for printing ink, paints and ceramics (Lou et al., 2015; Namasivayam and Sureshkumar, 2009). Due to the emission of Mo containing waste-water from these industries, Mo pollution has become a major problem in many parts of the world. Molybdenum exists in Mo(IV) and Mo(VI) forms,

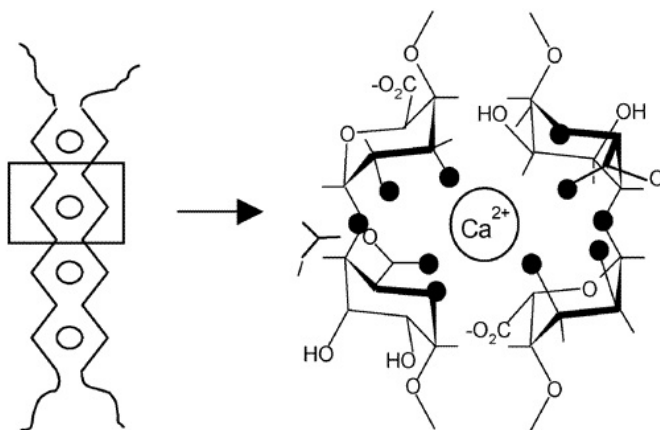


Figure 4.4: Structure of calcium alginate beads according to the “egg-box” model (Braccini and Perez, 2001)

however, Mo(VI) dominates and is present as MoO_4^{2-} . Several studies have been performed on Mo adsorption using adsorbents such as iron ore (Bostick et al., 2003), alumina (Wu et al., 2000, 2001), magnetic chitosan resins (Elwakeel et al., 2009), chitosan gel beads (Guibal et al., 1998, 1999b), maghemite nanoparticles (Afkhami and Norooz-Asl, 2009), sulfuric acid-modified cinder (Lian et al., 2012), carbon cloth (Afkhami et al., 2009).

Divalent copper, Cu(II) is very toxic and excessive consumption leads to respiratory problems, abdominal pain, liver and kidney failure and finally gastrointestinal bleeding. It also has harmful effects on the soil biota and many plant species. Copper is mostly released through effluents from metal cleaning and plating baths, paper board mills, pulp, wood pulp production and fertilizer industries (Akar et al., 2009). World Health Organization (WHO) defines the Cu(II) permissible limit in drinking water as 1.5 ppm while US EPA requires the concentration of copper in industrial waste water to be less than 1.3 ppm (Shawabkeh et al., 2004). Studies on removing copper using novel adsorbents have been performed using chitosan beads (Ngah et al., 2002), chitosan-GLA beads (Ngah and Fatinathan, 2008), chitosan-tripolyphosphate beads (Ngah and Fatinathan, 2010), chitosan-alginate beads (Ngah and Fatinathan, 2008; Yu et al., 2013).

The experimental data collected were fitted with Langmuir (Langmuir, 1917)

and Freundlich adsorption isotherms (Freundlich, 1906) to calculate the isotherm parameters. The Langmuir model is arguably the most popular adsorption model since it has excellent agreement with equilibrium adsorption behavior of a wide variety of systems. This model assumes that adsorption occurs at homogeneous adsorption sites with identical energy. It also assumes that all the adsorption happens on a monolayer and the intermolecular force decreases rapidly as the distance from adsorption sites increases. The Langmuir model has the following form:

$$Q = \frac{Q_{max}K_sC_e}{1 + K_sC_e} \quad (4.1)$$

where,

Q is the equilibrium adsorption capacity (in mg/g)

Q_{max} is the maximum adsorbent capacity at mono-layer coverage (in mg/g)

K_s is the Langmuir adsorption equilibrium constant (in L/mg)

C_e is the equilibrium adsorbate concentration (in mg/L)

The linear form of Langmuir model is as follows:

$$\frac{C_e}{Q} = \frac{C_e}{Q_{max}} + \frac{1}{Q_{max}K_s} \quad (4.2)$$

The Freundlich isotherm predicts that the equilibrium adsorption capacity increases with the adsorbate concentration as a power law. As opposed to the Langmuir model it assumes that the adsorption site energy decays exponentially. Hence, it is generally applied to multilayer adsorption. The Freundlich model can be expressed as:

$$Q = K_F C_e^{1/n} \quad (4.3)$$

where, K_F and n are empirical constants. $1/n$ represents adsorption intensity.

The linear form of Freundlich isotherm is shown below.

$$\log Q = \frac{1}{n} \log C_e + \log K_F \quad (4.4)$$

Objectives

The purpose of this study is to investigate the equilibrium adsorption capacity of heteroaggregates compared to that of their components. In addition, we aim to compare the adsorption of mixed ions (oppositely charged) with that of individual ions. We seek to investigate the presence of any synergistic or competitive effects in multi-ion adsorption on heteroaggregates. We use a mixture of oppositely charged ions as a more realistic model of real world waste-water as compared to single ion systems commonly studied in the literature. It is also important to study the adsorption characteristics of the heteroaggregates since they offer an advantage in capturing both the positive and negative ions over traditional adsorbents which generally have a higher affinity for ions of a particular charge. In addition, the large alginate particles in the heteroaggregates offer a support to the small chitosan nanoparticles which are rapid adsorbents with minimal internal diffusion limitations but need to be supported in adsorption equipment to prevent large pressure drops and loss of nanoparticles.

4.2 Experimental procedure

4.2.1 Materials

Low molecular weight (50-190 kDa) chitosan (deacetylation fraction 90.85 %, viscosity of 185 cP for a concentration of 1% w/w in 1% w/w acetic acid solution) (CAS #9012-76-4), 85% sodium tripolyphosphate (TPP) (CAS #7758-29-4, technical grade) and ammonium molybdate tetrahydrate (MW 1235.86 g/mol) (CAS #12054-85-2) were supplied by Sigma Aldrich (St. Louis, MO). Sodium alginate (molecular weight of 450-550 kDa, viscosity of 485 cP (for a 1% w/w solution)) (consisting of 65-75% guluronic acid (G) subunits and 25-35% mannuronic acid (M) subunits) (CAS #9005-38-3) and copper sulfate pentahydrate (MW 249.68

g/mol) (CAS #7758-99-8) were acquired from Acros Organics (Morris Plains, NJ). Calcium chloride (CAS #10035-04-8) and sodium chloride (CAS #7647-14-5) were supplied by Fisher Scientific (Pittsburgh, PA). Deionized water collected from Milli-Q water production system was used to prepare the solutions.

4.2.2 Instruments

Inductively coupled plasma - optical emission spectroscopy (ICP-OES) analysis was performed in an iCAP-7400 ICP-OES Duo SOP (Thermo Fisher Scientific, Waltham, MA). An Avanti J-E centrifuge (Beckman Coulter, Brea, CA) was used for centrifugation. The measurement of size and zeta potential of chitosan nanoparticles was done in a ZS-90 zetasizer (Malvern Instruments Ltd., Malvern, UK). A Misonix 3000 sonicator (Qsonica, Newtown, CT) was used to sonicate the suspension. For acquiring the microscope image of the alginate beads a Zeiss Axio Lab A1 optical microscope (Carl Zeiss, Thornwood, NY) was used.

4.2.3 Preparation of alginate bead

Larger alginate beads (diameter of 2 mm), as opposed to alginate microparticles, were used for the adsorption experiments. For preparation of alginate beads, 2 wt% sodium alginate solution was mixed with 2 wt% sodium chloride solution. A bath of 0.1 M calcium chloride solution was prepared to which sodium chloride was added to make a 0.075 M solution. A 5 cc syringe with a 30G 1/2 needle was attached to a syringe pump and the sodium alginate-sodium chloride solution was pumped into the bath in a drop-wise fashion from a height of 12 cm at a volumetric flow rate of 0.1 ml/min. The bath was stirred manually. The beads were collected after 15 minutes to allow for cross-linking to be complete. These beads were then stored in deionized water.

4.2.4 Heteroaggregation experiments

Three types of heteroaggregates were studied as adsorbents in this study. The heteroaggregates were chosen such that they represent the distinct heteroaggregation regimes determined in our previous work (Chaturbedi et al., 2016). To produce the heteroaggregates, firstly, 0.1 g of alginate beads were added to 10 ml of deionized water. Depending on the desired heteroaggregation regime, 10 μl ('dispersed, uncoated' regime), 400 μl ('agglomerated' regime) or 2000 μl ('dispersed, coated' regime) of chitosan suspension (of concentration 0.04 g/ml) was added to the alginate and water mixture. The mixture was sonicated for 30 seconds at 15 W power to break down any initial aggregates and to generate a homogeneous suspension. The mixture was left to rest for 30 minutes to ensure that the individual components had enough time to form the heteroaggregates.

4.2.5 Equilibrium adsorption experiments

To study the equilibrium adsorption capacity of chitosan for Mo(VI) ions, ammonium molybdate tetrahydrate solutions of different concentrations (0-4000 mg/L) were prepared and 3 ml of these solutions were added to test tubes containing 0.1 g of chitosan nanoparticles. These solutions were sonicated to uniformity at 9-12 watts for 30 seconds and then kept under magnetic stirring for a week. An excess amount of ion solution (3 ml) was used and the adsorption was allowed to continue for a week to ensure equilibrium adsorption. Afterwards, the solutions were centrifuged at 20,000 RPM for 30 minutes to separate the particles from the liquid. After centrifugation, the supernatant was collected and filtered using a 0.22 μm syringe filter. Subsequently, the samples were diluted 2-2000 times using 2% nitric acid depending on the initial concentration of the ion solution. The dilution factor was chosen such that the approximate final ion concentration of the samples remained between 115 ppb ($\mu\text{g/L}$)-50 ppm (mg/L), which was the

most suitable range for the ICP-OES used for analysis. A similar process was followed for the investigation of the equilibrium adsorption capacity of alginate. However, 0.2 g of alginate beads was used and samples were centrifuged at 10,000 RPM instead of 20,000 RPM (used for chitosan) since they were easily separable from the solution due to their large size.

For adsorption experiments with heteroaggregates, as mentioned before, 10 ml of heteroaggregate solution was used and 10 ml of ion solution was used. The final ion solution concentrations were kept the same as for the experiments with individual adsorbents. In case of heteroaggregates, the sonication and stirring steps were not performed to prevent breakage of the heteroaggregates. As mentioned in Section 4.2.4, the total amount of adsorbent used was 0.1 g alginate with 0.0004 g, 0.016 and 0.08 g chitosan, respectively, in heteroaggregates with 10, 400 and 2000 μl of chitosan. The rest of the process remained the same as in the experiments with chitosan or alginate.

The same set of experiments was repeated with a solution containing only copper sulfate pentahydrate in the same molar concentrations as those of ammonium molybdate tetrahydrate. Subsequently, both ammonium molybdate tetrahydrate and copper sulfate pentahydrate, each of the same concentrations as for individual ions, were mixed with alginate beads, chitosan nanoparticles and heteroaggregates. Both salts were added in the same molar concentration. The complete design of experiments is shown in Figure 4.5.

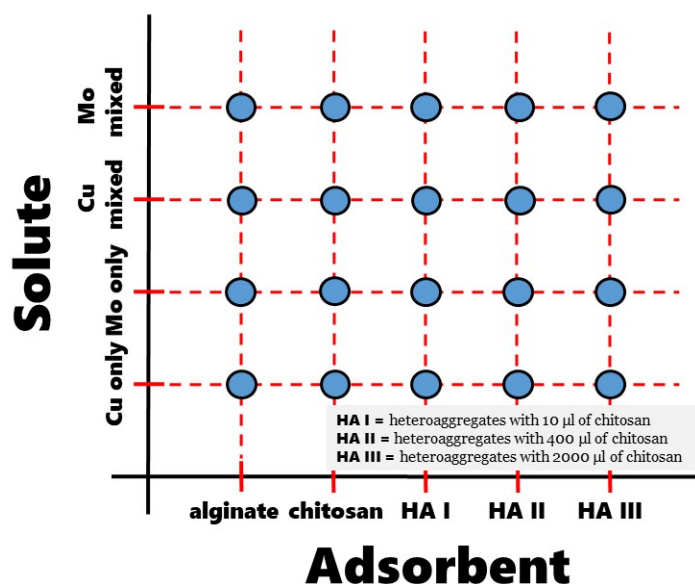


Figure 4.5: Schematic showing the design of experiments

4.2.6 ICP-OES analysis

The concentration of ions remaining in the supernatant liquid post adsorption was measured by inductively coupled plasma optical emission spectrometry (ICP-OES). Mo(VI) ion concentration was measured at 202.030, 203.844, 204.598 nm in radial mode. Cu(II) ion concentration was measured at 224.7, 324.754 and 327.396 nm in radial mode. These wavelengths were chosen based on the highest sensitivity of the ions at these wavelengths. Wavelengths at which both ions were sensitive, were avoided to eliminate overlapping signals. Before measuring each set, a set of calibration samples of the corresponding ions (copper, molybdenum or a mixture of both) of concentration 1, 3, 5, 7, 10, 30, 50 mg/L (ppm) was analyzed to get the calibration curve which was then used to calculate the concentration of the samples of unknown concentrations.

4.2.7 Particle characterization

Dynamic light scattering was used in the zetasizer to measure the size of the chitosan nanoparticles. Phase analysis light scattering was used in the same equipment to measure the zeta potential of the nanoparticles. The alginate gel beads were observed under an optical microscope and the image was recorded with AxioVision software under 5x magnification.

4.3 Results & discussion

4.3.1 Particle characterization

The average diameter of the chitosan nanoparticles was found to be 251.3 ± 3.3 nm which is close to previously reported chitosan nanoparticle diameter produced by the same ionic gelation method (Yu et al., 2013). The diameter of the alginate beads was measured by optical microscopy. It was seen that most of the beads have a spherical shape (Figure 4.6) and a diameter of around 1.5 mm.

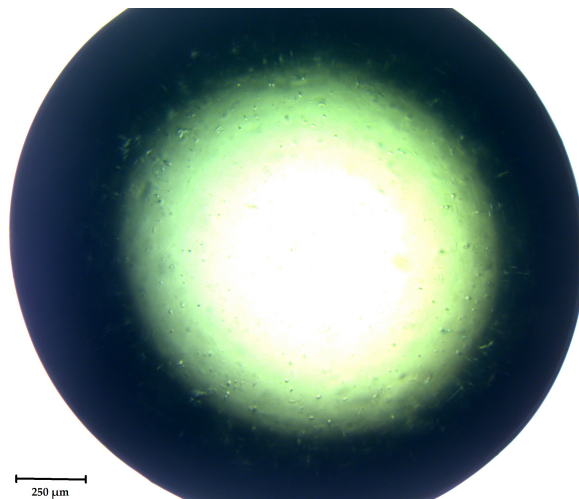


Figure 4.6: Optical microscope image of alginate beads

Zeta potential indicates the strength of electrostatic inter-particle interactions. Average zeta potential of the chitosan nanoparticles was found to be 39.6 mV at

pH 7. The positive zeta potential is due to the presence of protonated amine groups as shown in Figure 4.2a. Although the alginate beads studied here are too large for zeta potential measurements to be obtained by zetasizing instruments, Sarei et al. (2013) found that alginate nanoparticles of size 70 nm exhibit zeta potential values of -46.7 mV. The negative zeta potential is due to the carboxyl groups present in alginate (Figure 4.2b).

4.3.2 Equilibrium adsorption capacity

The equilibrium adsorption capacity of each adsorbent-adsorbate combination (shown in Figure 4.5) was studied according to the procedure described in Section 4.2. In all the figures in this section the equilibrium adsorption capacity, Q (amount of adsorbate adsorbed per unit amount of adsorbent) is plotted with the equilibrium concentration of the adsorbate in the solution, C_e .

4.3.2.1 Comparison between adsorbents

In this section, the equilibrium adsorption capacity of various adsorbents such as alginate beads, chitosan nanoparticles and heteroaggregates from three different heteroaggregation regimes has been investigated for the adsorption of copper from a solution of only copper sulfate, molybdenum from a solution containing only ammonium molybdate, and both copper and molybdenum from a mixed solution containing both copper sulfate and ammonium molybdate. The coefficients from Langmuir and Freundlich isotherm fits of the adsorption curves are shown in Table 4.1.

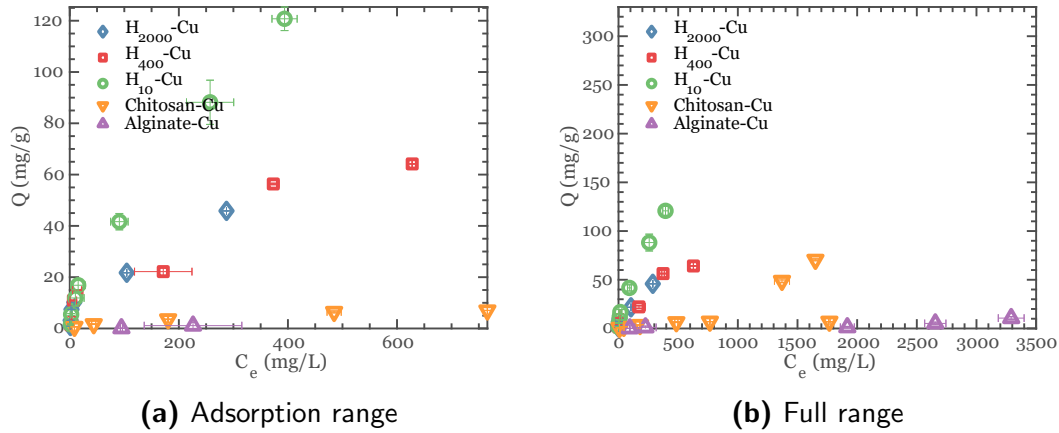


Figure 4.7: Adsorption of copper on various adsorbents. *Alginate-Cu* represents the adsorption of copper on alginate. *Chitosan-Cu* represents the adsorption of copper on chitosan. H_{10} -Cu, H_{400} -Cu and H_{2000} -Cu respectively represent the adsorption of copper on heteroaggregates with 10, 400 and 2000 μ l of chitosan.

Adsorption of copper

It can be seen from Figure 4.7 that the equilibrium adsorption capacity of all of the heteroaggregates is an order of magnitude higher than the maximum equilibrium adsorption capacities of individual adsorbents. It can also be seen that the equilibrium adsorption capacity is highest for heteroaggregates with 10 μ l of chitosan followed by the heteroaggregates with 400 and 2000 μ l of chitosan, which are very similar to each other. Among the heteroaggregates, the mass ratio of alginate to chitosan is the highest in the heteroaggregates with 10 μ l of chitosan, and in previous work (Yu et al., 2013) it was found that alginate has a higher density of adsorption sites for copper ions than chitosan does, even though both individual adsorbents adsorb copper ions, alginate by opposite charge attraction and chitosan by complexation. Therefore, among the heteroaggregates, the extent of interaction between the negative functional groups of alginate and positively charged copper is greatest for heteroaggregates with 10 μ l of chitosan, resulting in a higher equilibrium adsorption capacity than for other heteroaggregates. The

significant synergistic effect observed between alginate and chitosan in heteroaggregates could be due to a modification in structure of the alginate network. Local chitosan patches on the surface may attract nearby alginate molecules, leading to the formation of pores or a more permeable surface, causing more interior adsorption sites to be accessible to the copper ions compared to the number available in plain alginate particles. Chitosan nanoparticles may spread when aggregating with oppositely charged alginate, also causing more adsorption sites on the chitosan to be accessible than in the case of free chitosan.

Adsorption of molybdenum

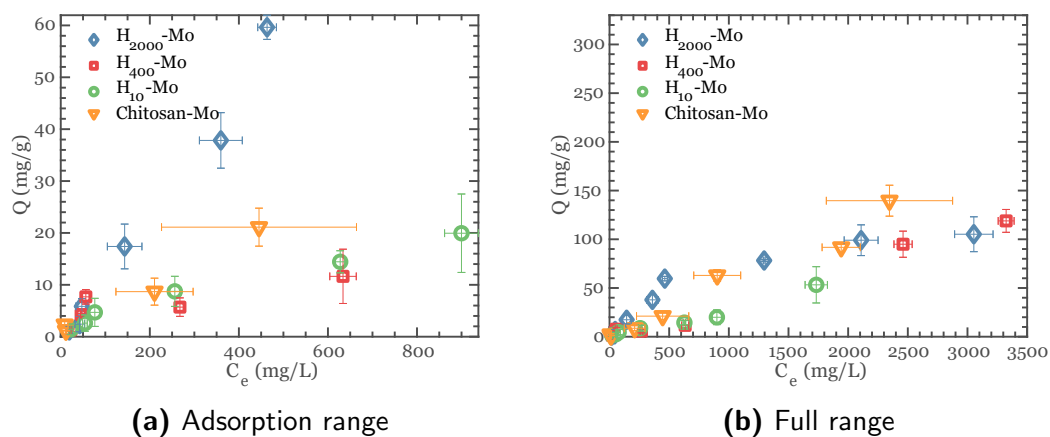


Figure 4.8: Adsorption of molybdenum on various adsorbents. *Chitosan-Mo* represents the adsorption of molybdenum on chitosan. *H*₁₀-*Mo*, *H*₄₀₀-*Mo* and *H*₂₀₀₀-*Mo* respectively represent the adsorption of molybdenum on heteroaggregates with 10, 400 and 2000 μ l of chitosan.

The adsorption of molybdenum ions on various adsorbents is shown in Figure 4.8. Negatively charged alginate did not adsorb a detectable amount of negative molybdate ions. Therefore, adsorption of molybdenum on alginate is not shown in the figure. In contrast to chitosan complexation with divalent metal ions, complexation of negative ions with alginate has not been reported and is not expected due to the absence of nitrogen functional groups in alginate. Accordingly, opposite charge attraction is the only adsorption mechanism expected for molybdate

ions. It can be seen that as the fraction of chitosan in the adsorbent increases, the amount of molybdenum adsorbed increases. This observation is consistent with the hypothesis that the negatively charged molybdate ion attaches to the positively charged amine groups of chitosan. However, heteroaggregates with 400 μl of chitosan seem to have a lower adsorption capacity than the heteroaggregates with 10 μl of chitosan, possibly because of diffusion limitations or presence of inaccessible sites in case of the former, due to multiple ‘monoaggregates’ agglomerating together. Moreover, unlike the adsorption enhancement observed in copper adsorption, all of the heteroaggregates do not have a higher adsorption capacity for molybdate than individual adsorbents (chitosan in this case) do. It is possible that the like charge repulsion of alginate and molybdate competes with the opposite charge attraction of chitosan and molybdate until the ions are adjacent to the chitosan, resulting in lower adsorption capacity for heteroaggregates than for free chitosan.

Adsorption of mixed molybdenum and copper ions

The adsorption of copper and molybdenum ions from a mixture of the same are shown in Figures 4.9 and 4.10 respectively.

It can be seen in Figure 4.9 that the adsorption capacities of the heteroaggregates are higher than those of the individual adsorbents. The individual adsorbents alginate and chitosan adsorb comparable amounts of copper ions from the mixture. Among the heteroaggregates, the ones in the ‘agglomerated’ regime (400 μl chitosan) seem to have the lowest adsorption capacity. This is probably due to the fact that the heteroaggregates in the ‘agglomerated’ regime have some adsorption sites obstructed or inaccessible compared to ‘dispersed, uncoated’ (10 μl chitosan) and ‘dispersed, coated’ (2000 μl chitosan) regimes. It can also be seen that as the equilibrium concentration increases, after a certain point, the adsorption capacity instead of reaching saturation starts to increase sharply again.

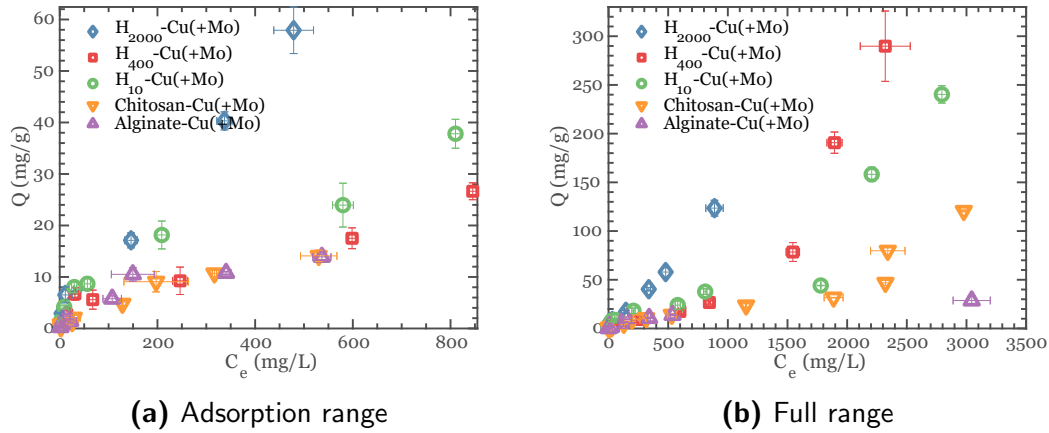


Figure 4.9: Adsorption of copper from a mixture of copper and molybdenum ions on various adsorbents. *Chitosan-Cu(+Mo)* and *Alginate-Cu(+Mo)* represent the adsorption of copper on chitosan and alginate respectively. *H₁₀-Cu(+Mo)*, *H₄₀₀-Cu(+Mo)* and *H₂₀₀₀-Cu(+Mo)* respectively represent the adsorption of copper on heteroaggregates with 10, 400 and 2000 μ l of chitosan.

The sharp increase, or inflection point, likely happens due to the transition of the system from the adsorption to the precipitation regime. The most likely explanation would be the precipitation of the positive copper ion and negative molybdate ion together as a salt. The fact that signs of precipitation in the adsorption curve were observed only in the case of mixed ion adsorption where the concentration of ions is twice the amount of ions in the single ion adsorption supports this explanation. Moreover, precipitation in the mixed solutions was observed visually where the starting ion solution concentration was higher than 2000 mg/L, but not in the single ion solutions. The sharp increase in the curve occurs at the lowest equilibrium concentration for the 2000 μ l heteroaggregate, followed by the 400 μ l heteroaggregate, the 10 μ l heteroaggregate, and chitosan, and is not observed at all for alginate over the concentration range studied.

As in Figure 4.9, the sharp changes in slope are seen in the curves of Figure 4.10, at the lowest equilibrium concentration for the 2000 μ l heteroaggregate, followed by the 400 μ l heteroaggregate, chitosan, the 10 μ l heteroaggregate, and are not observed at all for alginate particles. The reasons are believed to be

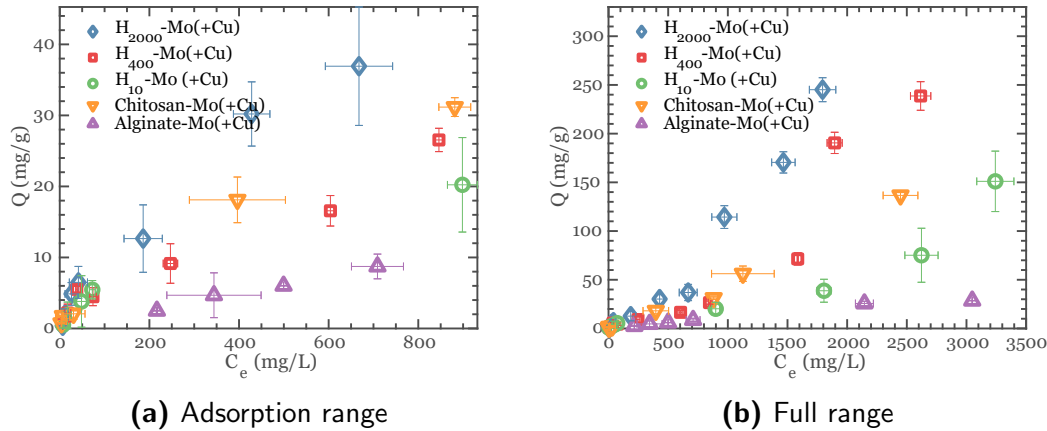


Figure 4.10: Adsorption of molybdenum from a mixture of copper and molybdenum ions on various adsorbents. *Chitosan-Mo(+Cu)* and *Alginate-Mo(+Cu)* represent the adsorption of molybdenum on chitosan and alginate respectively. H_{10} -Mo(+Cu), H_{400} -Mo(+Cu) and H_{2000} -Mo(+Cu) respectively represent the adsorption of molybdenum on heteroaggregates with 10, 400 and 2000 μ l of chitosan.

similar to the ones described above. Unlike copper adsorption, however, in the case of molybdate adsorption from a mixed ion system, the heteroaggregates do not show a clear advantage over the individual adsorbents. Similar to the adsorption of molybdate from a single ion solution (Figure 4.8), the chitosan has a higher adsorption capacity than the heteroaggregates with 10 and 400 μ l of chitosan, and comparable adsorption to that of the heteroaggregates with 2000 μ l of chitosan. Heteroaggregates with 2000 μ l of chitosan seem to have the highest adsorption capacity for both molybdate and copper from a mixture.

4.3.2.2 Comparison between solutes

In this section, the equilibrium adsorption capacity of each adsorbent for the adsorption of various solutes such as molybdate and copper ions from single ion and mixed ion solutions has been compared in order to understand the effect of the presence of oppositely charged ions in the system.

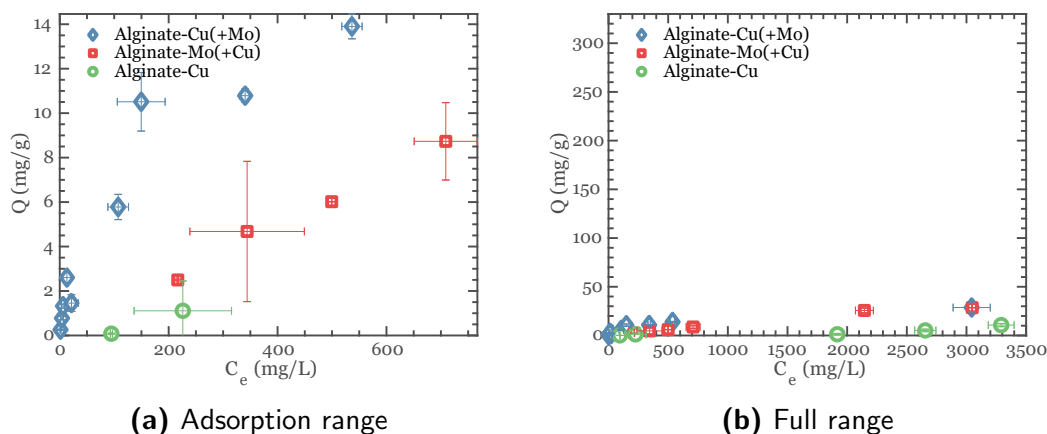


Figure 4.11: Adsorption of various solutes on alginate. *Alginates-Cu(+Mo)* and *Alginates-Mo(+Cu)* respectively represent the adsorption of copper and molybdenum from a mixture of the same on alginate. *Alginates-Cu* represents the adsorption of copper on alginate.

Adsorption on alginate

The adsorption capacity of alginate for the adsorption of copper ion from a copper sulfate solution, copper and molybdate ions from a mixture of copper sulfate and ammonium molybdate is shown in Figure 4.11. As mentioned before, adsorption of molybdate from the single ion solution is not shown in the figure because there was no detectable adsorption. In contrast, alginate was able to adsorb molybdate from the mixed ion solution. It can be seen that the adsorption capacity of alginate for both ions is much higher for mixed ion systems. This enhanced adsorption probably happens because of complexation in the case of mixed ions, where the positive copper ions adsorbed on the alginate beads interact with the negative molybdate ions in the solution and form a complex. Another possibility is that positive copper ions adsorb on to the alginate first and form a layer that neutralizes some of the alginate negative charge and thereby reduces the repulsion of molybdate ions. Molybdate ions may then form a layer on top of the copper ions and then promote enhanced adsorption of copper from the mixture as well. Because the copper ion is of the opposing surface charge of alginate, more copper

is adsorbed as compared to molybdate in case of mixed ions. In addition, the smaller size of the copper ions may allow more adsorption sites to be accessible to copper ions than to the larger molybdate ions.

Adsorption on chitosan

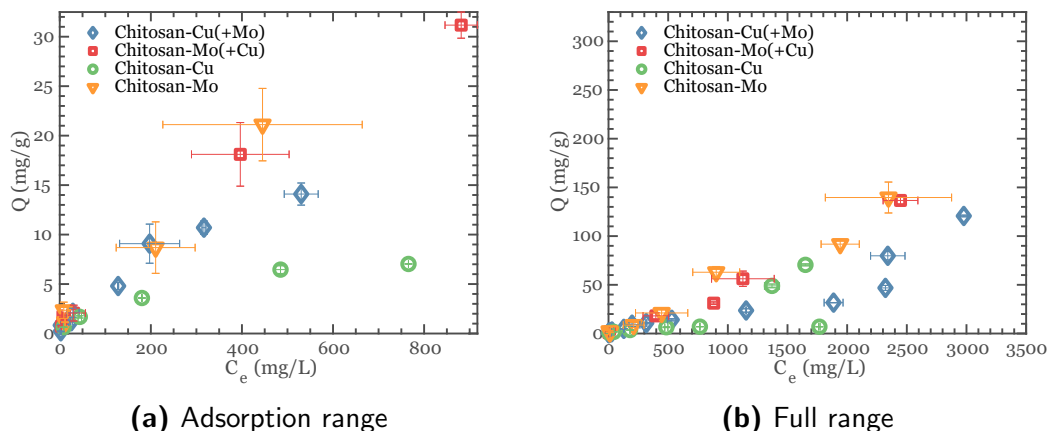


Figure 4.12: Adsorption of various solutes on chitosan. *Chitosan-Cu(+Mo)* and *Chitosan-Mo(+Cu)* respectively represent the adsorption of copper and molybdenum from a mixture on chitosan. *Chitosan-Cu* and *Chitosan-Mo* respectively represent the adsorption of copper and molybdenum on chitosan from single ion solutions.

In Figure 4.12, the equilibrium adsorption behavior of chitosan for molybdate and copper ions from both single ion systems and mixed ion systems is shown. It can be seen that the adsorption capacity is higher for molybdate ions compared to copper ions for both cases. This observation suggests that opposite charge attraction is a more effective adsorption mechanism than complexation. Comparing the mixed ion to single ion systems, the adsorption of molybdate ions was almost identical in both cases. At dilute concentrations where the data are most accurate, the adsorption of copper ions was greater in the mixed solution than in the single ion solution. Perhaps the molybdate is preferentially adsorbed through opposite charge attraction by the chitosan and then provides additional opportunities for copper ions to adsorb through complexation between the two metal ions, layer-by-layer adsorption of oppositely charged metal ions, or opening of pores in

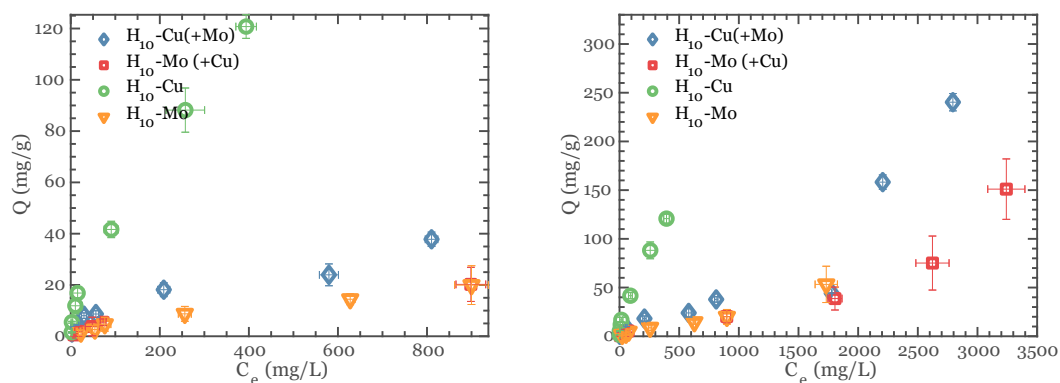
the chitosan to expose additional interior adsorption sites on the chitosan, similar to the hypothesized adsorption behavior on alginate.

Adsorption on heteroaggregates

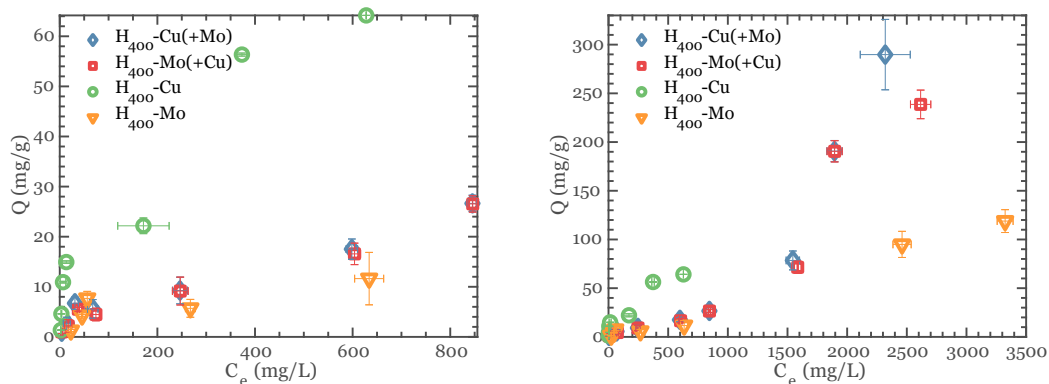
The adsorption of various solutes on the heteroaggregates from the three different regimes is presented in Figure 4.13. For all of the heteroaggregates, the adsorption capacity for copper ions alone is higher than that for molybdate ions alone, with the greatest difference seen in heteroaggregates with 10 μl of chitosan. Also, the amount of copper adsorbed from a mixed solution is greater than or equal to the amount of molybdate adsorbed from a mixed solution. It can be seen that the adsorption behavior is similar for heteroaggregates with 10 and 400 μl of chitosan but slightly different behavior can be seen for heteroaggregates with 2000 μl of chitosan. This is expected since the amount of chitosan is very dissimilar in the latter from the other two. In the case of heteroaggregates with 10 and 400 μl of chitosan, it can be seen that the adsorption capacity is much higher for adsorption of copper from single ion as well as mixed ion solutions compared to molybdate. This finding can be attributed to the higher alginate-to-chitosan ratio in heteroaggregates in these regimes. In the case of heteroaggregates with 2000 μl of chitosan, the difference between copper adsorption from a single and mixed ion solution is less compared to that of the heteroaggregates with 10 and 400 μl of chitosan. Also, the adsorption of molybdate is very similar in the mixed ion and single ion solutions for heteroaggregates with 10 and 400 μl of chitosan, while the molybdate adsorption is less for the mixed ion solution than the single ion solution for heteroaggregates with 2000 μl of chitosan. These results could be due to the presence of a much higher chitosan fraction in the heteroaggregates with 2000 μl of chitosan. In addition, it is possible that there are free chitosan molecules remaining on the surface of the chitosan nanoparticles which agglomerate with negative molybdate ions, resulting in an increase in the ‘adsorption’ of molybdate.

Comparing the three types of heteroaggregates over the full concentration range (b,d,f), it appears that a sharp increase in the slope of the adsorption curve, likely indicating precipitation, occurs at a lower equilibrium concentration as the chitosan fraction in the heteroaggregate increases. This observation suggests that the presence of chitosan promotes precipitation, possibly by bringing the oppositely charged metal ions into close proximity as they are nearing adsorption on the chitosan. Another notable point is the lower copper ion adsorption in mixed ion compared to single ion solutions, particularly for heteroaggregates with 10 μ l of chitosan, while molybdate adsorption is unchanged or slightly lower in mixed ion solutions. The lower copper ion adsorption in a mixture is the opposite of what is observed in the individual components. The data suggest the molybdate ions interfere with the enhancement of copper ion adsorption observed in the heteroaggregates, perhaps by decreasing the mobility of the alginate and chitosan networks due to adsorption or charge effects.

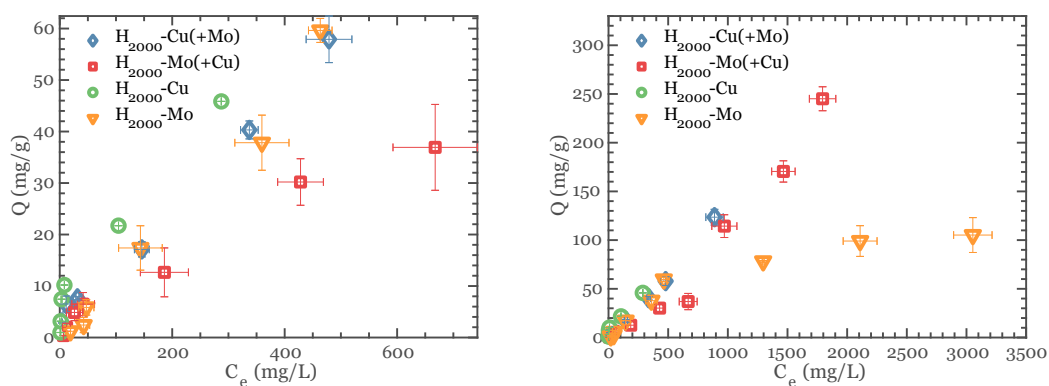
In mixed ion solutions, all of the heteroaggregates are able to achieve a capacity of approximately 40-50 mg/g (based on the wet mass) adsorption of either ion, before significant precipitation occurs. Considering that the adsorbents are hydrogels and consist of more than 90% water, the adsorption capacity based on the dry mass adsorbent is at least a factor of 10 greater than the observed amount and therefore quite promising. Based on the Langmuir coefficients indicating the maximum adsorption capacity in Table 1, the optimal choice of adsorbent would probably be a combination of the heteroaggregates with 10 μ l and with 2000 μ l of chitosan.



(a) Adsorption range for heteroaggregates with 10 µl of chitosan (b) Full range for heteroaggregates with 10 µl of chitosan



(c) Adsorption range for heteroaggregates with 400 µl of chitosan (d) Full range for heteroaggregates with 400 µl of chitosan



(e) Adsorption range for heteroaggregates with 2000 µl of chitosan (f) Full range for heteroaggregates with 2000 µl of chitosan

Figure 4.13: Adsorption of various solutes on heteroaggregates from three different regimes. H_{-} -Cu(+Mo) and H_{-} -Mo(+Cu) respectively represent the adsorption of copper and molybdenum from a mixture on the heteroaggregates. H_{-} -Mo and H_{-} -Cu respectively represent the adsorption of molybdenum and copper on the heteroaggregates.

Table 4.1: Coefficient of determination and model constants for Langmuir and Freundlich isotherms

Adsorbent	Adsorbate	R^2	Langmuir		R^2	Freundlich	
			Q_{\max} (mg/g)	K_s (L/mg)		K_F $(\frac{mg}{g})(\frac{mg}{L})^{-1/n}$	$1/n$
Alginate	Cu	1	1.2548	0.0340	-	-	-
Alginate	Cu(+Mo)	0.9551	30.9396	0.00302	0.9497	0.6334	0.5902
Alginate	Mo(+Cu)	0.7513	110.0027	1.2×10^{-4}	0.9901	0.1797	0.9255
Chitosan	Cu	0.9936	7.5967	0.0080	0.9587	0.5596	0.4815
Chitosan	Mo	0.2024	210.732	3.6496×10^{-4}	0.9494	0.5304	0.7856
Chitosan	Cu(+Mo)	0.9253	44.4012	0.0011	0.9499	0.5299	0.6520
Chitosan	Mo(+Cu)	0.9881	63.8913	0.0011	0.9678	0.6034	0.6677
H_{10}	Cu	0.8587	153.9457	0.0065	0.9437	1.3044	0.7094
H_{10}	Mo	0.93	28.4576	0.0021	0.9825	0.4759	0.6927
H_{10}	Cu(+Mo)	0.93802	46.8200	0.0046	0.9772	1.0745	0.4995
H_{10}	Mo(+Cu)	0.9859	26.8345	0.0034	0.9468	0.4926	0.7166
H_{400}	Cu	0.8138	69.2450	0.0095	0.8518	1.3921	0.5369
H_{400}	Mo	0.7466	13.3518	0.0061	-	-	-
H_{400}	Cu(+Mo)	0.8893	19.1086	0.0086	0.9388	0.8138	0.5383
H_{400}	Mo(+Cu)	0.8846	19.2979	0.0065	0.9642	0.7091	0.5770
H_{2000}	Cu	0.8749	48.5419	0.0217	0.8510	1.3781	0.5560
H_{2000}	Mo	0.9823	139.2400	0.0011	0.9327	0.4257	0.8876
H_{2000}	Cu(+Mo)	0.6554	71.1779	0.0047	0.9624	1.1285	0.5757
H_{2000}	Mo(+Cu)	0.3847	74.1708	0.0015	0.9125	0.4676	0.8562

4.4 Chapter conclusions

In this work, the equilibrium adsorption capacity of novel structured particulates (heteroaggregates) made up of environmentally benign biopolymers alginate and chitosan, popularly used as adsorbents for wastewater purification individually, has been investigated. The adsorption capacity of the heteroaggregates has been compared with that of its components to explore the possibility of using these heteroaggregates instead of their individual components. Moreover, the adsorbents have been tested for the adsorption from mixed ion solutions which represent real wastewater more accurately than the commonly studied single ion systems.

It was observed that for adsorption of copper ions, both from single ion and mixed ion systems, the heteroaggregates from all three regimes showed enhanced equilibrium adsorption capacity. For adsorption of copper from a single ion system, heteroaggregates with 10 μl of chitosan showed much higher adsorption capacity than the other heteroaggregates, possibly due to the fact that these heteroaggregates have the highest alginate-to-chitosan ratio.

For molybdate adsorption from both single and mixed ion systems, it was seen that as the quantity of chitosan in the adsorbent increases, the adsorption capacity increases. This finding can be attributed to the electrostatic attraction between negatively charged molybdate ions and positively charged chitosan particles. Unlike the copper adsorption behavior, however, chitosan individually seemed to have a higher adsorption capacity for molybdate than the heteroaggregates with 10 and 400 μl of chitosan, which is possibly due to the high surface area available with chitosan nanoparticles and the strong electrostatic attraction between positively charged chitosan nanoparticles and negatively charged molybdate ions. Alginate particles individually did not adsorb any detectable levels of molybdate ions as both are negatively charged entities.

Among the heteroaggregates, the structures with 400 μl of chitosan generally

showed the lowest equilibrium adsorption capacity. This effect is most likely due to either diffusion limitations or the presence of inaccessible sites to the ions or both, since, in this agglomerated regime, multiple ‘monoaggregates’ agglomerate to form large heteroaggregates.

In case of adsorption from mixed ion systems, a sharp change in the slope of the adsorption curve was observed in almost all of the experiments. Instead of the saturation of equilibrium adsorption capacity with increasing ion concentration, the equilibrium adsorption capacity seemed to continue to increase. This indicated the transition of the system from adsorption to precipitation regime. Due to an ion concentration that is twice of the ion concentration in single ion systems, oppositely charged copper and molybdate ions seemed more prone to aggregation with each other followed by precipitation.

From the comparison of the adsorption capacity of alginate and chitosan for different solutes, it was seen that the adsorption of each ion from mixed ion systems was greater than or equal to the adsorption from single ion systems. The increase in mixed solutions can be attributed to a complex formation where the first ‘layer’ of ions adsorbed on the adsorbent, for example, molybdate ions on chitosan and copper ions on alginate, form a complex with the oppositely charged ions, such as copper ions for chitosan and molybdate ions for alginate. Another expected trend was the greater adsorption of ions when they are oppositely charged with respect to the adsorbent, for example, molybdate ion adsorption on chitosan both from mixed and single ion systems is greater than copper adsorption on chitosan.

From the comparison of adsorption of different solutes on heteroaggregates, the overarching trend was greater or equal adsorption of copper compared to molybdate from single and mixed ion systems, which is likely due to both components alginate and chitosan exhibiting affinity for copper ions while only chitosan

shows affinity with molybdate. The heteroaggregates in all three regimes are alginate dominated, with a mass fraction of negatively charged alginate of greater than 0.5. Another observation was that the heteroaggregates with 10 and 400 μl of chitosan behaved quite similarly to each other, which was expected considering that the composition of the heteroaggregates of these two regimes is quite similar to each other compared to the heteroaggregates with 2000 μl of chitosan. Also, as expected, heteroaggregates with 2000 μl of chitosan adsorbed more molybdate than the other heteroaggregates, since there was more chitosan in these heteroaggregates and possibly some free chitosan as well in the solution to adsorb more molybdate. Moreover, it was observed that the adsorption of copper ions and of molybdate ions was the same or lower in the mixed ion solution than in the single ion solutions, suggesting the presence of competitive or blocking interactions between the ions. Finally, in mixed ion solutions, all of the heteroaggregates are able to achieve a capacity of approximately 40-50 mg/g (based on the wet mass) adsorption of either ion, before significant precipitation occurs, which indicates that they have great potential as sustainable, next generation adsorbents.

Chapter 5

Conclusions and future directions

5.1 Conclusions

In this work, firstly, a population balance model for the second stage or the agglomeration stage of the heteroaggregation process was developed. A parametric study was performed using the model to study the effect of various process parameters on the van der Waals, electrostatic, hydration and total interaction potential. It was seen that the magnitude of the electrostatic force was highest in case of two small, equal sized particles with a high surface potential ratio at close distance in contrast to the case between two large, dissimilar sized particles with low surface potential ratio that were very far from each other. In comparison, van der Waals and hydration forces were strongest at a close distance between two equal sized particles. Electrostatic force was seen to be the most dominant among all the forces. VDW force closely followed but the hydration force seemed negligible compared to these forces.

Both simulations and experiments were performed to investigate the effect of initial alginate and chitosan concentration on the final particles size distribution and composition. It was observed that the system progressed towards different regimes based on the initial relative amount of alginate and chitosan. For systems with small amount of chitosan compared to alginate, 'monoaggregates' with very little chitosan layered on top was formed initially. These negatively charged 'monoaggregates' repelled each other and did not agglomerate. This was termed the 'dispersed, uncoated' regime. For a very high chitosan amount compared

to the alginate, positively charged ‘monoaggregates’ were formed which repelled each other. This regime was called the ‘dispersed, coated’ due to the ‘monoaggregates’ being well coated with chitosan but not aggregating. Agglomeration was seen when the chitosan amount was just enough to neutralize the negative surface charge of majority of alginate particles. These resulted in neutral monoaggregates which aggregated with each other to form larger heteroaggregates. This was named the ‘agglomerated’ regime.

In different application areas of heteroaggregates, different size and composition criteria have to be maintained. In this work, a qualitative relation between the initial alginate-chitosan relative concentration and the final heteroaggregate size and composition was established. This knowledge can therefore be applied to design and produce heteroaggregates suited to different applications.

In the next step, a separate model for the first stage or the layering stage of the heteroaggregation process was developed and validated by comparing with the trends seen in the final heteroaggregate PSD.

It was seen that at no surface coverage, the monoaggregate had a surface potential equal to that of an alginate particle. With increasing surface coverage the surface potential increased. At maximum allowed surface coverage in the model, the monoaggregate surface potential reached the surface potential of chitosan particles.

A zeta potential within ± 30 mV is considered to lead to unstable suspensions where particles do not repel each other enough to overcome the attractive van der Waals force which leads to agglomeration. It was seen that monoaggregates with about 20% surface area coverage were neutral and monoaggregates within 6-32% surface area coverage were likely to agglomerate with each other.

The relation of the number distribution of monoaggregates with the percentage surface coverage and the surface potential of the monoaggregates was also

investigated. As expected, with more chitosan in the system, the number distribution shifted to the right which meant that the number of monoaggregates with higher surface coverage and higher surface potential increased. For 0.1 g of alginate and 10, 1200 and 2400 μl of chitosan, most or all monoaggregates had a surface potential that was in the stable region and therefore large heteroaggregate formation was less compared to 200, 400 and 800 μl of chitosan cases where most monoaggregates were in the unstable region which lead to the formation of large heteroaggregates. The model findings were validated by comparing with experimental heteroaggregate PSDs, which matched with the layering model results. In case of 0.2 g alginate, both model and experimental results showed that for 10 and 200 μl of chitosan the system progressed towards 'dispersed, uncoated' regime. Addition of 400 and 800 μl of chitosan lead to 'agglomerated regime' and 1200, 2400 μl of chitosan lead to 'dispersed, coated' regime.

The layering of chitosan on alginate beads was also studied using SEM analysis. The samples had to be dried before the SEM analysis which led to shrinkage of the alginate beads and chitosan nanoparticles. This reduced the visibility of chitosan layers on the surface of alginate beads. However, with increasing chitosan amount in the system, a slight increase in chitosan layering was observed. The overall low surface coverage observed in the SEM images agreed with the low surface coverage observed with the layering model, which was probably more pronounced due to the shrinking of particles. The chitosan layer was also found to be non-uniform and patchy which was in line with what has been found by other researchers.

After that, the layering model framework was integrated in the agglomeration model developed in Chapter 2. Although, the combined agglomeration-layering model was able to capture the general trend of the system transition from one regime to another without any assumption about the initial monoaggregate distribution, a over-prediction of the layering was observed.

Lastly, the equilibrium adsorption capacity of the heteroaggregates for the adsorption of heavy metal ions from wastewater was studied. The components of the heteroaggregates used in this study being good adsorbents of heavy metals individually made it likely for the heteroaggregates to be good adsorbents of heavy metals as well. With the added benefit of having oppositely charged components in the heteroaggregates facilitating the adsorption of oppositely charged heavy metal ions from the wastewater which is otherwise not possible by having just one of the adsorption components in the system, the heteroaggregates have potential to be a better alternative to individual adsorbents. Moreover, the components being environment friendly biopolymer particles makes these heteroaggregates an attractive option as an adsorbent of heavy metal ions from wastewater. The adsorption capacities of the heteroaggregates were compared with the adsorption characteristics of the individual components to verify this hypothesis. In addition, the adsorption characteristics of the adsorbents were compared for the adsorption from mixed ion systems as well as single ion systems. This was included in the study because the mixed ion solutions represented real wastewater more accurately than the commonly studied single ion systems.

The heteroaggregates showed a much better adsorption than the individual adsorbents in case of copper ion adsorption. Among the heteroaggregates, the one with 10 μl of chitosan had the highest adsorption capacity, likely due to the highest alginate-to-chitosan ratio in the adsorbent.

For adsorption of molybdenum, the adsorption capacity increased with increasing chitosan amount in the adsorbent. This was probably due to the electrostatic attraction between the positively charged component of the adsorbents, chitosan and negatively charged molybdenum ions. Individual alginate particles did not adsorb detectable amount of molybdenum probably due to the similar surface charge of both.

The biggest heteroaggregates, the ones with 400 μl of chitosan adsorbed the

least amount, likely due to either diffusion limitations causing some adsorption sites inside the hydrogel to be less accessible to the ions.

For the adsorption of various ions on alginate and chitosan, it was observed that the adsorption was higher when the adsorbent-ion combination was oppositely charged, for example, adsorption of copper on alginate and molybdenum on chitosan was higher than the other combinations.

For the adsorption of different adsorbates on heteroaggregates, the adsorption of copper was more than the adsorption of molybdenum; both for single and mixed ion systems. This can be attributed to the smaller size of copper ions compared to the molybdenum oxoanion which possibly allowed more adsorption sites inside the hydrogel structure to be accessible to the copper ion but not the molybdenum ion. It could also be possible that the presence of a higher quantity of negatively charged alginate in the heteroaggregates helped in the adsorption of positively charged copper. Possibly for a similar reason, heteroaggregates with 2000 μl of chitosan adsorbed more molybdenum compared to the other heteroaggregates. It is also possible that there was some free chitosan in this case which might have precipitated with the molybdenum ions. The heteroaggregates with 10 and 400 μl of chitosan did not show much difference in terms of adsorption characteristics, probably because the composition of the heteroaggregates were not much different from each other even though structurally they were different.

5.2 Future directions

This work can be extended to study and predict the particle size evolution of heteroaggregates in real systems such as an adsorption column packed with particles that are very different in terms of size and charge such as the alginate microparticles and the chitosan nanoparticles studied in this system for wastewater purification by coupling the PBM with discrete element models (DEM) and

computational fluid dynamics (CFD), if necessary. The over-prediction of layering by the combined agglomeration-layering model indicated the need for a more detailed DEM model or even more accurate molecular dynamics simulations for simulating the layering stage. More detailed imaging of the monoaggregates and heteroaggregates would give a better idea of the structure and layering. It would be especially useful to use a imaging method such as cryo-SEM where the structure of the monoaggregates could be conserved during imaging. This would also allow for imaging of heteroaggregates which is otherwise impossible. It would be useful to develop a microscale model for the layering stage and use those images for validation of the model.

Elemental analysis of the heteroaggregates and monoaggregates would also give a better idea about the composition of the aggregates which is another criterion that is very crucial in various application of heteroaggregates.

Acknowledgement of previous publications

Journal publication

Publications in support of this thesis

1. **A. Chaturbedi**, C. Pathak, K. Deshpande, N. Shapley, R. Ramachandran. Population balance model development and experimental validation for the heteroaggregation of oppositely charged micro- and nano-particles. *Chemical Engineering Research & Design*, 113, 96-111, 2016
2. **A. Chaturbedi**, S. Patil, R. Ramachandran, N. Shapley. Adsorption of positively and negatively charged heavy metal ions from wastewater by heteroaggregates of biopolymer particles. *Submitted to Colloids and Surfaces A: Physicochemical and Engineering Aspects*
3. **A. Chaturbedi**, R. Ramachandran, N. Shapley. Modeling and experimental study of layering of positively charged nanoparticles on negatively charged microparticles. *In preparation*

Other publications

1. **A. Chaturbedi**, C. Bandi, D. Reddy, P. Pandey, A. Narang, D. Bindra, L. Tao, J. Zhao, J. Li, M. Hussain, R. Ramachandran. Compartment based population balance model development and validation of a high shear wet granulation process via dry binder addition. *Chemical Engineering Research & Design*, 123, 187-200, 2017
2. **A. Chaturbedi**, P. Pandey, D. Bindra, J. P. Reddy, B. Lang, D. Buckley, R. Ramachandran. Predictive population balance model development and

- validation of the effect of high shear wet granulation process parameters on granule properties. *Powder Technology*, 338, 391-401, 2018
3. F. Bettencourt, **A. Chaturbedi**, R. Ramachandran. Parallelization methods for efficient simulation of high dimensional population balance models of granulation. *Computers & Chemical Engineering*, 107, 158-170, 2017
 4. C. Sampat, F. Bettencourt, Y. Baranwal, I. Paraskevagos, **A. Chaturbedi**, S. Karkala, S. Jha, R. Ramachandran, M. Ierapetritou. A parallel unidirectional coupled DEM-PBM model for the efficient solution and simulation of computationally intensive systems. *Computers & Chemical Engineering*, 119, 128-142, 2018
 5. **A. Chaturbedi**, J. P. Reddy, P. Pandey, D. Bindra, B. Lang, D. Buckley, R. Ramachandran. Predictive population balance model development and validation of the effect of high shear wet granulation formulation on granule properties. *In preparation*
 6. **A. Chaturbedi**, I. Muthancheri, A. Betard, R. Ramachandran. Development and validation of multi-dimensional, compartment-based population balance model for high shear wet granulation processes. *In preparation*
 7. K. Yu, **A. Chaturbedi**, B. Schendt, N. Shapley. Rheology of a concentrated bimodal suspension containing rigid and soft particles. *In preparation*

Conference presentations

1. **A. Chaturbedi**, N. Shapley, R. Ramachandran, Development of Population Balance Model and Semi-Mechanistic Layering Kernel for Two-Stage Heteroaggregation of Oppositely Charged Micro- and Nano-Particles, AIChE Annual Meeting 2016, San Francisco, USA, November 2016

2. **A. Chaturbedi**, F. Bettencourt, S. Mushnoori, S. Karkala, S. Jha, M. Ierapetritou, R. Ramachandran, Cyberinfrastructure-Enabled Parallelization of Population Balance Models for Efficient Simulation of Granulation Processes, AIChE Annual Meeting 2016, San Francisco, USA, November 2016
3. F. Bettencourt, **A. Chaturbedi**, R. Ramachandran, Parallelization of Population Balance Models for Real Time Control of Particulate Processes, International Symposium on Design, Operation and Control of Chemical Processes PSE Asia 2016, Tokyo, Japan, July 2016
4. F. Bettencourt, **A. Chaturbedi**, R. Ramachandran, Hybrid Parallelization Algorithms to Accelerate Population Balance Modeling for Wet Granulation, AIChE Mid-Atlantic Student Regional Conference, University of Delaware, USA, April 2016
5. F. Bettencourt, **A. Chaturbedi**, R. Ramachandran, Hybrid parallelization of Population Balance Models for Massively Accelerated Modeling of particulate Processes, AIChE Annual Meeting, Salt Lake City, USA, November 2015
6. N. C. Shapley, **A. Chaturbedi**, B. Schendt. Relative viscosity trends of bimodal suspensions containing rigid and soft particles, 87th Annual Society of Rheology Meeting, Baltimore, USA, October 2015
7. N. C. Shapley, O. Isijola, **A. Chaturbedi**. Rheology of a bimodal suspension containing rigid and soft particles, 86th Annual Society of Rheology Meeting, Philadelphia, USA, October 2014

Bibliography

- Afkhami, A., Madrakian, T., and Amini, A. (2009). Mo(VI) and W(VI) removal from water samples by acid-treated high area carbon cloth. *Desalination*, 243(1):258 – 264.
- Afkhami, A. and Norooz-Asl, R. (2009). Removal, preconcentration and determination of Mo(VI) from water and wastewater samples using maghemite nanoparticles. *Colloids and Surfaces A: Physicochemical and Engineering Aspects*, 346(13):52 – 57.
- Ahuja, S., Lai, Z., and Cheng, C. (2007). Toner composition and methods. US Patent App. 11/368,830.
- Akar, S. T., Akar, T., Kaynak, Z., Anilan, B., Cabuk, A., zge Tabak, Demir, T. A., and Gedikbey, T. (2009). Removal of copper(II) ions from synthetic solution and real wastewater by the combined action of dried trametes versicolor cells and montmorillonite. *Hydrometallurgy*, 97(12):98 – 104.
- Akpor, O., Ohiobor, G., and Olaolu, T. (2014). Heavy metal pollutants in wastewater effluents: sources, effects and remediation. *Advances in Bioscience and Bioengineering*, 2(4):37–43.
- Atmuri, A. K., Henson, M. A., and Bhatia, S. R. (2013). A population balance equation model to predict regimes of controlled nanoparticle aggregation. *Colloids and Surfaces A: Physicochemical and Engineering Aspects*, 436:325 – 332.

- Axford, S. D. T. (1997). Aggregation of colloidal silica: Reaction-limited kernel, stability ratio and distribution moments. *J. Chem. Soc., Faraday Trans.*, 93:303–311.
- Barakat, M. (2011). New trends in removing heavy metals from industrial wastewater. *Arabian Journal of Chemistry*, 4(4):361 – 377.
- Barrasso, D., Hagrasy, A. E., Litster, J. D., and Ramachandran, R. (2015). Multi-dimensional population balance model development and validation for a twin screw granulation process. *Powder Technology*, 270, Part B:612 – 621.
- Barrasso, D. and Ramachandran, R. (2015). Multi-scale modeling of granulation processes: Bi-directional coupling of PBM with DEM via collision frequencies. *Chemical Engineering Research and Design*, 93:304 – 317.
- Babler, M. U., Moussa, A. S., Soos, M., and Morbidelli, M. (2010). Structure and kinetics of shear aggregation in turbulent flows. I. early stage of aggregation. *Langmuir*, 26(16):13142–13152.
- Boddu, V. M., Abburi, K., Talbott, J. L., and Smith, E. D. (2003). Removal of hexavalent chromium from wastewater using a new composite chitosan biosorbent. *Environmental Science & Technology*, 37(19):4449–4456.
- Bodmeier, R. and Paeratakul, O. (1989). Spherical agglomerates of water-insoluble drugs. *Journal of Pharmaceutical Sciences*, 78(11):964–967.
- Bostick, B. C., Fendorf, S., and Helz, G. R. (2003). Differential adsorption of molybdate and tetrathiomolybdate on pyrite (FeS_2). *Environmental Science & Technology*, 37(2):285–291.
- Braccini, I. and Perez, S. (2001). Molecular basis of Ca^{2+} induced gelation in alginates and pectins the egg-box model revisited. *Biomacromolecules*, 2(4):1089–1096.

- Cerbelaud, M., Videcoq, A., Abelard, P., and Ferrando, R. (2009). Simulation of the heteroagglomeration between highly size-asymmetric ceramic particles. *Journal of Colloid and Interface Science*, 332(2):360 – 365.
- Cerbelaud, M., Videcoq, A., Abelard, P., Pagnoux, C., Rossignol, F., and Ferrando, R. (2008). Heteroaggregation between Al_2O_3 submicrometer particles and SiO_2 nanoparticles: experiment and simulation. *Langmuir*, 24(7):3001–3008.
- Cerbelaud, M., Videcoq, A., Abelard, P., Pagnoux, C., Rossignol, F., and Ferrando, R. (2010). Self-assembly of oppositely charged particles in dilute ceramic suspensions: predictive role of simulations. *Soft Matter*, 6:370–382.
- Chaturvedi, A., Pathak, C., Deshpande, K., Shapley, N., and Ramachandran, R. (2016). Population balance model development and experimental validation for the heteroaggregation of oppositely charged micro- and nano-particles. *Chemical Engineering Research and Design*, 113:96 – 111.
- Chaudhury, A., Armenante, M. E., and Ramachandran, R. (2015). Compartment based population balance modeling of a high shear wet granulation process using data analytics. *Chemical Engineering Research and Design*, 95:211 – 228.
- Chaudhury, A., Barrasso, D., Pandey, P., Wu, H., and Ramachandran, R. (2014). Population balance model development, validation, and prediction of CQAs of a high-shear wet granulation process: Towards QbD in drug product pharmaceutical manufacturing. *Journal of Pharmaceutical Innovation*, 9:53–64.
- Chaudhury, A., Kapadia, A., Prakash, A. V., Barrasso, D., and Ramachandran, R. (2013). An extended cell-average technique for a multi-dimensional population balance of granulation describing aggregation and breakage. *Advanced Powder Technology*, 24(6):962 – 971.
- Derjaguin, B. (1934). Untersuchungen ber die reibung und adhsion, IV. *Kolloid-Zeitschrift*, 69(2):155–164.

- Derjaguin, B. and Landau, L. (1993). Theory of the stability of strongly charged lyophobic sols and of the adhesion of strongly charged particles in solutions of electrolytes. *Progress in Surface Science*, 43(1):155–164.
- Deshpande, K. V. (2014). *Particulate Flows and Heteroaggregation Studied by Optical Imaging and Fluorescence Spectroscopy*. PhD thesis, Rutgers, The State University of New Jersey.
- Donati, I., Holtan, S., Morch, Y. A., Borgogna, M., and Dentini, M. (2005). New hypothesis on the role of alternating sequences in calcium-alginate gels. *Biomacromolecules*, 6(2):1031–1040.
- Elimelech, M., Gregory, J., Jia, X., and R.A., W. (1995). *Particle Deposition and Aggregation - Measurement, Modelling and Simulation*. Elsevier.
- Elwakeel, K. Z., Atia, A. A., and Donia, A. M. (2009). Removal of Mo(VI) as oxoanions from aqueous solutions using chemically modified magnetic chitosan resins. *Hydrometallurgy*, 97(12):21 – 28.
- Emmerichs, N., Wingender, J., Flemming, H.-C., and Mayer, C. (2004). Interaction between alginates and manganese cations: identification of preferred cation binding sites. *International Journal of Biological Macromolecules*, 34(1):73 – 79.
- Evans, J. R., Davids, W. G., MacRae, J. D., and Amirbahman, A. (2002). Kinetics of cadmium uptake by chitosan-based crab shells. *Water Research*, 36(13):3219 – 3226.
- Fisher, M. L., Colic, M., Rao, M. P., and Lange, F. F. (2001). Effect of silica nanoparticle size on the stability of alumina/silica suspensions. *Journal of the American Ceramic Society*, 84(4):713–718.

- Freundlich, H. (1906). Over the adsorption in solution. *J. Phys. Chem*, 57(385471):1100–1107.
- Fuchs, N. Z. (1934). Ueber die stabilitat und aufladung der aerosole. *Zeitschrift fur Physik*, 89:736–743.
- Furusawa, K. and Velev, O. D. (1999). Electrokinetic behavior in synthetic process of composite particles. *Colloids and Surfaces A: Physicochemical and Engineering Aspects*, 159(2):359–371.
- Gerente, C., Andres, Y., and Cloirec, P. L. (1999). Uranium removal onto chitosan: Competition with organic substances. *Environmental Technology*, 20(5):515–521.
- Gilchrist, J. F., Chan, A. T., Weeks, E. R., and Lewis, J. A. (2005). Phase behavior and 3D structure of strongly attractive microspherenanoparticle mixtures. *Langmuir*, 21(24):11040–11047.
- Gonzalez-Davila, M., Santana-Casiano, J., and Millero, F. J. (1990). The adsorption of Cd(II) and Pb(II) to chitin in seawater. *Journal of Colloid and Interface Science*, 137(1):102 – 110.
- Gotoh, T., Matsushima, K., and Kikuchi, K.-I. (2004). Preparation of alginate-chitosan hybrid gel beads and adsorption of divalent metal ions. *Chemosphere*, 55(1):135 – 140.
- Guibal, E. (2004). Interactions of metal ions with chitosan-based sorbents: a review. *Separation and Purification Technology*, 38(1):43 – 74.
- Guibal, E., Dambies, L., Milot, C., and Roussy, J. (1999a). Influence of polymer structural parameters and experimental conditions on metal anion sorption by chitosan. *Polymer International*, 48(8):671–680.

- Guibal, E., Milot, C., Eterradosi, O., Gauffier, C., and Domard, A. (1999b). Study of molybdate ion sorption on chitosan gel beads by different spectrometric analyses. *International Journal of Biological Macromolecules*, 24(1):49 – 59.
- Guibal, E., Milot, C., and Tobin, J. M. (1998). Metal-anion sorption by chitosan beads: equilibrium and kinetic studies. *Industrial & Engineering Chemistry Research*, 37(4):1454–1463.
- Gumustas, M., Sengel-Turk, C. T., Gumustas, A., Ozkan, S. A., and Uslu, B. (2017). Chapter 5 - effect of polymer-based nanoparticles on the assay of antimicrobial drug delivery systems. In Grumezescu, A. M., editor, *Multifunctional Systems for Combined Delivery, Biosensing and Diagnostics*, pages 67 – 108. Elsevier.
- Hong, C.-W. (1997). New concept for simulating particle packing in colloidal forming processes. *Journal of the American Ceramic Society*, 80(10):2517–2524.
- Hong, C.-W. (1998). From long-range interaction to solid-body contact between colloidal surfaces during forming. *Journal of the European Ceramic Society*, 18(14):2159 – 2167.
- Israelachvili, J. N. (1992). *Intermolecular and Surface Forces*. Academic Press.
- Israelachvili, J. N. and McGuiggan, P. M. (1988). Forces between surfaces in liquids. *Science*, 241(4867):795–800.
- Jang, L., Nguyen, D., and Geese, G. (1995). Effect of pH on the absorption of Cu(II) by alginate gel. *Water Research*, 29(1):315 – 321.
- Jha, I. N., Iyengar, L., and Rao, A. V. S. P. (1988). Removal of cadmium using chitosan. *Journal of Environmental Engineering*, 114(4):962–974.

- Johnson, C. A. and Lenhoff, A. M. (1996). Adsorption of charged latex particles on mica studied by atomic force microscopy. *Journal of Colloid and Interface Science*, 179(2):587 – 599.
- Juang, R.-S. and Shao, H.-J. (2002). A simplified equilibrium model for sorption of heavy metal ions from aqueous solutions on chitosan. *Water Research*, 36(12):2999 – 3008.
- Kim, A. Y. and Berg, J. C. (2000). Fractal heteroaggregation of oppositely charged colloids. *Journal of Colloid and Interface Science*, 229(2):607 – 614.
- Kim, A. Y., Hauch, K. D., Berg, J. C., Martin, J. E., and Anderson, R. A. (2003). Linear chains and chain-like fractals from electrostatic heteroaggregation. *Journal of Colloid and Interface Science*, 260(1):149 – 159.
- Kim, Y. H., Gihm, S. H., Park, C. R., Lee, K. Y., Kim, T. W., Kwon, I. C., Chung, H., and Jeong, S. Y. (2001). Structural characteristics of size-controlled self-aggregates of deoxycholic acid-modified chitosan and their application as a DNA delivery carrier. *Bioconjugate Chemistry*, 12(6):932–938.
- Kumar, J., Peglow, M., Warnecke, G., Heinrich, S., and Mrl, L. (2006). Improved accuracy and convergence of discretized population balance for aggregation: The cell average technique. *Chemical Engineering Science*, 61(10):3327 – 3342.
- Kyzas, G. Z. and Deliyanni, E. A. (2013). Mercury(II) removal with modified magnetic chitosan adsorbents. *Molecules*, 18(6):6193–6214.
- Langmuir, I. (1917). The constitution and fundamental properties of solids and liquids. II. liquids. 1. *Journal of the American Chemical Society*, 39(9):1848–1906.
- Lasko, C. L. and Hurst, M. P. (1999). An investigation into the use of chitosan

- for the removal of soluble silver from industrial wastewater. *Environmental Science & Technology*, 33(20):3622–3626.
- Lattuada, M., Sandkhler, P., Wu, H., Sefcik, J., and Morbidelli, M. (2003). Aggregation kinetics of polymer colloids in reaction limited regime: experiments and simulations. *Advances in Colloid and Interface Science*, 103(1):33 – 56.
- Lattuada, M., Wu, H., Sefcik, J., and Morbidelli, M. (2006). Detailed model of the aggregation event between two fractal clusters. *The Journal of Physical Chemistry B*, 110(13):6574–6586.
- Li, J.-F., Chen, C.-S., Yu, B.-Y., and Wei, W.-C. J. (2006). Simulation of colloidal particle packing for photonic bandgap crystals. *Journal of the American Ceramic Society*, 89(4):1257–1265.
- Lian, J., Xu, S., Yu, C., and Han, C. (2012). Removal of Mo(VI) from aqueous solutions using sulfuric acid-modified cinder: kinetic and thermodynamic studies. *Toxicological & Environmental Chemistry*, 94(3):500–511.
- Long, M. F., Shing, S. S., Tao, L. S., and Bi, W. T. (1999). Kinetic study of chitosan tripolyphosphate complex reaction and acid resistive properties of the chitosan tripolyphosphate gel beads prepared by in liquid curing method. *Journal of Polymer Science Part B Polymer Physics*, 37(14):1551–1564.
- López-López, J. M., Moncho-Jordá, A., Schmitt, A., and Hidalgo-Álvarez, R. (2005). Formation and structure of stable aggregates in binary diffusion-limited cluster-cluster aggregation processes. *Phys. Rev. E*, 72:031401.
- Lou, Z., Wang, J., Jin, X., Wan, L., Wang, Y., Chen, H., Shan, W., and Xiong, Y. (2015). Brown algae based new sorption material for fractional recovery of molybdenum and rhenium from wastewater. *Chemical Engineering Journal*, 273:231 – 239.

- Maindarkar, S. N., Bongers, P., and Henson, M. A. (2013). Predicting the effects of surfactant coverage on drop size distributions of homogenized emulsions. *Chemical Engineering Science*, 89:102 – 114.
- Maindarkar, S. N., Raikar, N. B., Bongers, P., and Henson, M. A. (2012). Incorporating emulsion drop coalescence into population balance equation models of high pressure homogenization. *Colloids and Surfaces A: Physicochemical and Engineering Aspects*, 396:63 – 73.
- Mao, Y. and McClements, D. J. (2011). Modulation of bulk physicochemical properties of emulsions by hetero-aggregation of oppositely charged protein-coated lipid droplets. *Food Hydrocolloids*, 25(5):1201 – 1209.
- Mladenovska, K., Cruaud, O., Richomme, P., Belamie, E., Raicki, R., Venier-Julienne, M.-C., Popovski, E., Benoit, J., and Goracinova, K. (2007). 5-ASA loaded chitosanCaalginate microparticles: Preparation and physicochemical characterization. *International Journal of Pharmaceutics*, 345(12):59 – 69.
- Monteiro, O. A. and Airoidi, C. (1999). Some thermodynamic data on copperchitin and copperchitosan biopolymer interactions. *Journal of Colloid and Interface Science*, 212(2):212 – 219.
- Moret, A. and Rubio, J. (2003). Sulphate and molybdate ions uptake by chitin-based shrimp shells. *Minerals Engineering*, 16(8):715 – 722.
- Murata, Y., Maeda, T., Miyamoto, E., and Kawashima, S. (1993a). Preparation of chitosan-reinforced alginate gel beads effects of chitosan on gel matrix erosion. *International Journal of Pharmaceutics*, 96(1):139 – 145.
- Murata, Y., Nakada, K., Miyamoto, E., Kawashima, S., and Seo, S.-H. (1993b). Influence of erosion of calcium-induced alginate gel matrix on the release of brilliant blue. *Journal of Controlled Release*, 23(1):21 – 26.

- Namasivayam, C. and Sangeetha, D. (2006). Removal of molybdate from water by adsorption onto ZnCl₂ activated coir pith carbon. *Bioresource Technology*, 97(10):1194 – 1200.
- Namasivayam, C. and Sureshkumar, M. V. (2009). Removal and recovery of molybdenum from aqueous solutions by adsorption onto surfactant-modified coir pith, a lignocellulosic polymer. *CLEAN Soil, Air, Water*, 37(1):60–66.
- Ng, J., Cheung, W., and McKay, G. (2003). Equilibrium studies for the sorption of lead from effluents using chitosan. *Chemosphere*, 52(6):1021 – 1030.
- Ngah, W. W., Endud, C., and Mayanar, R. (2002). Removal of copper(II) ions from aqueous solution onto chitosan and cross-linked chitosan beads. *Reactive and Functional Polymers*, 50(2):181 – 190.
- Ngah, W. W. and Fatinathan, S. (2008). Adsorption of Cu(II) ions in aqueous solution using chitosan beads, chitosanGLA beads and chitosanalginic acid beads. *Chemical Engineering Journal*, 143(13):62 – 72.
- Ngah, W. W. and Fatinathan, S. (2010). Adsorption characterization of Pb(II) and Cu(II) ions onto chitosan-tripolyphosphate beads: Kinetic, equilibrium and thermodynamic studies. *Journal of Environmental Management*, 91(4):958 – 969.
- Ostberg, T. and Graffner, C. (1994). Calcium alginate matrices for oral multiple unit administration: III. influence of calcium concentration, amount of drug added and alginate characteristics on drug release. *International Journal of Pharmaceutics*, 111(3):271 – 282.
- Peukert, W., Schwarzer, H.-C., and Stenger, F. (2005). Control of aggregation in production and handling of nanoparticles. *Chemical Engineering and Processing: Process Intensification*, 44(2):245 – 252.

- Puisto, A., Illa, X., Mohtaschemi, M., and Alava, M. (2012). Modeling the viscosity and aggregation of suspensions of highly anisotropic nanoparticles. *The European Physical Journal E*, 35(1).
- Prez-Candela, M., Martn-Martnez, J., and Torregrosa-Maci, R. (1995). Chromium(VI) removal with activated carbons. *Water Research*, 29(9):2174 – 2180.
- Raikar, N. B., Bhatia, S. R., Malone, M. F., McClements, D. J., Almeida-Rivera, C., Bongers, P., and Henson, M. A. (2010). Prediction of emulsion drop size distributions with population balance equation models of multiple drop breakage. *Colloids and Surfaces A: Physicochemical and Engineering Aspects*, 361(13):96 – 108.
- Raikar, N. B., Bhatia, S. R., Malone, M. F., McClements, D. J., and Henson, M. A. (2011). Predicting the effect of the homogenization pressure on emulsion drop-size distributions. *Industrial & Engineering Chemistry Research*, 50(10):6089–6100.
- Ramachandran, R. and Barton, P. I. (2010). Effective parameter estimation within a multi-dimensional population balance model framework. *Chemical Engineering Science*, 65(16):4884 – 4893.
- Rasa, M., Philipse, A., and Meeldijk, J. (2004). Heteroaggregation, reptization and stability in mixtures of oppositely charged colloids. *Journal of Colloid and Interface Science*, 278(1):115 – 125.
- Rodrigues, J. R. and Lagoa, R. (2006). Copper ions binding in cu-alginate gelation. *Journal of Carbohydrate Chemistry*, 25(2-3):219–232.
- Sader, J. E., Carnie, S. L., and Chan, D. Y. (1995). Accurate analytic formulas for the double-layer interaction between spheres. *Journal of Colloid and Interface Science*, 171(1):46 – 54.

- Sarei, F., Dounighi, N., Zolfagharian, H., Khaki, P., and Bidhendi, S. (2013). Alginate nanoparticles as a promising adjuvant and vaccine delivery system. *Indian Journal of Pharmaceutical Sciences*, 75(4):442–449.
- Sarmiento, B., Ribeiro, A., Veiga, F., Sampaio, P., Neufeld, R., and Ferreira, D. (2007). Alginate/chitosan nanoparticles are effective for oral insulin delivery. *Pharmaceutical Research*, 24(12):2198–2206.
- Sa, Y. and Aktay, Y. (2002). Kinetic studies on sorption of Cr(VI) and Cu(II) ions by chitin, chitosan and rhizopus arrhizus. *Biochemical Engineering Journal*, 12(2):143 – 153.
- Schaer, E., Ravetti, R., and Plasari, E. (2001). Study of silica particle aggregation in a batch agitated vessel. *Chemical Engineering and Processing*, 40(3):277–293.
- Schmitt, A., Odriozola, G., Moncho-Jorda, A., Callejas-Fernandez, J., Martinez-Garcia, R., and Hidalgo-Alvarez, R. (2000). Multiple contact kernel for diffusionlike aggregation. *Phys. Rev. E*, 62:8335–8343.
- Sefcik, J., Soos, M., Vaccaro, A., and Morbidelli, M. (2006). Effects of mixing on aggregation and gelation of nanoparticles. *Chemical Engineering and Processing: Process Intensification*, 45(10):936 – 943.
- Sezer, A. D. (1999). Release characteristics of chitosan treated alginate beads: I. sustained release of a macromolecular drug from chitosan treated alginate beads. *Journal of Microencapsulation*, 16(2):195–203.
- Sezer, A. D. and Akbuga, J. (1999). Release characteristics of chitosan treated alginate beads: II. sustained release of a low molecular drug from chitosan treated alginate beads. *Journal of Microencapsulation*, 16(6):687–696.
- Shawabkeh, R., Al-Harashseh, A., and Al-Otoom, A. (2004). Copper and zinc

- sorption by treated oil shale ash. *Separation and Purification Technology*, 40(3):251 – 257.
- Siew, C. K., Williams, P. A., and Young, N. W. G. (2005). New insights into the mechanism of gelation of alginate and pectin: Charge annihilation and reversal mechanism. *Biomacromolecules*, 6(2):963–969.
- Smidsrd, O., Skjk-Brk, G., and Draget, K. (2005). *Polysaccharides and Polyamides in the Food Industry: Properties, Production, and Patents*. WILEY-VCH Verlag GMBH & Co. KGaA.
- Soos, M., Sefcik, J., and Morbidelli, M. (2006). Investigation of aggregation, breakage and restructuring kinetics of colloidal dispersions in turbulent flows by population balance modeling and static light scattering. *Chemical Engineering Science*, 61(8):2349 – 2363.
- Tohver, V., Smay, J. E., Braem, A., Braun, P. V., and Lewis, J. A. (2001). Nanoparticle halos: A new colloid stabilization mechanism. *Proceedings of the National Academy of Sciences*, 98(16):8950–8954.
- Tourbin, M. and Frances, C. (2007). A survey of complementary methods for the characterization of dense colloidal silica. *Particle & Particle Systems Characterization*, 24(6):411–423.
- Turner, A. J., Nair, S., Lai, Z., Cheng, C.-M., and Bhatia, S. R. (2011). Controlled aggregation of colloidal particles for toner applications. *Journal of Applied Polymer Science*, 122(2):1358–1363.
- Udaybhasakar, P., Iyengar, L., and Rao, A. V. S. P. (1990). Hexavalent chromium interaction with chitosan. *Journal of Applied Polymer Science*, 39(3):739–747.
- Verwey, E. J. and Overbeek, J. T. G. (1948). *Theory of Stability of Lyophobic Colloids*. Elsevier.

- Wang, X., Du, Y., and Liu, H. (2004). Preparation, characterization and antimicrobial activity of chitosan-zein complex. *Carbohydrate Polymers*, 56(1):21 – 26.
- Williams, C., Aderhold, D., and Edyvean, R. (1998). Comparison between biosorbents for the removal of metal ions from aqueous solutions. *Water Research*, 32(1):216 – 224.
- Wu, C.-H., Lo, S.-L., and Lin, C.-F. (2000). Competitive adsorption of molybdate, chromate, sulfate, selenate, and selenite on γ -Al₂O₃. *Colloids and Surfaces A: Physicochemical and Engineering Aspects*, 166(13):251 – 259.
- Wu, C.-H., Lo, S.-L., Lin, C.-F., and Kuo, C.-Y. (2001). Modeling competitive adsorption of molybdate, sulfate, and selenate on γ -Al₂O₃ by the triple-layer model. *Journal of Colloid and Interface Science*, 233(2):259 – 264.
- Yang, Y., III, A. C., and Henson, M. A. (2012). Experimental investigation and population balance equation modeling of solid lipid nanoparticle aggregation dynamics. *Journal of Colloid and Interface Science*, 374(1):297 – 307.
- Yates, P. D., Franks, G. V., Biggs, S., and Jameson, G. J. (2005). Heteroaggregation with nanoparticles: effect of particle size ratio on optimum particle dose. *Colloids and Surfaces A: Physicochemical and Engineering Aspects*, 255(13):85 – 90.
- Yu, K., Ho, J., McCandlish, E., Buckley, B., Patel, R., Li, Z., and Shapley, N. C. (2013). Copper ion adsorption by chitosan nanoparticles and alginate microparticles for water purification applications. *Colloids and Surfaces A: Physicochemical and Engineering Aspects*, 425:31 – 41.
- Zhang, F., Long, G. G., Jemian, P. R., Ilavsky, J., Milam, V. T., and Lewis, J. A. (2008). Quantitative measurement of nanoparticle halo formation around colloidal microspheres in binary mixtures. *Langmuir*, 24(13):6504–6508.